Master Thesis

Comparison of Optimization Methods for Prechamber Spark Plug Operations in Natural Gas Engines using CFD-Simulation

Salvo Miccichè

Tutors

Mirko Baratta

Olaf Toedter

Master in Mechanical Engineering

Institut für Kolbenmaschinen (IFKM)

Politecnico di Torino - Karlsruher institut für Technologie

Torino, Italy - Karlsruhe, Germany

December 2019

Master Thesis

Master in Mechanical Engineering

Comparison of Optimization Methods for Prechamber Spark Plug Operations in Natural Gas Engines using CFD-Simulation

Salvo Miccichè

Tutors

Mirko Baratta

Olaf Toedter

Institut für Kolbenmaschinen (IFKM)

Politecnico di Torino - Karlsruher institut für Technologie

Torino, Italy - Karlsruhe, Germany

December 2019

Comparing Optimization Methods for Prechamber Spark Plug Operations in Natural Gas Engines using CFD-Simulation

Salvo Miccichè

Tutors: Mirko Baratta, Olaf Toedter

Abstract

One of the challenges engineering has to face nowadays is environmental sustainability: restrictions of emissions' standards and consumption reduction. For this purpose today, *prechamber* technology is bringing back in fashion natural gas fed internal combustion engines for stationary applications. By keeping the mixture very lean ($\lambda > 1.5$) one can reduce consumption and emissions of unburnt CH_4, CO and formaldehyde. It's not trivial, as combustion could be incomplete. Combustion is started in the narrow prechamber volume causing, thanks to the pressure gradient between pre- and main chamber, burnt gases jets to diffuse into the cylinder (*Turbulent Jet Ignition*). Prechamber geometry turns out to be of extreme importance. This work is an investigation on a natural gas engine equipped with prechamber. The first part of this master thesis deals with the validation of a suitable model for the numerical simulation of combustion in Star-CD. Several models for the ignition of the mixture have been compared, and several adjustments in the flame propagation model have been done. The setup used is *ECFM-3Z* model for combustion and *ISSIM* model for ignition. To reproduce in simulations the same early flame kernel development of the experimental case turned out to be crucial for building a suitable model. This phase is governed by laminar flame speed (LFS). The *Metghalchi* correlation, together with a correction at low pressure, was found to be appropriate to ensure consistent LFS values in this early phase. The second part is a comparison of several prechamber geometries, with the main goal of achieving a pressure peak the closest possible to TDC, and to have an uniform and complete combustion, optimizing the turbulent jets penetration into the cylinder. Apparent Heat

Release during combustion and fuel burnt profile were analyzed and compared with the standard geometry case. This analysis showed the importance of the number, the geometry and the orientation of the channels connecting prechamber with main one. The fastest combustion has been achieved with a 4 channels prechamber, which ensures the earliest diffusion of the turbulent jets into the main chamber. The use of channels tangential to the prechamber wall enhances the swirl motion of the flame, but the combustion is overall slower. The use of 4 narrow channels plus one at the bottom of the prechamber enhances the increase of turbulent kinetic energy of the fresh charge in the spark gap, with an overall slower combustion. One remarkable result of the simulation is that the first channel through which the flame propagates is the closest one to the breakdown spark.

Acknowledgements

My biggest thanks goes to my parents and my sister Carla, for their selfless emotional support and help during trouble time.
I thank my home university supervisor Prof. Mirko Baratta, for having supported me and having gave me many clever advice for my work, despite the distance.
I would like to thank my supervisor Dr.-Ing. Olaf Toedter for welcoming me and giving me the possibility to do this work, and Mr. Kamlesh Ghael for having supported and putted up with me during these months.
Finally, I thank all my friends for having been close through all this time.

Contents

1 Introduction **7**

1.1 Research engine specifics 7

2 Background **9**

2.1 Internal Combustion Engine 9

2.1.1 Overview 9

2.1.2 Engine operating cycle 10

2.1.3 Indicated and real quantities 11

2.2 Prechamber operations 13

2.3 Natural gas as fuel 14

2.3.1 Benefits 14

2.3.2 Drawbacks 15

2.4 Heat Release in the combustion engine 16

2.4.1 Apparent Heat Release 16

2.4.2 Integrated Heat Release and mass of fuel burnt 18

3 Methodology **19**

3.1 Fluid flow 19

3.1.1 Mass conservation 19

3.1.2 Momentum equation 19

3.1.3 Energy conservation: enthalpy 20

3.1.4 Mass transfer in fluid mixtures 21

3.2 Turbulence 22

3.3 Combustion 23

3.3.1 Overview 23

3.3.2 STAR-CD implementation: ECFM-3Z 25

3.3.3 STAR-CD implementation: ISSIM 31

4 Combustion model validation **34**

4.1 Mesh . . . 34

4.1.1 Coarse mesh . . . 35

4.1.2 Fine mesh . . . 35

4.2 Setup history . . . 36

4.2.1 Influence of secondary circuit inductance . . . 42

4.2.2 Influence of α . . . 44

4.2.3 Influence of boundary conditions . . . 47

4.2.4 Influence of laminar flame speed . . . 52

4.2.5 Influence of ignition energy . . . 63

4.2.6 Influence of ignition coordinates . . . 69

4.2.7 Influence of ignition timing . . . 71

5 Geometry optimization **73**

5.1 New prechamber geometries . . . 73

5.2 Choice of the model . . . 74

5.3 Results . . . 75

6 Conclusions **81**

6.1 Future work . . . 82

7 Appendix **83**

Chapter 1

Introduction

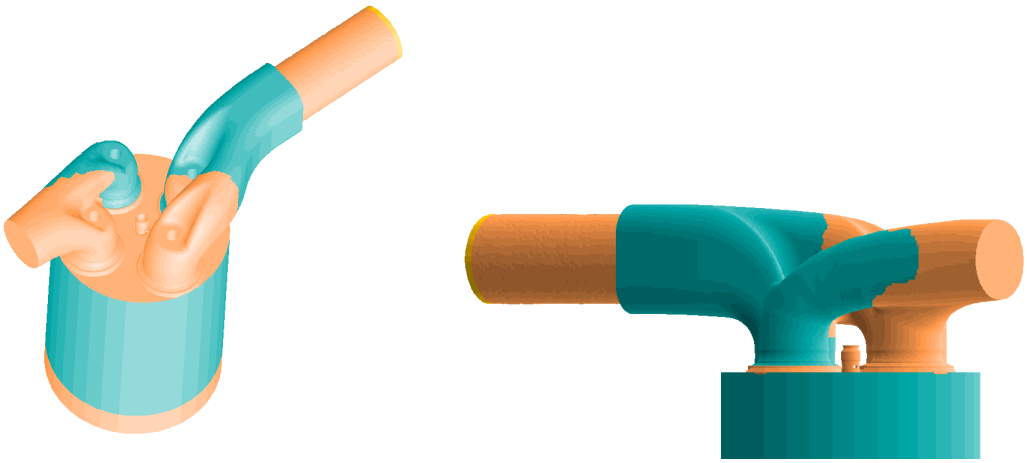

Figure 1.1: Fluid domain

1.1 Research engine specifics

The 4 stroke engine investigated is a large bore, heavy duty one. It is fed with natural gas (nearly completely methane), premixed in the first part of the intake pipe, so to have a completely homogeneous fresh charge. Equivalence ratio is $\phi = 0.6440$, ($\lambda = 1.5529$). The engine is equipped with 4 valves, 2 intake ones and 2 exhaust ones. The main peculiarity is the *prechamber*. At the site of the spark plug in the cylinder head, a small chamber with a perforated cap is separated from the main combustion chamber. With passive prechamber ignition, the compression stroke pushes the mixture through the openings into the prechamber where it is ignited by the spark plug. Prechamber can be built-in the engine or installed through devices

very similar to the classic spark plug, showing the same body shape but hollow. In this engine the prechamber is carved into the engine head. Electrodes are two concentric features: the cathode is the inner one, shaped as a cylinder, while the anode is ring shaped, linked to the prechamber wall by means of three uprights.

Engine type	large bore, single cylinder
Equivalence ratio ϕ	0.6440
Displacement [cc]	1991
Cylinder bore [m]	0.13
Piston stroke [m]	0.15
Connecting rod length [m]	0.273
Geometric compression ratio	12.4897
Engine cycle [degrees]	720
Rotational speed (constant) [rpm]	1500
Fuel	Methane (CH_4)
Fuel LHV [kJ/kg]	47100
Ignition timing	11.5° before fTDC

Table 1.1: Engine characteristics

Chapter 2

Background

2.1 Internal Combustion Engine

2.1.1 Overview

An internal combustion engine is a machine with the purpose of converting into mechanical energy the biggest part of a fuel's chemical energy through combustion. The working fluid, which by expanding and compressing exchanges energy with the engine moving parts, consists of air and fuel before combustion, and after combustion it includes the products of the oxidation of the fuel in air. The burnt gases are replaced with fresh charge at the end of every cycle through the inlet and exhaust gases. Based of the complete cycle duration, engines are classified into *2-strokes* engines and *4-strokes* ones. Among the several categories and classifications of internal combustion engines, it's worth emphasizing the difference between the *Otto* engines and the *Diesel* ones.

In *Otto* engines the mixture is ignited through a spark plug, which releases a certain amount of energy through an electric discharge, sufficient for the mixture to start burning (ideally at constant volume). In *Diesel* engines the fuel is injected within the hot and compressed air. In this way the autoignition of the mixture is provoked, to start a slower and more gradual combustion (ideally at constant pressure).

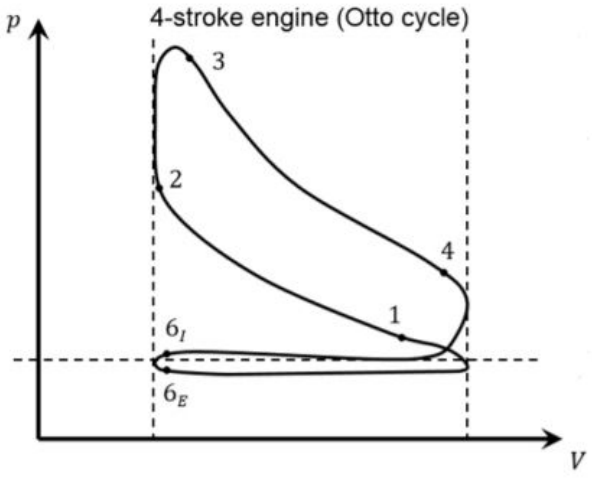

Figure 2.1: Pressure evolution inside the combustion chamber (*indicated cycle*). Picture taken from [15].

2.1.2 Engine operating cycle

Let us focus the attention on the case study engine, which is a *4-stroke, Otto cycle* engine. The pressure evolution inside the combustion chamber of an engine of this kind is represented in Figure 2.1 against the volume. The engine requires four strokes of the piston to complete a cycle with one power stroke. The piston moves between the top dead center position (TDC) and the bottom dead center position (BDC), which correspond to the minimum and maximum chamber volume, respectively. The volume swept out by the piston is the engine displacement V_0.

The 4 strokes of a SI engine are (referring to Figure 2.2):

- Intake stroke: piston moves from TDC to BDC and draws fresh mixture into the cylinder. To increase the mass induced, the inlet valve opens shortly before the stroke starts (6_I) and closes after it ends (1).

- Compression stroke: both the valves are closed and the mixture inside the cylinder is compressed to a small volume. Towards the end of the compression stroke, combustion is initiated (2) and the cylinder pressure rises dramatically.

- Expansion stroke: the high temperature and high pressure gases push down the piston toward its BDC position, and force the crank to rotate. When the

piston approaches BDC, the exhaust valve opens (4), the cylinder begins to be scavenged, and the pressure drops close to the exhaust one.

- Exhaust stroke: the burnt gases are kicked out by the piston as it moves towards TDC. As the piston approaches the TDC position, the inlet valve opens (6_I). The exhaust valve closes just after TDC (6_E).

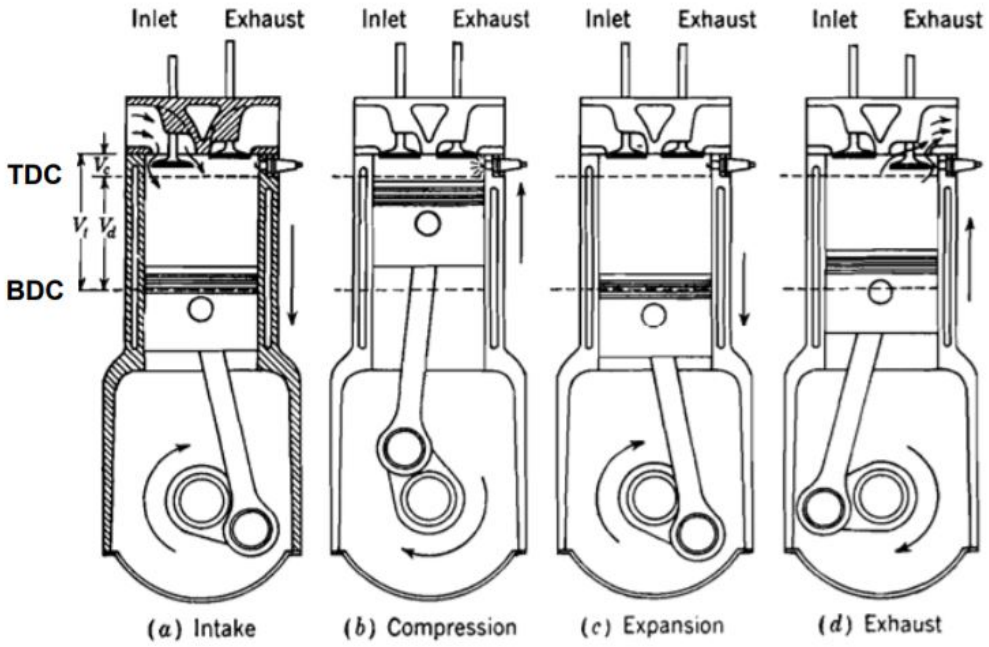

Figure 2.2: Piston and valves position during each stroke. The SI (spark ignition) engine reaches lower peak firing pressures with respect to CI (compression ignition) engines. Picture taken from [15].

2.1.3 Indicated and real quantities

To quantify the performances and the efficiencies of an internal combustion engine (*ICE*), some characteristic quantities are used. Let us imagine the ICE cycle on three levels of perfection: the ideal cycle, the indicated cycle and the real cycle. In the ideal cycle the strokes are represented as polytropic evolutions ($V = const.$ and adiabatic, Figure 2.3). It's trivial to derive the expression of the *thermodynamic efficiency* of the cycle as a function of the geometric compression ratio ϵ applying the polytropic evolution:

$$\eta_{th} = 1 - \epsilon^{1-k} \tag{2.1}$$

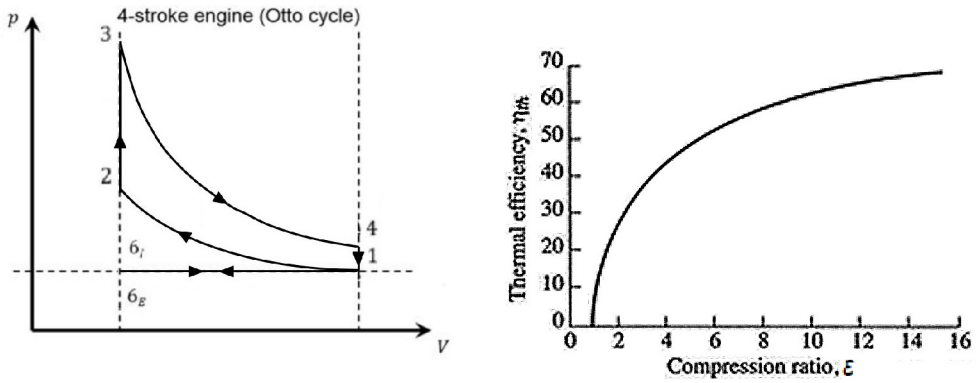

Figure 2.3: Ideal cycle and exponential behaviour of the thermal efficiency with respect to ϵ

Figure 2.3 shows the ideal cycle $p - V$ diagram and the exponential behaviour of the thermal efficiency. The indicated cycle pictures an evolution of the pressure in the combustion chamber (Figure 2.1) which is faithful to reality, differently from the ideal one. Besides, the indicated cycle does not consider dissipation inside the real engine. For this purpose, let us introduce the *brake mean effective pressure*:

$$bmep = imep - tfmep \tag{2.2}$$

Where:

- $bmep = brake\ mean\ effective\ pressure = \frac{\mathcal{L}_i}{V_0}$
- $imep = indicated\ mean\ effective\ pressure = \frac{\mathcal{L}_u}{V_0}$
- $tfmep = total\ friction\ mean\ effective\ pressure$

$\mathcal{L}_i$ and *imep* are respectively the indicated work per cycle [*Joule*] and the mean ordinate of the indicated cycle. $\mathcal{L}_i$ is thus the area inside the indicated cycle in the $p - V$ diagram. It takes into account: imperfect combustion, pumping work i.e. the portion of the area (negative) subtended by the counterclockwise curve, across the environmental pressure, leakages, heat exchanges. $\mathcal{L}_u$ is the real, measured work per cycle, taking into account: friction at the walls, auxiliaries, friction due to gas pressure. *bmep* is the corresponding value of pressure. *tfmep* represents all the losses just described ($\frac{\mathcal{L}_i - \mathcal{L}_u}{V}$).

These quantities are very useful for the final purpose of computing the *organic efficiency* 2.3 of the engine and the overall efficiency of the engine called *global efficiency* 2.4.

$$\eta_o = \frac{bmep}{imep} = 1 - \frac{tfmep}{imep} \tag{2.3}$$

$$\eta_g = \frac{P_u}{\dot{m}_f LHV} \tag{2.4}$$

$P_u = \mathcal{L}_u \frac{n}{2} i$ is the correspondent of $\mathcal{L}_u$ in terms of power, and i is the number of cylinders. η_g value varies widely depending on the application/type of engine:

- Otto engines for commercial vehicles: $0.28 \div 0.36$
- Aspirated Diesel engines for heavy vehicles: $0.36 \div 0.44$
- Heavy duty turbocharged Diesel engines: $0.40 \div 0.53$

2.2 Prechamber operations

A number of ignition options are available for lean burn Otto cycle gas engines. The most widespread are: open chamber spark ignition, passive prechamber spark ignition, active prechamber spark ignition, open chamber diesel micro-pilot injection and prechamber diesel micro-pilot injection [8]. The natural gas engine provided with a prechamber is a relatively new technology which, according to many (see IAV lecture at 27th Aachen Colloquium Automobile and Engine Technology [7]) can lead in the early future to 45% global efficiency. The purpose of a prechamber is to enhance combustion in extremely lean mixture conditions. Because of that, combustion in initiated inside the small volume of the prechamber (usually $\approx 2\%$ of the main combustion chamber volume [9]) to achieve a so called TJI *Turbulent Jet Ignition* [16]. Right after ignition the pressure inside the prechamber raises dramatically to much above the main chamber one, this difference generates a throttling effect thanks to the narrow channels. The burning gases are suddenly blown out the prechamber causing the flame to propagate inside the cylinder in the form of turbulent jets.

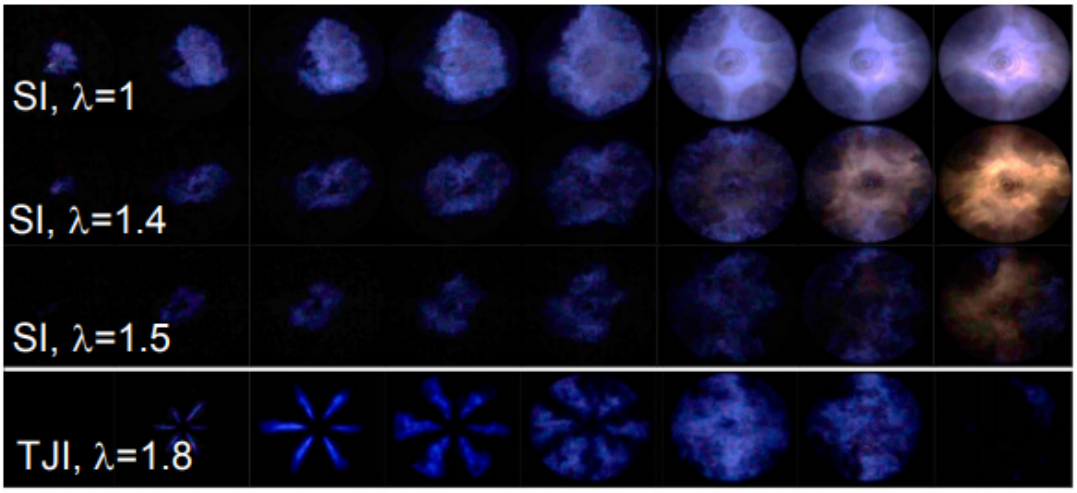

Figure 2.4: Turbulent Jet Ignition picture obtained from an engine with optical access. The combustion of very lean mixtures ($\lambda = 1.8$) can be stabilized equipping the engine with a prechamber. Image taken from [16]

2.3 Natural gas as fuel

2.3.1 Benefits

Natural gas is composed mainly by methane (CH_4 up to 97%) and longer-chain hydrocarbons such as ethane (C_2H_6), propane (C_3H_8), butane (C_4H_{10}) and in minimal quantities pentane (C_5H_{12}). The state of physical of this fuel is gaseous, and the transportation is realized through gas pipelines even for very long distances. Considering the other fuels on the market, like gasoline or diesel, natural gas is the one producing less polluting emissions during its whole lifecycle: production, storage and transport phases. Moreover, being methane the quasi totality of the fuel, the particulate matter after combustion is nearly zero. To exploit its gaseous state of physical, which means high mixing potential with air (nearly 100% homogeneous mixtures), natural gas in combustion engines applications is premixed and only in a few applications injected. The mixture is sucked into the cylinder environment allowing duel fuel operations and active prechamber operations (for charge stratification). One other benefit of natural gas is its high octane number, whose typical values range from 100 to 130, compared to the 95-98 of gasoline. Mixture is less reactive at high pressure-temperature conditions, thus higher compression ratios can be achieved, directly affecting the engine efficiency (see Chapter 2.2). The direct

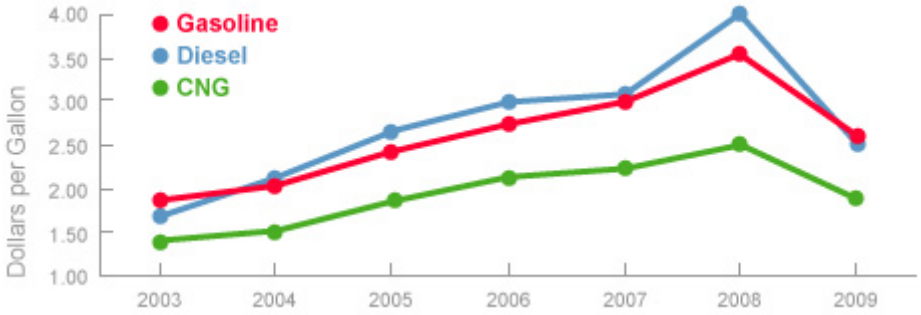

Figure 2.5: Image taken from [22]

consequence is that sturdy engines should be built if one wants to increase much the compression ratio. Heavy-duty (like domestic power supply or grid balancing) engines turn out to be one of the most suitable field of application for natural gas, as long as they do not need to be carried by a vehicle and they do not need to be very powerful but very efficient. Furthermore, because of the clean-burning attributes of natural gas, NGEs generally have longer life compared to most gasoline-powered engines. Last but not least, the cost of natural gas is historically lower than any other of the above mentioned fuels, thanks also to the large amount of resources (Figure 2.5).

2.3.2 Drawbacks

There are two major disadvantages in natural gas operations: the relatively low Efficiency in Transportation (the mileage is lower than gasoline), and the environmental damage deriving from emitting unburnt CH_4 in the atmosphere. Methane is estimated to have a Global Warming Potential (GWP) of 26 times with respect to carbon dioxide (standard potential 1) over 100 years. CH4 emitted today lasts about a decade on average, which is much less time than CO2 but it absorbs much more energy than CO2. The net effect of the shorter lifetime and higher energy absorption is reflected in the GWP. The CH4 GWP also accounts for some indirect effects, such as the fact that CH4 is a precursor to ozone, and ozone is itself a greenhouse gas [1].

2.4 Heat Release in the combustion engine

To describe the progress of combustion in an internal combustion engine it can be convenient to refer to some quantities derived with theoretical elaborations from experimental results, especially pressure. In the case of numerical simulations, the approach remains the same, but the data to be elaborated come from simulations' results.

2.4.1 Apparent Heat Release

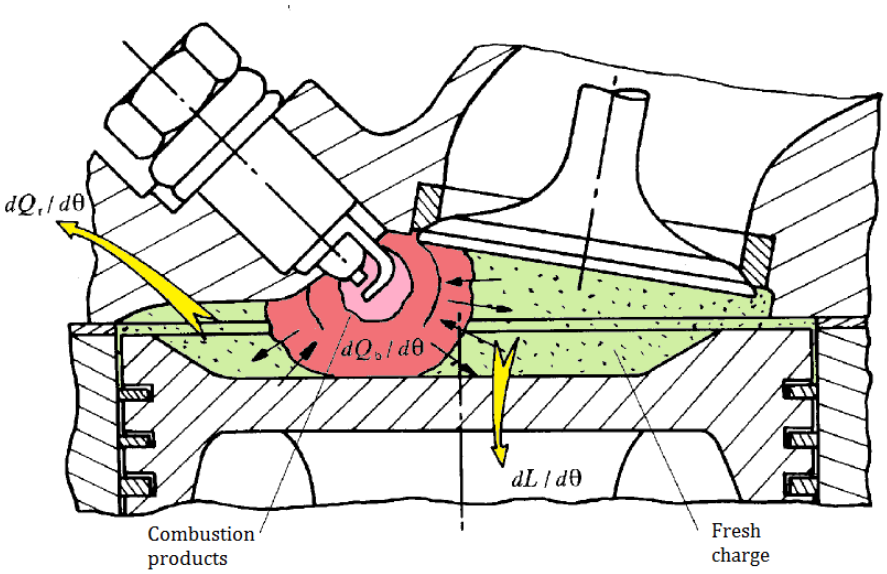

Figure 2.6: The gases inside the cylinder, with a good approximation, can be considered as a closed and homogeneous system. Image taken from [4].

In the figure above, the gases inside the combustion chamber can be considered as a system, eventually with mass exchange with the environment, but as this analysis concerns combustion phase, it can be said to be a closed system. Let us apply the First Law of Thermodynamics: the gases are exchanging work with the moving parts of the engine $\frac{dL}{d\theta}$ (only piston in this crank angle interval), heat through the refrigerated cylinder walls $\frac{dQ_r}{d\theta}$, and eventually mass $\frac{dm_i}{d\theta}$, but as long as in this time interval there's no valve open, we can consider leakages negligible and say there is no mass exchange. Moreover the energy of the gaseous system is changing $\frac{dE}{d\theta}$. The production term is the heat generated by the chemical reaction of the gases .

$$\frac{dQ_b}{d\theta} + \Sigma_i h_i \frac{dm_i}{d\theta} = \frac{dE}{d\theta} + \frac{dL}{d\theta} + \frac{dQ_r}{d\theta} \tag{2.5}$$

All the terms are known but the last one $\frac{dQ_r}{d\theta}$. Considering the fluid as a perfect gas of average temperature T, we can explicit energy as:

$$\frac{dE}{d\theta} = mc_v \frac{dT}{d\theta} + c_v T \frac{dm}{d\theta} \tag{2.6}$$

while temperature T can be expressed as a function of p and V through the ideal gas law. Differentiating, one has:

$$\frac{dT}{d\theta} = \frac{p}{mR}\frac{dV}{d\theta} + \frac{V}{mR}\frac{dp}{d\theta} + \tag{2.7}$$

The work per degree crank angle is:

$$\frac{dL}{d\theta} = p\frac{dV}{d\theta} \tag{2.8}$$

Summing these terms according to Equation 2.5, one has:

$$\frac{dQ_b}{d\theta} = \frac{k}{k-1} p \frac{dV}{d\theta} + \frac{1}{k-1} V \frac{dp}{d\theta} + \frac{dQ_r}{d\theta} \tag{2.9}$$

Now the last step is to model the heat losses through the walls with an appropriate law, for example:

$$\frac{dQ_r}{d\theta} = Sh_i(T - T_p) \tag{2.10}$$

Subtracting this last term, Equation 2.9 represents the Apparent Heat Release, and it is a function of the only pressure.

2.4.2 Integrated Heat Release and mass of fuel burnt

By integrating the equation for Apparent Heat Release in the combustion domain (crank angle), one obtains the total amount of heat released Q_b, which equals with a low percentage error (normally around 5%) the product of the total mass of fuel burnt per cycle times its lower heating value:

$$Q_b = \int_{\theta_i}^{\theta_f} \frac{dQ_b}{d\theta} d\theta \approx m_c H_i \tag{2.11}$$

Therefore, both the Integrated Heat Release curve and the fuel burnt per cycle one, are S-shaped, whit decreasing slope (corresponding to AHR) while gradually getting closer to combustion end. The peak IHR value achieved at the end represents respectively the total heat released [J] and the total mass -or mass fraction- of fuel burnt [g]. It is worth also looking to the percentage error between the two quantities, to have an estimation of the degree of completeness of the oxidation reactions, and of the accuracy of the simulation result with respect to experimental measurements. It's possible to individuate the start, the end and the center of combustion referring to the fraction of fuel burnt: 10% for start [4], 50% for center and 90% for end.

Chapter 3

Methodology

3.1 Fluid flow

STAR-CD is a Computational Fluid Dynamics software which utilizes mathematical models for describing fluid flow, turbulence and chemical reactions. The basic is constituted by Navier Stokes set of partial differential equations.

3.1.1 Mass conservation

Using the Einstein tensor notation, this is the expression of the conservation of mass in the general limit of compressible flow:

$$\frac{\partial \rho}{\partial t} + \frac{\partial (\rho u_j)}{\partial x_j} = s_m \tag{3.1}$$

Where:

- ρ density
- x_j coordinate of the j-th direction
- u_j j-th component of velocity vector
- s_m mass source or sink

3.1.2 Momentum equation

$$\frac{\partial \rho u_i}{\partial t} + \frac{\partial}{\partial x_j}(\rho u_j u_i - \tau_{ij}) = -\frac{\partial p}{\partial x_j} + s_i \tag{3.2}$$

Where:

- s_i momentum source

- p piezometric pressure $p = p_s - p_0$

- τ_{ij} stress tensor

Stress tensor accounts for the contribution due to viscosity and turbulence. Its general form is:

$$\tau_{ij} = \mu\left(\frac{\partial u_i}{\partial x_j} + \frac{\partial u_j}{\partial x_i}\right) - \frac{2}{3}\mu\frac{\partial u_k}{\partial x_k}\delta_{ij} - \overline{\rho}\overline{u_i' u_j'} \tag{3.3}$$

Where the first and the second term are related to shear viscous stress, while the third one comes along with turbulence when introducing Reynolds averaging of variables. u_i' in fact, represents the fluctuating component of velocity. How to model this term is a deep problem and it will be discussed further on.

3.1.3 Energy conservation: enthalpy

The total energy is expressed as the sum of a mechanical energy term and a static chemico-thermal enthalpy term:

$$H = \frac{1}{2}u_i u_j + h = \frac{1}{2}u_i u_j + h_t + \Sigma Y_m H_m \tag{3.4}$$

Where:

- h_t thermal enthalpy

- Y_m species m concentration

- H_m formation enthalpy of species m

- Thermal enthaply is defined as:

$$h_t = \overline{c}_p T - c_p^0 T_0 \tag{3.5}$$

The general form of the total enthalpy H conservation equation can be derived from the chemico-thermal enthalpy transport equation:

$$\frac{\partial \rho h}{\partial t} + \frac{\partial}{\partial x_j}(\rho u_j h + F_{h,j}) = \frac{\partial p}{\partial t} + u_j \frac{\partial p}{\partial x_j} + \tau_{i,j} \frac{\partial u_i}{\partial x_j} + s_h \tag{3.6}$$

or the equivalent:

$$\frac{\partial \rho h_t}{\partial t} + \frac{\partial}{\partial x_j}(\rho u_j h_t + F_{h,j}) = \frac{\partial p}{\partial t} + u_j \frac{\partial p}{\partial x_j} + \tau_{i,j} \frac{\partial u_i}{\partial x_j} + s_h - \Sigma_m H_m s_{c,m} \tag{3.7}$$

Where:

- $\overline{c}_p$ mean constant-pressure specific heat at temperature T
- c_p^0 reference specific heat at temperature T_0
- $F_{h,j}$ diffusional energy flux in direction x_j
- $F_{h_t,j}$ diffusional thermal energy flux in direction x_j
- s_h energy source
- $s_{c,m}$ rate of production or consumption of species m due to chemical reaction

Thus, combining an equation for mechanical energy conservation derived from 3.2 and the static chemico-thermal enthalpy equation 3.6 we obtain the total enthalpy conservation equation:

$$\frac{\partial \rho H}{\partial t} + \frac{\partial}{\partial x_j}(\rho u_j H + F_{h,j} - u_i \tau_{i,j}) = \frac{\partial p}{\partial t} + s_i u_i + s_h \tag{3.8}$$

3.1.4 Mass transfer in fluid mixtures

Each mixture component m has a local concentration in each point of the domain, which is called Y_m and its transport equation is:

$$\frac{\partial \rho Y_m}{\partial t} + \frac{\partial}{\partial x_j}(\rho u_j Y_m - F_{m,j}) = s_m \tag{3.9}$$

Where:

- $F_{m,j}$ diffusional flux component
- s_m mass source or sink

$F_{m,j}$ is computed through the *Fick's law*, which can be time averaged in the turbulent case. This procedure leads to the generation of the *mass fraction fluctuation* term, which again is modeled through the turbulence model adopted. *Fick's law:*

$$F_{m,j} = \rho Y_i V_{m,j} \tag{3.10}$$

Where $V_{m,j}$ is the j-th component of the diffusion velocity $\mathbf{V}_m$.

3.2 Turbulence

Turbulence problem can be resumed in the lack of equations which rises from the new born turbulent Reynolds stresses. To achieve sufficiently precise results and keep the computational cost relatively low, *RANS* approach has been chosen, which is based on the concept of *time average*:

$$< u >= \lim_{T\to\infty} \frac{1}{T} \int_0^T u(t)dt \tag{3.11}$$

Applying this definition to any random variable $u(x,t)$ leads to the decomposition into a mean component and a fluctuating one (*Reynolds decomposition*):

$$u_i = u_i + u_i' \tag{3.12}$$

Let us define now the *ensamble average*:

$$< u >= \lim_{N\to\infty} \frac{1}{N} \sum_{i=1}^{N} u^{(i)} \tag{3.13}$$

We can see ensamble average as the real way to extrapolate a mean value from a stochastic variable through measurements. The two averages are equivalent only in the limit of *ergodicity* of the stochastic variable averaged. For ergodicity to hold, by definition the time interval has to be big, thus not allowing to catch turbulence perturbations. RANS allows to compute only mean flow quantities.

Applying Reynolds averaging to conservation equations, new Reynolds stress terms born. They represent unknowns in the previous conservation equations for momentum, enthalpy and mass fraction. Many theories have been formulated to solve them and the problem is still not completely solved. Some suitable models can be used for CFD applications like the so called $k-\epsilon$ models. Reynolds stress tensors are expressed as a function of the mean flow variables to eliminate an unknown, through the proportionality with the *turbulent viscosity* μ_t (*Boussinesq hypothesis*):

$$\mu_t = f_\mu \frac{C_\mu \rho k^2}{\epsilon} \tag{3.14}$$

The problem is turned into solving two transport equation for k and ϵ (*RANS formulation*). Several versions of $k-\epsilon$ models are available in STAR-CD, in this work the so called *RNG (Renormalization Group)* was used. It is employed in high Reynolds number form, therefore not applicable to near wall regions, thus leading to the need for near wall treatment models. k and ϵ equations are solved everywhere but close to the wall, and they are:

$$\frac{\partial(\rho k)}{\partial t} + \frac{\partial}{\partial x_j}\left[\rho u_j k - \left(\mu + \frac{\mu_t}{\sigma_k}\right)\frac{\partial k}{\partial x_j}\right] = \mu_t(P + P_B) - \rho\epsilon - \frac{2}{3}\left(\mu_t \frac{\partial u_i}{\partial x_i} + \rho k\right)\frac{\partial u_i}{\partial x_i} \tag{3.15}$$

$$\begin{aligned}\frac{\partial(\rho\epsilon)}{\partial t} + \frac{\partial}{\partial x_j}\left[\rho u_j \epsilon - \left(\mu + \frac{\mu_t}{\sigma_k}\right)\frac{\partial k}{\partial x_j}\right] = \\ = C_{\epsilon,1}\frac{\epsilon}{k}\left[\mu_t P - \frac{2}{3}\left(\mu_t \frac{\partial u_i}{\partial x_i} + \rho k\right)\frac{\partial u_i}{\partial x_i}\right] + C_{\epsilon,3}\frac{\epsilon}{k}\mu_t P_B - C_{\epsilon,2}\rho\frac{\epsilon^2}{k} + \\ + C_{\epsilon,4}\rho\epsilon\frac{\partial u_i}{\partial x_i} - \frac{C_\mu \eta^3 (1 - \frac{\eta}{\eta_0})}{1 + \beta\eta^3}\frac{\rho\epsilon^2}{k}\end{aligned} \tag{3.16}$$

Near wall treatment models available are *Angelberger* and *GruMo-UniMORE*.

3.3 Combustion

3.3.1 Overview

Combustion inside a combustion chamber is a very complex process. It is influenced by many variables, so the prediction of the real course of the events is extremely dif-

ficult, and its numerical simulation is strongly dependent on assumptions. Though, one can say that combustion (in an engine environment) is mostly influenced by:

- flow field
- species in the mixture
- quantity and distribution of the species
- pressure and temperature

The laminar flame front propagates with S_L *laminar flame speed*. In a combustion engine the flame propagation phenomenon is driven mostly by turbulence and by the flow field inside the chamber. Laminar velocities would not be sufficient to achieve a relatively small crank angle interval for complete combustion, even in near stoichiometric conditions (maximum S_L). Furthermore, to speed up the combustion duration with the increasing rotational speed, the propagation speed should increase with the rotational speed itself, which is not the case of S_L. This is needed to achieve the pressure peak nearly in proximity of the same crank angle (usually TDC).
The flame front is no longer regular and smooth when turbulence occurs: turbulent eddies wrinkle the flame front, making it corrugated. It looks like a lamina curved several times on itself, as a fractal geometry [14] (Figure 3.1).

Flame front propagation is additionally accelerated thanks to the confined environment: burnt gases expand, pushing the fresh charge towards the periphery of the chamber, compressing and heating them.
Let us give some simple definitions:

i) r_f flame radius

ii) u_b mean burnt gas expansion speed

iii) S_b burning velocity

iv) u_f flame front expansion speed

$u_f \cong u_b$ is the real *Observed speed*. Let us take a look to its trend as a function of the kernel radius r_f in Figure 3.2: provided that S_b increases with r_f, one can still notice how the latter (flame speed u_f) is different from S_b. This discrepancy is due

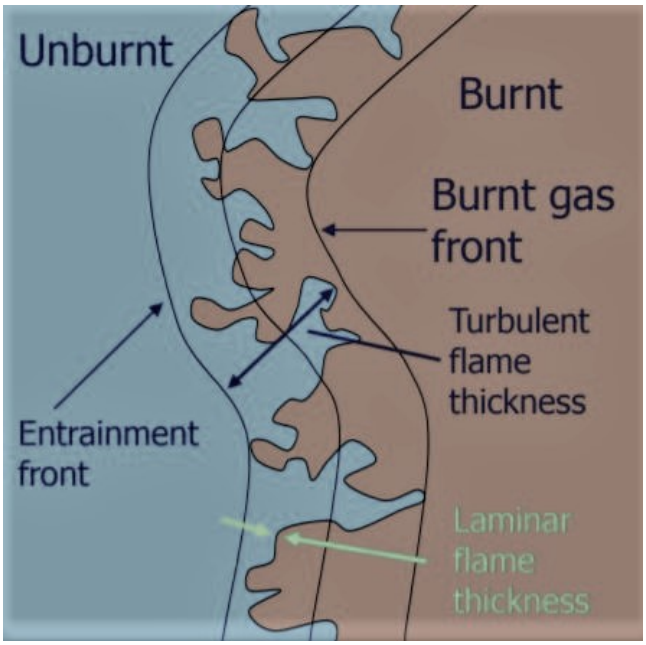

Figure 3.1: Turbulent flame front. Picture taken from [14]

to the unburnt gas speed u_g just ahead of the flame front. u_g is a transport term. In the graph of Figure 3.2 it's possible to see how the very first combustion phase (small kernel) is governed by laminar flame speed: S_b assumes its laminar value S_L (work developed by G. Beretta, M. Rashidi, and J. Keck [3]) .

3.3.2 STAR-CD implementation: ECFM-3Z

STAR-CD has powerful means to model combustion. For the gas engine of this work, the flow chart to which the software sticks is the representation of the combustion's phases:

1. Ignition and *flame kernel* development
2. Flame propagation

This is completed with a model to describe the chemical reaction. One of the most suitable combustion models available in STAR-CD for spark ignition engines is the *ECFM-3Z (Extended Coherent Flame model)* (as described by [19]). The model itself is made up by four models for:

- Mixing
- Flame propagation

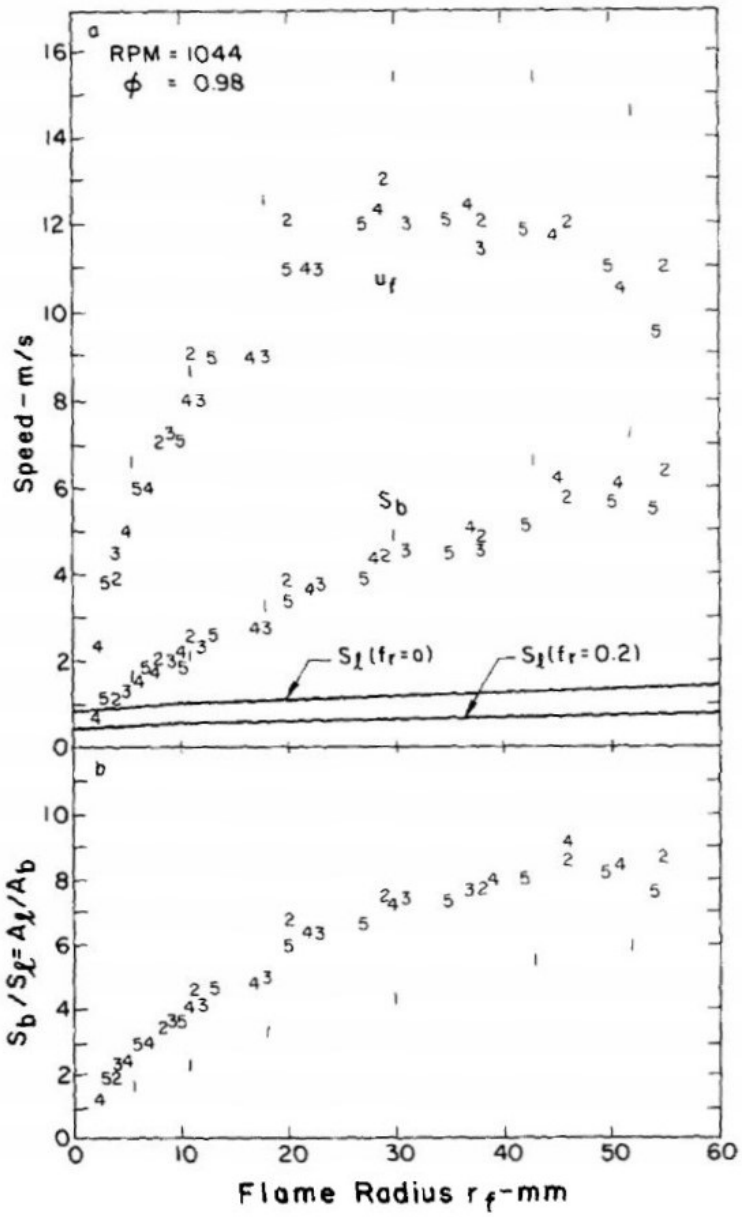

Figure 3.2: (a) u_f and the corresponding burning velocity S_b as a function of flame radius for 5 measured cycles. Also shown is the laminar burning speed S_L for 0 and 20% residual burned gas fractions. (b) Corresponding ratio $S_b/S_L = A_L/A_b$. Picture taken from [3]

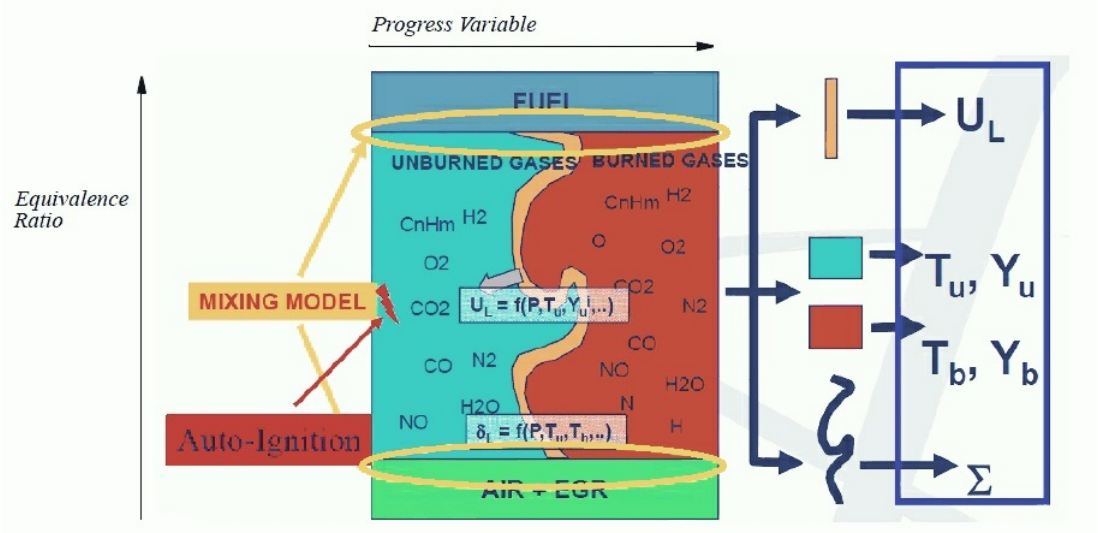

Figure 3.3: ECFM-3Z model schematic. Picture taken from [19]

- Post-flame and emission

- Spark ignition and knock

Mixing

3Z stands for 3 zones of mixing, namely the unmixed fuel zone, the unmixed air plus EGR zone, and the mixed gases zone. The zones are small with respect to the mesh size, so they are treated as sub-grid quantities. In both the fuel and oxidizer sides, the mass fraction of unmixed fuel Y_{fum} and unmixed oxygen Y_{o2um} are solved by means of transport equations. Very important in this phase is the mixing timescale τ_m, often assumed to be equal to the turbulent timescale $\tau_m = \tau_T = k/\epsilon$. The mixing zone is the result of turbulent and molecular mixing, and it is the area in which combustion takes place. Thus all the process will be influenced by the concentration of the species there. The mass fraction of species in the mixing zone can be defined as the fractions' conditional averages:

$$Y_i^m = Y_i\big|_{Z=Z_m} = \int_{\delta V} Y(x',t)\delta[Z(x',t) - Z_m]dV' \tag{3.17}$$

Where Z_m is the mean mixture fraction and δ the Dirac function. Each Y_i^m (for unmixed fuel and unmixed oxygen) is governed by a transport equation:

$$\frac{\partial \rho Y_{fum}}{\partial t} + \nabla \cdot (\rho \mathbf{u} Y_{fum}) - \nabla \left[\left(D + \frac{\mu_t}{Sc_t} \right) \nabla Y_{fum} \right] = \frac{-\beta_{min}}{\tau_m} Y_{fum} \left(1 - Y_{fum} \frac{\rho}{\rho_u} \frac{W_m}{W_f} \right) + \dot{\omega}_{evap} \quad (3.18)$$

$$\frac{\partial \rho Y_{o2um}}{\partial t} + \nabla \cdot (\rho \mathbf{u} Y_{o2um}) - \nabla \left[\left(D + \frac{\mu_t}{Sc_t} \right) \nabla Y_{o2um} \right] = \frac{-\beta_{min}}{\tau_m} Y_{o2um} \left(1 - \frac{Y_{o2um}}{Y_{o2inf}} \frac{\rho}{\rho_u} \frac{W_m}{W_f} \right) + \dot{\omega}_{evap} \quad (3.19)$$

Flame propagation

The flame propagation phase is described through Flame Surface Density (FSD) [19], defined as:

$$\Sigma = \overline{\Sigma'} = \lim_{\delta V \to 0} \frac{\overline{\delta A}}{\delta V} \quad (3.20)$$

Where the overbar represents the ensamble averaging. STAR-CD uses one of the most common forms of its transport equation:

$$\frac{\partial \Sigma}{\partial t} + \nabla \cdot (\mathbf{u}\Sigma) - \nabla \cdot \left[\left(D + \frac{\mu_t}{Sc_t} \right) \nabla \left(\frac{\Sigma}{\rho} \right) \right] = \Sigma \left[C_{divu} \frac{2}{3} \nabla \cdot u + C \alpha \Gamma \frac{\epsilon}{k} + C \frac{2}{3} \frac{\rho_u}{\rho_b} U_L \Sigma \frac{1-c}{c} - \beta U_L \Sigma \frac{1}{1-\overline{c}} - \frac{2}{3} \frac{1}{(\gamma p)} \frac{\partial p}{\partial t} \right] + S_{conv} \quad (3.21)$$

Where:

- D molecular diffusivity
- C_{divu} empirical parameter with default value of 1
- C corretion factor for taking into account the chemical timescale and the flame quenching at the walls

- Γ the ITNFS (Net Flame Stretch) function

- ρ_u and ρ_b unburnt and burnt gas density

- U_L effective laminar speed

- Q_L laminar flame speed correction factor for heat-loss effect

- α and β empirical coefficients

- μ_t turbulent viscosity

- p thermodynamic pressure

- $\overline{c}$ Reynolds averaged progress variable

Laminar flame speed value is crucial in the computation of flame surface density. Its value depends on the equivalent ratio, the species, the temperature and the pressure in the environment. To compute it, STAR-CD allows to choose between tables for the fuel in use (Natural gas library for this case), and correlations.

Metghalchi and Keck correlation The simplest alternative and the most widely used form of the wholly empirical correlation is the so-called power law formula [2], adopted by many investigators. One of the most known studies in which such a form was employed is the work by Metghalchi and Keck [13]. This correlation is not recommended off the limit of near-stoichiometric mixtures. Threshold for consistent values of laminar flame speed is fixed to $\phi > 0,65$. The study was carried out in a range of pressure 0,4 - 50 atm

$$S_L = S_{L0}\left(\frac{T_u}{T_0}\right)^{\alpha}\left(\frac{p}{p_0}\right)^{\beta} \tag{3.22}$$

Where α, β and S_{L0} depend on the equivalent ratio.

Gülder correlation A completely different approach for determining the term $S_{L0}(\phi)$ in equation 3.22, was proposed by Gülder [6]. In his work no dependence on equivalence ratio was proposed for α and β, but constant values. Gülder correlation

is the following:

$$S_L = WZ\phi^{\eta} \cdot exp[-\zeta(\phi - 1.075)^2]\left(\frac{T_u}{T_0}\right)^{\alpha}\left(\frac{p}{p_0}\right)^{\beta} \tag{3.23}$$

Where W, Z, ζ, α and β are fuel-dependent constants, which for methane are shown in table 3.1:

$\boldsymbol{W}$	$\boldsymbol{Z}$	α	β
1	0.422	2.00	-0.5

Table 3.1: Gülder coefficients in case of single fuel (methane).

Correction factor C This factor mostly accounts for the flame quenching at the walls. It is basically governed by an on-off mechanism which can be regulated by the user:

$$C = q_w / \left[1 + \left(\alpha\Gamma\frac{\epsilon}{k} + \frac{2}{3}\frac{\rho_u}{\rho_b}S_L\Sigma\frac{1-c}{c}\right)\tau_c\right] \tag{3.24}$$

and q_w:

$$q_w = \begin{cases} 1 & if \quad y^+/y_c^+ > D_{querat} \\ 0 & if \quad y^+/y_c^+ > D_{querat} \end{cases} \tag{3.25}$$

Where y^+ and y_c^+ represent the adimensional longitudinal coordinate (distance from the wall) used in the boundary layer theory, and D_{querat} the discriminant value below which the correction is active. It can be tuned by the user.

Ignition and knock

Ignition is the preliminary phase which includes the initiation of the flame, realized by releasing a certain amount of energy into the mixture with a spark plug.
Spark plug circuit stores some electric energy. When breakdown occurs, an electric arc plays as a bridge between electrodes thus initiating the circuit discharge process,

releasing the electric energy. This sudden energy absorption allows a primary flame kernel to develop, the very initial phase of combustion and flame propagation.
The choice of the ignition model is of utmost importance. The more parameters one can set, the more the model is difficult to tune but, at the same time, the more one gets closer to reality. One of the most suitable ignition models is *ISSIM*. For the sake of completeness and simplicity the next section is dedicated to illustrate the method.

3.3.3 STAR-CD implementation: ISSIM

The *ISSIM (Imposed Stretch Spark Ignition)* is a 10 years old ignition model. Hallmark of ISSIM is to model the reaction rate of the growing flame kernel no longer in a zero-dimensional way, but through the FSD. To use it from the very first phases requires some corrections for the transport equation. The user can set the amount energy in the secondary circuit E_s, of which only the fraction E_{ign} will be released to the fluid. When $E_{ign}(t) > E_{crit}(t)$, the software recognizes the correct conditions for ignition. An initial burnt gas is created, and it is evaluated through a target burnt gas volume fraction $\overline{c}_{ign}$:

$$\overline{c}_{ign} = c_0 \exp\left[-\left(\frac{|x - x_{spk}|}{0.7 d_{le}}\right)^2\right] \tag{3.26}$$

To assign a value to $c(x,t)$ in the spatial and temporal domain, the reaction rate of this progress variable is written as:

$$\overline{\dot{\omega}_c} = max\left(\rho_u S_L \Sigma, \frac{\rho_b(\overline{c}_{ign} - \overline{c})}{dt}\right) \tag{3.27}$$

The FSD equation needs to be initialized as soon as the initial burnt gas kernel of radius r_b^{ign} is created. FSD is computed alongside through the transport equation, till the instant in which the second term becomes the maximum:

$$\overline{\Sigma} = max\left(\overline{\Sigma}, \frac{3}{r_b^{ign}}\overline{c}_{ign}\right) \tag{3.28}$$

At this point FSD equation is initialized according to ISSIM description of the flame kernel development [23]. Please note how, integrating along the x coordinate (kernel radius) the second term in Equation 3.28, one obtains $4\pi(r_b^{ign})^2$ which is the external surface of the current spherical flame kernel, consistently with the initialization criterion discussed so far.

Modifications of FSD equation

Spark source term S_{conv} ISSIM overestimates the effect of the spark on the FSD equation. When the ignition criterion is satisfied for the first time, the earliest target profile $\overline{c}_{ign}$ is created. Convection has the effect to replace burnt gases in the vicinity of spark plug with fresh charge. If the energy criterion is still satisfied STAR-CD goes on in producing further $\overline{c}_{ign}$ profiles. This is not realistic since the RANS approach tell us that the initial distribution $\overline{c}_{ign}(x,t)$, quickly convected away, is such that $\overline{c}(x,t) < \overline{c}_{ign}(x,t)$, the latter being computed as in equation 3.26.
The solution implemented in STAR-CD is to determine a new equation for the correct profile adjusting c_0 (see equation 3.26). This is done by determining the exact amount of mass convected around the spark dm_b^{ign} with a phenomenological approach, and then c_0 is computed satisfying the condition:

$$dm_b^{ign} = \int \rho_b max((c_{ign} - c), 0) dV \tag{3.29}$$

The spark source term in FSD equation 3.21 is defined as:

$$S_{conv} = max\left(\frac{3}{r_b^{ign}}\overline{c}_{ign} - \Sigma, 0.0\right) \tag{3.30}$$

Modification of the laminar flame speed near the spark plug The energy released by the spark plug causes an increase in temperature and thus in laminar flame speed. When a laminar flame speed table is in use, ISSIM foresees the use of a correction to S_L in the vicinity of the spark. At kernel developing phase, the LFS used is the one computed by ISSIM, regardless of the value given by the table in use.

$$S_L^{eff} = S_L^0 \cdot 0.5\left[1 - \frac{4\delta_L^0}{l_{spk}} + \sqrt{\Delta}\right] \tag{3.31}$$

$$\Delta = \left[\frac{4\delta_L^0}{l_{spk}} - 1\right] + 4\left[\frac{4\delta_L^0}{l_{spk}}\right]\left[1 + \frac{E_{ign}}{400 c_p^b m_b}\right] = \left[\frac{4\delta_L^0}{l_{spk}} - 1\right] + 4\left[\frac{4\delta_L^0}{l_{spk}}\right]\left[1 + \frac{\Delta T_b^{ign}}{400}\right] \tag{3.32}$$

Where:

- S_L^0 standard laminar flame speed
- δ_L^0 standard laminar flame thickness
- c_p^b specific heat capacity of the burnt gases
- m_b total burnt gas mass

To adjust the influence interval of the correction:

$$S_L^{eff} = S_L^0 \cdot \left[1 + (S_L^{corr} - 1) \cdot exp - \left(2\frac{|x - x_{spk}|}{l_{spk} \cdot SPINFEXT2}\right)\right] \tag{3.33}$$

$$\Delta T_b^{ign} = min\left(\frac{E_b}{c_p^b m_b}, TEMPMAXSLCORR\right) \tag{3.34}$$

The user can tune the parameters *SPINFEXT2* and *TEMPMAXSLCORR*.

When a correlation is used more complex corrections are available to obtain plausible LFS values, and this case will be discussed later in Chapter 4.2.4.

Chapter 4

Combustion model validation

The first step of the work was to build a suitable model for the CFD analysis of combustion. All the models available in STAR-CD have been illustrated in Chapter 3. The current stage consisted of finding the most suitable models for the case study, and tuning them according to the real engine's features, to get the most faithful simulations results possible. The quantities which is common use to analyze for evaluate the combustion in a engine environment are:

- Pressure evolution
- Temperature evolution
- Apparent Heat Release Rate
- Integrated Heat Release Rate

as a function of the crank angle (see Chapter 2.4). These data were compared to the ones coming from measurements on the engine model *FP5105-1810*.

4.1 Mesh

The current work is based on the previous studies realized by [11]. In the latter, the charge motion inside the cylinder has been investigated, as well as a grid independence evaluation. Three mesh grids with different refinement levels have been tested in the same conditions, to check the analysis dependence on the grid. The results are a check point for the current work. To decrease the computational effort and

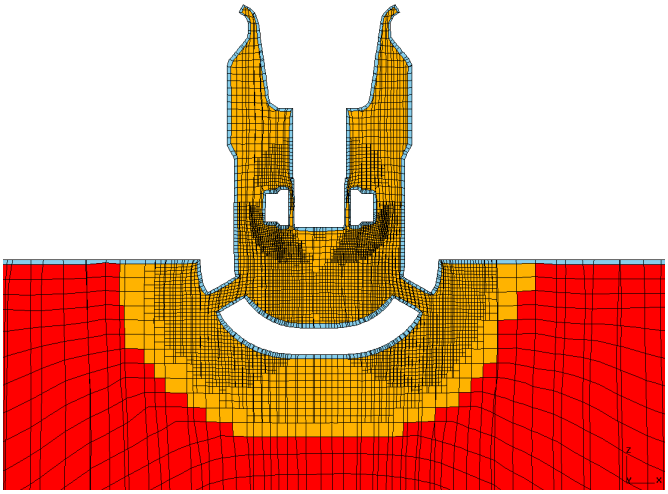

Figure 4.1: Highlight of the prechamber coarse mesh (x-direction section): one can see the refined zones in correspondence of the spark gap, the channels and the area of the main chamber close to them.

the time, a less refined mesh has been used for the model validation purpose. At the end of this process, before to switch to the finer mesh, a quick grid independence check has been performed.

4.1.1 Coarse mesh

This mesh was realized with the *Trimming method* [20], built in STAR-CD. The area between electrodes as well as the whole prechamber volume and a portion of the main chamber close to the channels (Figure 4.1), has a refined mesh size to catch properly combustion events. The use of a mesh originated automatically by the Trimming function is recommended by Siemens to receive dedicated support by the company itself.

4.1.2 Fine mesh

The fine mesh consists of a cylinder grid and a prechamber one, which are assembled together in es-ice. Since independence has been verified by [11], the choice fell on the mesh with intermediate cell size. All the four prechamber meshes which have been compared consist of nearly the same amount of cells (Table 4.1).

Fine mesh cells	
cylinder	3 mln
standard prechamber	670 k
K2 prechamber	900 k
K3 prechamber	978 k
K4 prechamber	841 k

Table 4.1: Fine mesh cells

4.2 Setup history

A preliminary open cycle simulation (simulation which includes the valve openings intervals) has been run starting from scratch (340 c.a.). The intermediate solution at 630.9 c.a. was extrapolated (*SMAP* technique in STAR-CD). This backup was used as an initial condition for mapping the flow field of the next closed cycle simulations (intake valve closes at 545 c.a.). This is done to shorten the simulations duration (range and time) and reduce the computational cost. In the validation phase, the simulations were run in the range 630.9 - 760 crank angle, with a variable time step size, refined in the ignition and combustion period.

Time step size (°)	
630.9°	0.1
705°	0.05
708°	0.01
730°	0.05
740°	0.1

Table 4.2: Time step size

The modelling of the combustion phase in an engine is not an easy process since many variables have a big influence on the phenomenon. This work has been based on some initial choices as concerns combustion and ignition models, and validation consisted of shaping them to best fit the experimental case. Among the numerous amount of physical variables playing a role in combustion, it turned out that *laminar flame*

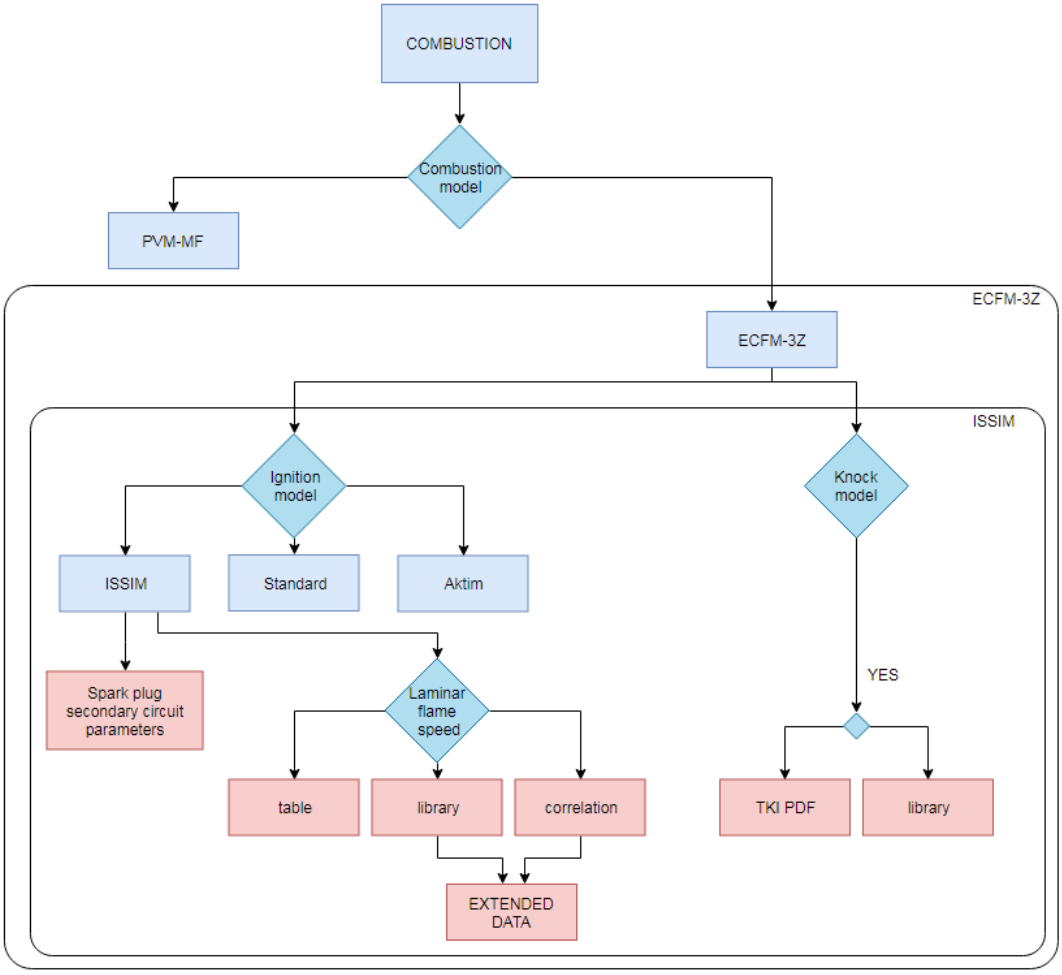

Figure 4.2: Scheme of the path for creating the model.

speed is the most crucial in this case study. The flow chart (Figure 4.2) highlights the critical points of the procedure, showing in diamond boxes the points where an hypothesis on the correct path to follow has to be made.

ECFM-3Z is the most suitable model for the case study and one of the best for spark ignition engines (Chapter 3.3.2). ISSIM is the ignition method chosen (Chapter 3.3.3). ISSIM is an advanced internal combustion engine model which allows the user to set many parameters concerning the spark plug secondary circuit, the ignition points, the laminar flame speed. The tuning of all of them is a long process (drawback), but it allows to reproduce the real setup in a quite precise way. The red boxes shown in Figure 4.2 represent all the sensible parameters to tune the combustion in simulations, i.e. the ones set by the user. The wall function used is *GruMo-UniMORE*.

The first approach is a simple setup where the least number of parameters was

changed from STAR-CD standard, to see how close the result could be to real case. Below is an overview of the simulations performed. This is a compact version of full table listing all the complete setup (Appendix, Table 7.3).

	Ignition (ISSIM)				ECFM-3Z				B.C.	Extended data		
	Ignition		Spark circuit						Walls			
	Ignition angle [deg]	Ignition point [cm]	Energy [J]	Inductance [H]	Laminar flame speed	Auto ignition model	α [-]	β [-]	Electrodes temperature [K]	ULAM3	ULAM3BELOW	PRTRANSL
	708.5°	(-1.4925; 0; 2.4)	0.1	20	STAR-CD open	no	1.6	1	950			
1	700°	4 ignition points	0.1	20	STAR-CD open	no	1.6	1	950			
2	708.5°	4 ignition points	0.1	20	STAR-CD open	no	1.6	1	950			
3	708.5°	(-1.4925; 0; 2.4)	0.1	40	STAR-CD open	no	1.6	1	950			
4	708.5°	(-1.4925; 0; 2.4)	0.1	10	STAR-CD open	no	1.6	1	950			
5	708.5°	(-1.4925; 0; 2.4)	0.1	20	STAR-CD open	no	2	1	950			
6	708.5°	(-1.4925; 0; 2.4)	0.1	20	STAR-CD open	TKI PDF	1.6	1	950			
7	708.5°	(-1.4925; 0; 2.4)	0.1	20	STAR-CD open	no	1.6	1	Adiabatic			
8	708.5°	(-1.4925; 0; 2.75)	0.1	20	Gülder	no	1.6	1	950			
9	708.5°	(-1.4925; 0; 2.75)	0.1	20	Metghalchi	no	1.6	1	950			
10	708.5°	(-1.4925; 0; 2.75)	0.1	20	STAR-CD open	no	1.6	1	950	standard setup		
11	708.5°	(-1.4925; 0; 2.75)	0.1	20	Gülder	no	2	1	Adiabatic			
12	700°	(-1.4925; 0; 2.75)	0.1	20	STAR-CD open	no	1.8	1	Adiabatic	standard setup		
13	708.5°	(-1.4925; 0; 2.75)	0.1	20	library	library	1.6	1	950			
14	690°	(-1.4925; 0; 2.75)	0.1	20	STAR-CD open	no	1.6	1	950			
15	708.5°	(-1.4925; 0; 2.75)	0.1	20	Metghalchi	no	1.6	1	950	45	50	383959
16	708.5°	(-1.4925; 0; 2.75)	0.1	20	Metghalchi	no	1.6	1	950	45	100	383959
17	700°	(-1.4925; 0; 2.75)	1	20	STAR-CD open	no	1.6	1	950	standard setup		
18	708.5°	(-1.4925; 0; 2.75)	0.1	20	Metghalchi	no	1.6	1	950	45	70	550000

Figure 4.3: Overview of the simulations performed

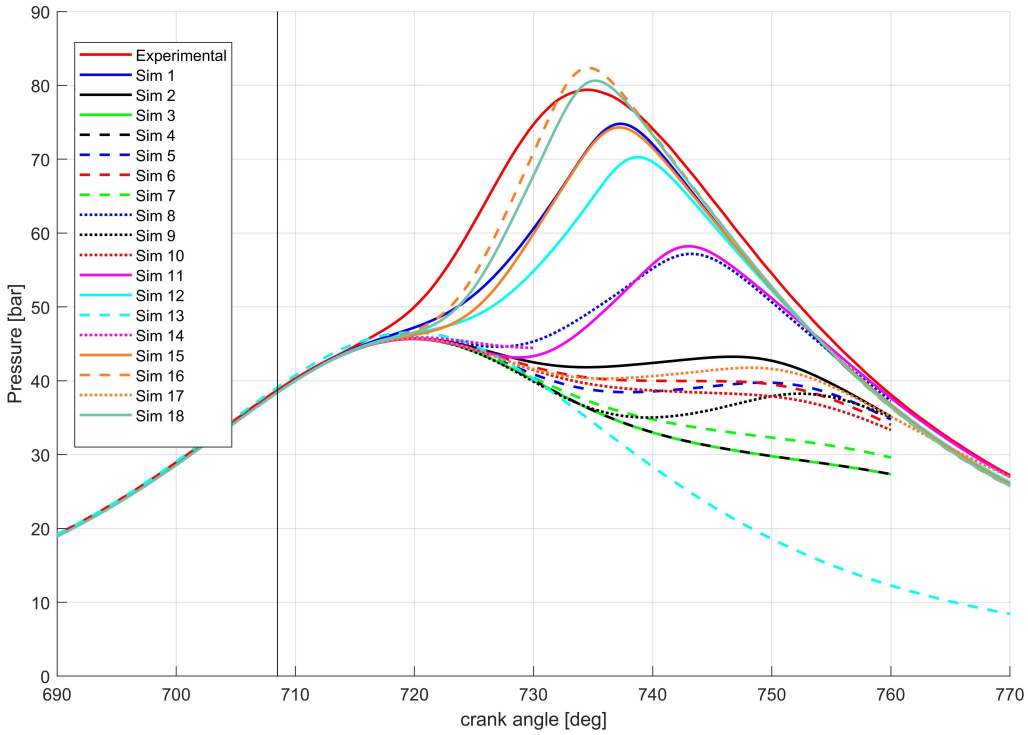

Figure 4.4: Pressure

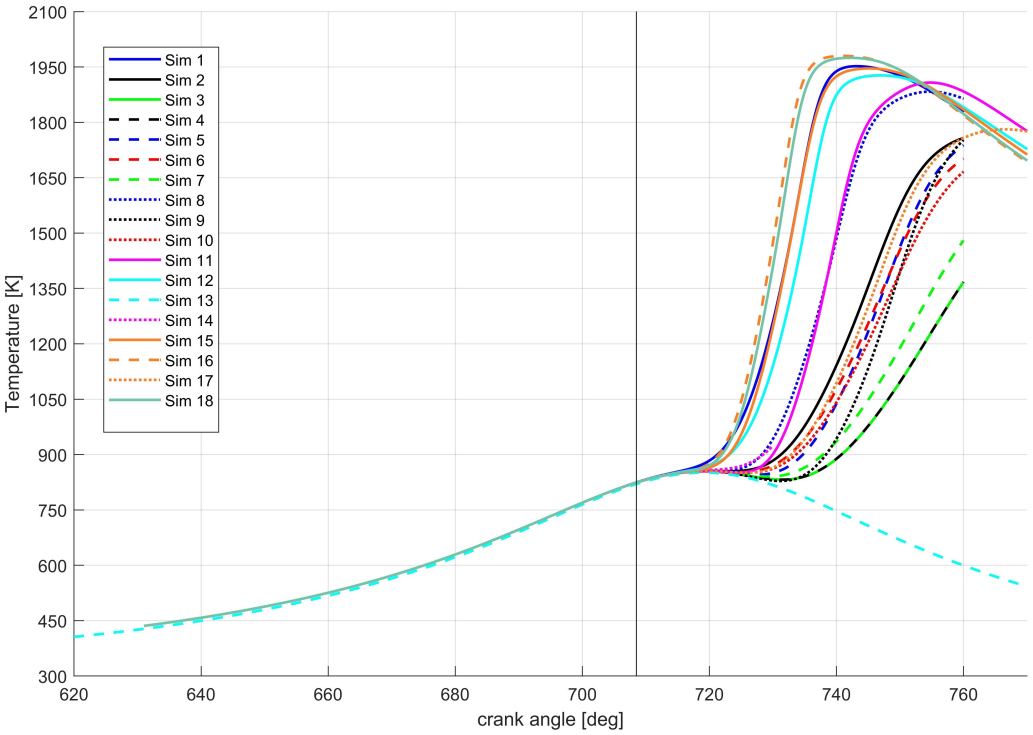

Figure 4.5: Temperature

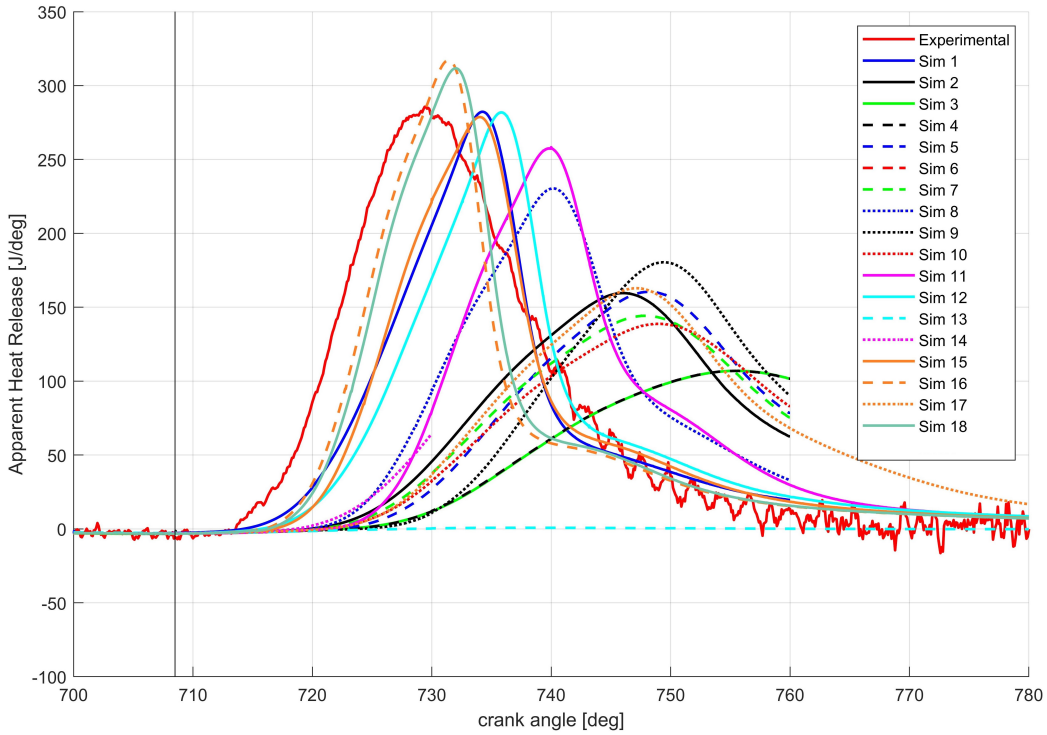

Figure 4.6: Apparent Heat Release

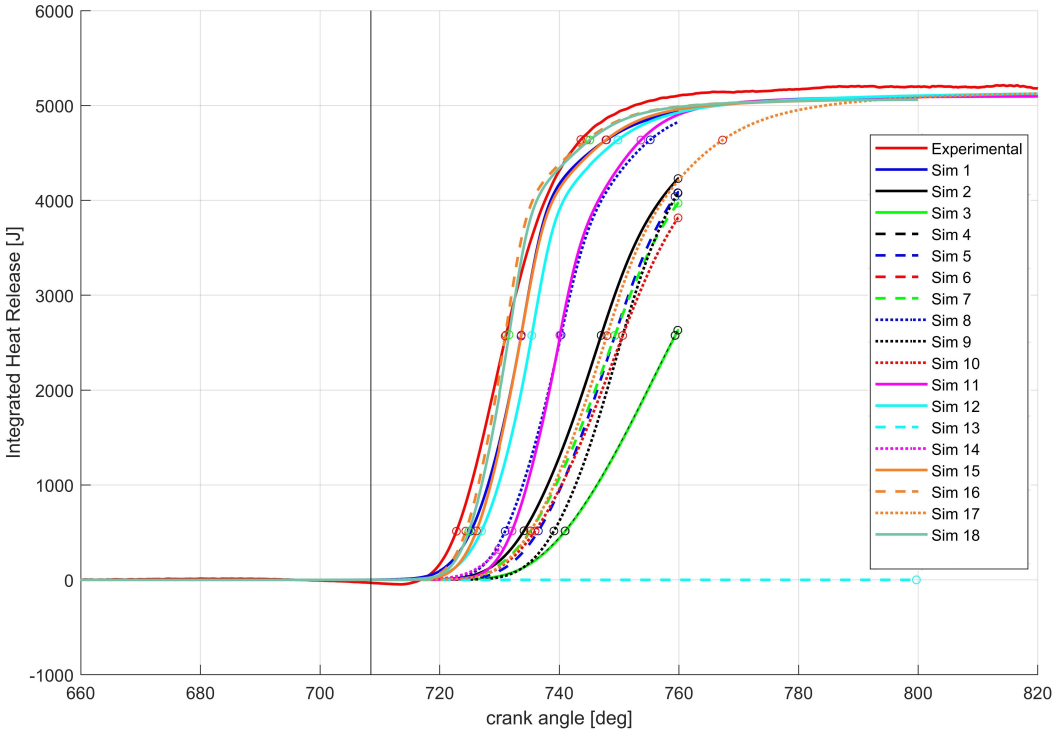

Figure 4.7: Integrated Heat Release

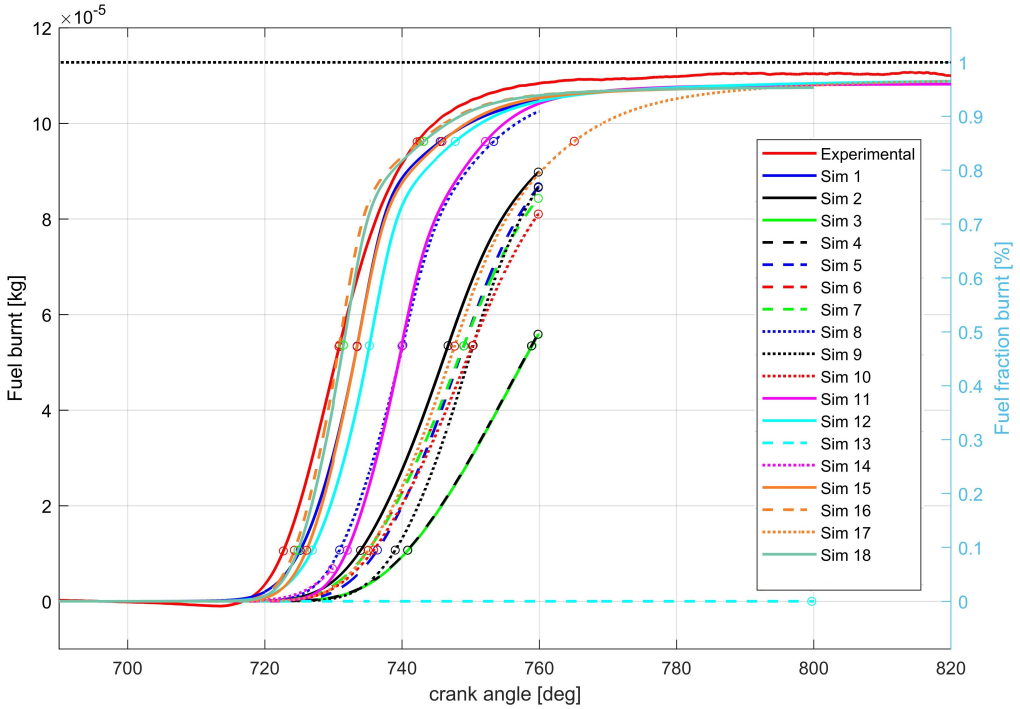

Figure 4.8: Fuel burnt

NAME	START	END	DURATION	CENTRE
Exp	722.4	741.9	19.50	730.6
Sim 1	725.15	745.55	20.40	733.45
Sim 2	733.95	759.85	25.90	746.70
Sim 3	740.85	759.85	19.00	758.95
Sim 4	740.80	759.80	19.00	758.85
Sim 5	736.40	759.85	23.45	749.00
Sim 6	735.05	759.85	24.80	748.95
Sim 7	735.05	759.85	24.80	748.95
Sim 8	730.90	753.35	22.45	740.10
Sim 9	739.00	759.85	20.85	750.35
Sim 10	735.85	759.85	24.00	750.25
Sim 11	732.01	752.15	20.14	739.98
Sim 12	726.91	747.75	20.84	735.24
Sim 13	799.70	799.70	0.00	799.70
Sim 14	729.85	729.85	0.00	729.85
Sim 15	726.07	745.80	19.73	733.45
Sim 16	724.31	742.60	18.29	730.80
Sim 17	735.05	765.10	30.05	747.65
Sim 18	724.83	743.15	18.32	731.45

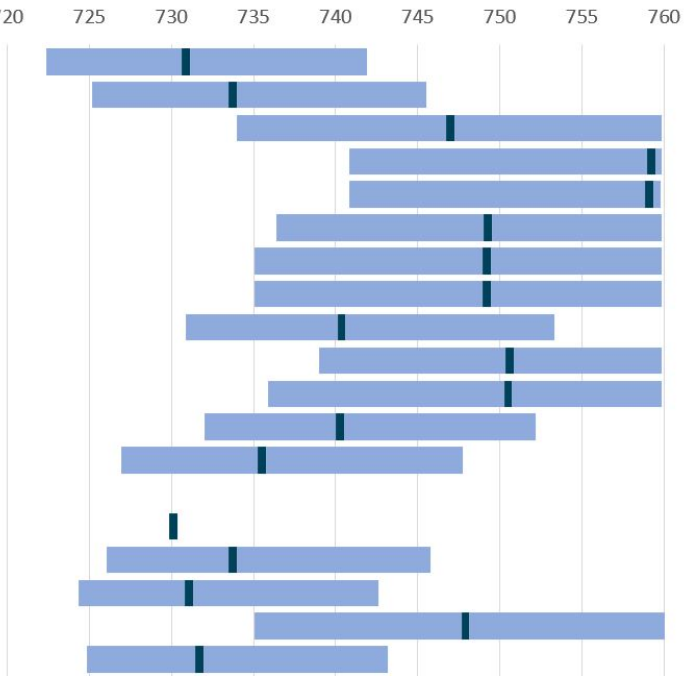

Figure 4.9: Combustion duration

4.2.1 Influence of secondary circuit inductance

The energy released by the spark obeys a time dependent law (Equation 4.7 will be shown later on in Chapter 4.2.5) which refers to the R-L secondary circuit, thus it depends on the current flowing in the secondary circuit of the spark plug. The current in the secondary circuit can be estimated from

$$i_s(t) = \sqrt{\frac{2E_s(t)}{L_s}} \tag{4.1}$$

where L_s is the circuit inductance set by the user into the *Star controls* section of *es-ice*. Two simulations have been performed to verify whether L_s has a considerable influence on the energy release rate, and thus in the early flame development. In Simulation 3 and Simulation 4 the inductance sizes of 40 H and 10 H have been tried respectively, which are the double and the half of the nominal value of 20 H of the standard setup. As one can see clearly in the results plots, no difference arose between Simulation 3 and 4. All the curves are perfectly superimposable. Being the combustion phenomenon exactly equal in both the simulations, the conclusion is that L_s is not influential in this case study's simulation. These results thus, being equal to the case where $L_s = 20H$, will be considered as equivalent to the standard ones, for the purpose of future comparisons to other simulations.

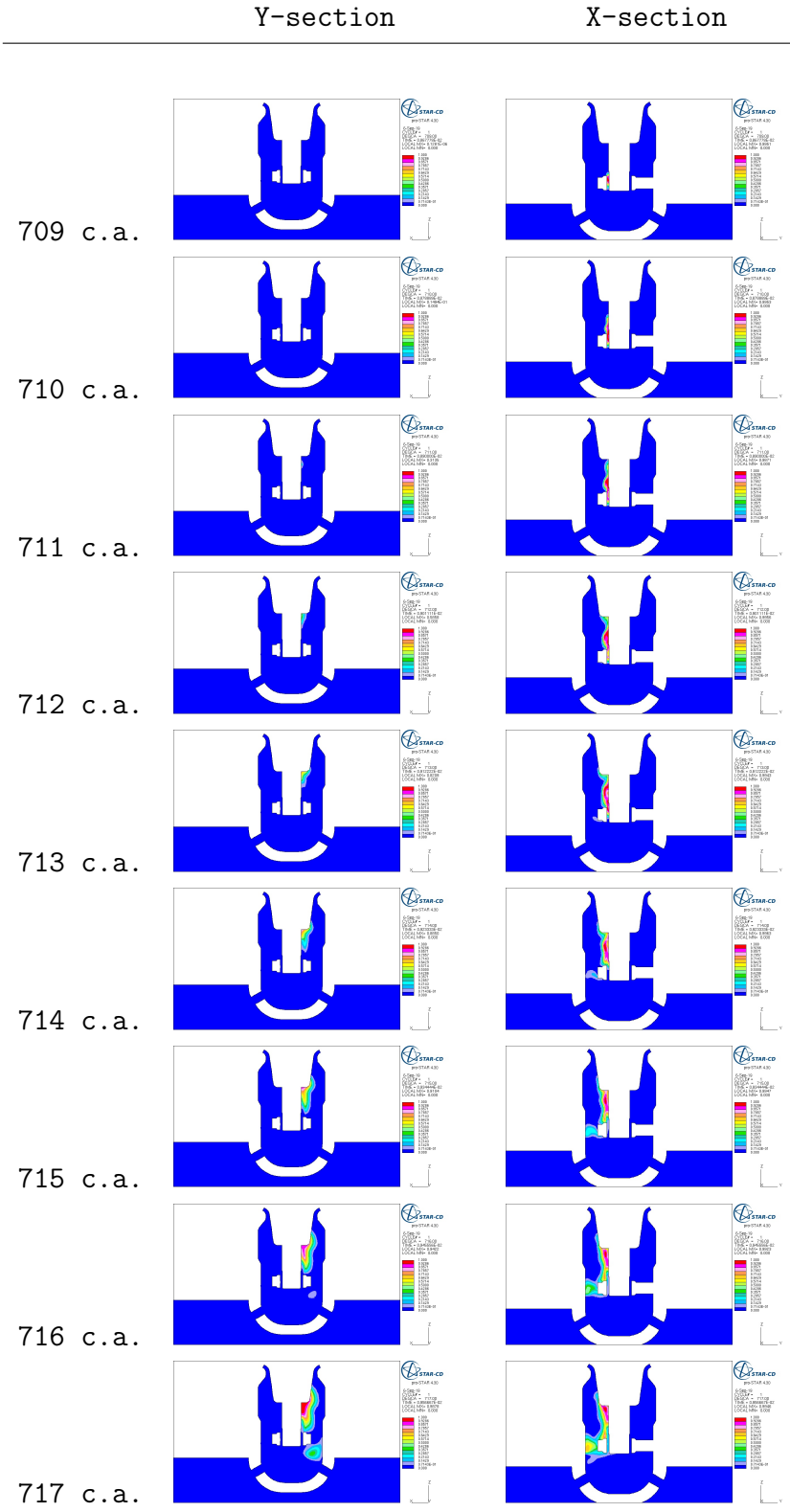

Figure 4.10: Flame front evolution for Simulation 3

4.2.2 Influence of α

α is an empirical coefficient multiplying a production term in the Flame Surface Density equation (Equation 3.21). It is also present inside the expression for C (Equation 3.24), the term in FSD equation taking into account flame quenching at the walls and the flame chemical timescale. As one can easily check with a rapid look to those equations, α has a positive effect on the FSD, meaning that the latter is proportional to α. In Simulation 5 the value of α was raised to 2. According to many papers (for instance [5]), its value should range in the order of magnitude of 1, so 2 is a reasonable value. The pressure curve of Simulation 5 shows no detachment from the no-combustion curve until about 728 c.a.. This fact can be interpreted saying that combustion is very slow: the flame has reached a volume not yet big enough to affect the average pressure value inside the whole cylinder. In other words, up to 728 c.a., the pressure raise due to combustion has probably happened, but only in a restricted area. The pressure wave in fact requires time to propagate, and this is even more evident in a two-chambers environment. This hypothesis on the course of the events makes sense if one refers to the mechanism governing the early flame and the flame propagation in this CFD environment. FSD equation in fact accounts mostly for the flame propagation in the late phases. The attempt of tuning α though is not a mistake: ISSIM's main feature is to govern the early flame kernel by means of FSD and not zero-dimensional ways (see Chapter 3.3.3). Nevertheless, no effect of α on the early phase is shown by the pressure curve between Simulation 5 and 3: increasing α did not affect pressure directly. In the late part of combustion, i.e. the right part of the curve, pressure reaches an higher peak with respect to Simulation 3. Looking to the AHR curve one can see how the peak value is anticipated from Simulation 3 (starting setup, not tuned) by 7.15 c.a.. The start of combustion in Simulation 5 happens at 736.4 c.a., which is 4.45 c.a. before Simulation 3. This anticipation is very slight, and not so influential as well. The two IHR curves differ mostly because they diverge, which is due to their different slope. The anticipation of the AHR peak with respect to Simulation 3 as well, proves how α affects more the second phase of the flame. Table 7.2 shows how small is the influence of α on the AHR (Figure 4.12): for Simulation 5 the peak value is 160 J/deg at 748.55 c.a., which is smaller of about the 43.83% with respect to the Experimental one and delayed by

19 c.a.. The effect of α was evaluated also in more complex models. In Simulation 12 α has been set to 1.8, the laminar flame speed model is still a table, and the effect of anticipating the ignition timing was tested, while in Simulation 11 the Gülder correlation has been used, and α has been set to 2. Simulation 12 is a complex setup where Extended data have been set, electrodes are set adiabatic and ignition is anticipated to 700 c.a., thus it's difficult to understand the effect of the single α parameter. Simulation 11 was run with the purpose of understanding the cause for the late raise in pressure (slow combustion). We can compare the results with the ones of Simulation 8: in both the Gülder correlation has been used. The pressure curve of Simulation 11 shows a pressure raise at about 725 c.a., while Simulation 8 pressure curve detaches the no-combustion at about 723 c.a.. Here however, the difference between two curves is not much, except from a slightly higher peak for Simulation 11. The positive effect has been enhanced by the adiabatic walls set in Simulation 11 (see following section 4.2.3). Summarizing, one can say the flame propagation phase is influenced by α and not the early phase.

It is a common situation that combustion in a CFD simulation is faster and more efficient than in the real case, due to non predictable events happening in real process (dissipation, frictions etc.). The coefficient α thus is most likely reduced than raised, to slightly decrease the flame propagation speed in the simulation. This is allowed since α is an empirical and non dimensional coefficient which needs to be tuned based on the very case. This fact, combined to the very small change of the simulation results with respect to the standard one (with $\alpha = 1.6$), led to the conclusion that α has not a strong influence in this case study, and it shall be used for small final tunings once a robust model has been built.

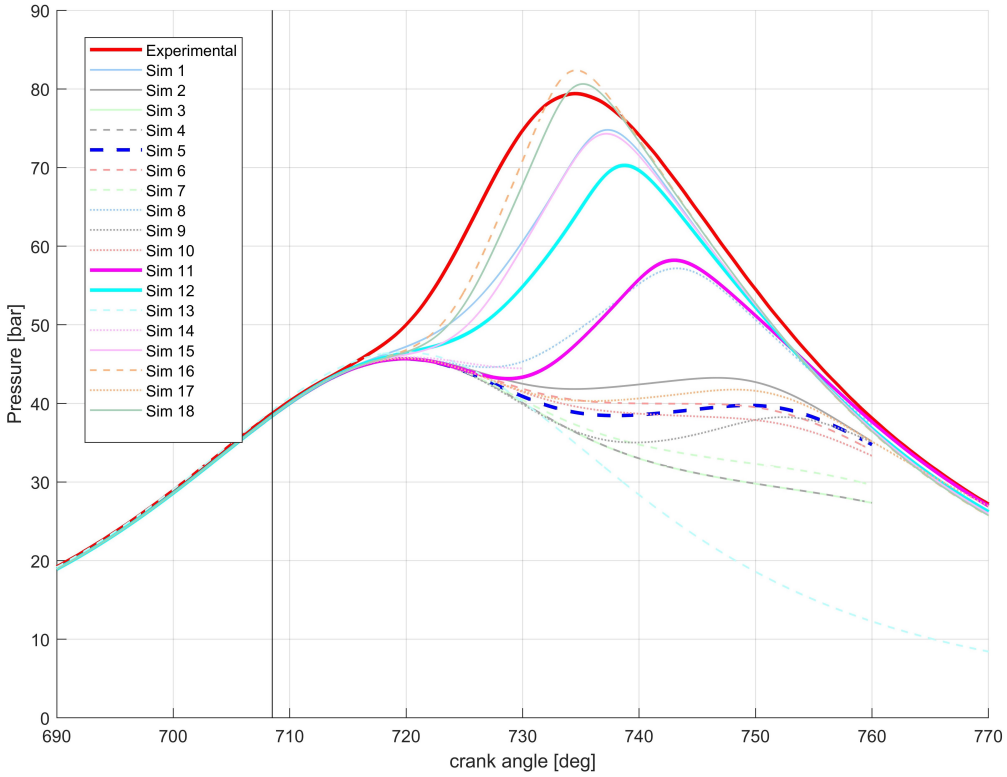

Figure 4.11: α pressure curve

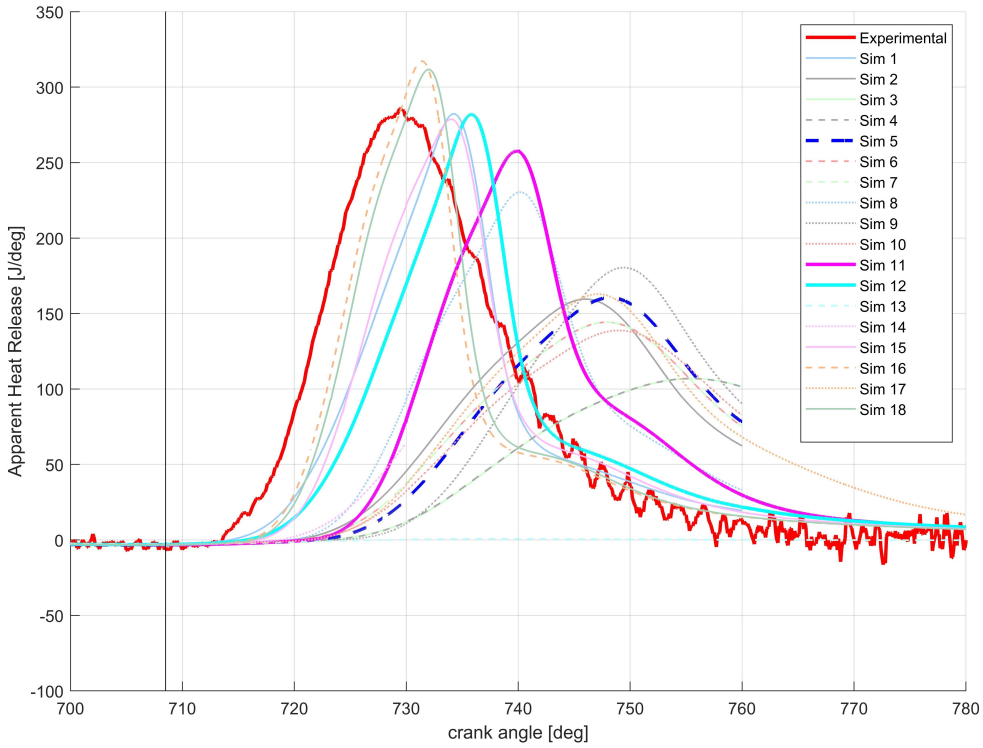

Figure 4.12: α AHR curve

4.2.3 Influence of boundary conditions

The lack of knowledge of thermal boundary conditions is still a challenge in CFD engine simulations [12]. The options available in Star-CD software are:

- Adiabatic wall
- Fixed wall
- Mapped wall

In order to keep the complexity of the modelling as low as possible, at least at this preliminary stage, boundary conditions of the walls are not mapped for all the engine cycle as a function of the crank angle, but they are considered as constant, and they are taken from experimental measurements. The situation is different for the

Boundary conditions	
combustion dome	480 K
piston crown	500 K
cylinder wall	483 K
intake valve surface	Adiabatic
exhaust valve surface	Adiabatic

Table 4.3: Boundary conditions

spark plug electrodes. The temperature of these walls is very influential as long as right after the ignition timing, the first flame kernel develops in the spark gap, and its external surface touches first the electrodes walls. From the very ignition time instant, to the instant in which the kernel touches the walls, it passes an extremely short time interval. That means flame kernel is getting bigger with a certain growing rate governed by laminar flame speed and, being in the early phase, this rate can be influenced by the temperature of the walls. Let us approximate this early flame front to be shaped as a sphere propagating from the center of the spark gap. In the time instant at which the diameter of the sphere equals the dimension of the spark gap, flame front begins to touch the walls: we can observe from post processing (Figure 4.13) that less than 0.5° crank turn is sufficient. From then on, an increasing portion of the sphere surface is in contact with the cold wall. If the walls

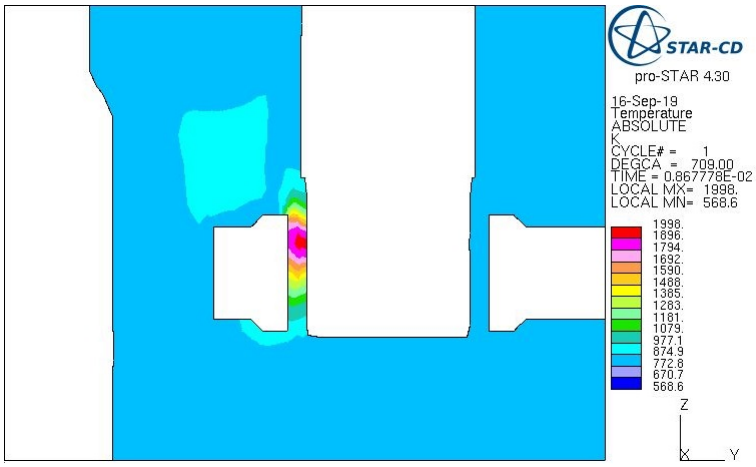

Figure 4.13: Early flame temperature: the peak temperature is 1998 K. The hot flame front (hottest zone of the flame) can be quenched by the electrodes. Ignition took place at 708.5 c.a., so less than 0.5° ($5.556E-05$ s) before the snapshot.

were too cold, the flame quenching could slow down the flame kernel propagation, affecting the whole flame propagation. It's a good approximation for the electrodes as well, to consider the wall temperature as constant. The spark plug electrodes of course are not an easily accessible zone to measure the wall temperature, so there is not a correct reference value representing faithfully the reality. Therefore, at the beginning of the work, this boundary condition was not thought to have a very high influence on combustion as long as its value was close to a reasonable one. The tuning in that phase has just been limited to a small change in the setup (Table 4.4).

	Anode [K]	Cathode [K]
Setup 1	850	900
Setup 2	950	950

Table 4.4

The most significant effort to verify the influence of electrodes' temperature is represented by Simulation 7, in which the walls have been set adiabatic. The flame front is the hottest part of the whole domain of the combustion reaction, and depending on equivalence ratio its temperature ranges between 1900 K and 2000 K. That means a wall at 950 K causes the quenching of the flame by absorbing heat

from it and cooling it down. The result of Simulation 7 proves this reasoning: the peak temperature in the flame region is 1998 K. Although the heat exchange is strongly enhanced by convection caused by the turbulent flow field, and from the high wall-fluid temperature gradient, it requires some time to take place. Setting the wall adiabatic in fact, only slightly influenced the macroscopic quantities in the early phase. The positive effect of having adiabatic electrodes' walls is evident from 730 c.a. on. For both thermal conduction and thermal convection, the heat power [W] is proportional to temperature gradient and exchanging surface (we can refer for example to such a law 2.10). Heat lost to the walls [J] thus increases with the time. This is clearly visible in Figure 4.16: IHR is the energy released in combustion minus the losses through the walls 2.11. The discrepancy between Simulation 7 curve and Simulation 3 (standard setup) curve can be said to increase linearly with the crank angle, meaning that less and less heat is lost to the electrodes' metal walls. AHR for Simulation 7 and for Simulation 3 should be, according to this reasoning, distant each other from a constant segment. Considering that AHR takes into account the global heat loss through all the engine walls, that the flow field is not constant (affecting the convection), and that temperature varies with the flame front motion within the cylinder (affecting 2.10), it's not easy to see the effect of the adiabatic electrodes in the AHR plot. However, looking to the pressure curve, and comparing Simulation 7 with Simulation 3, confirms that the effect of adiabatic walls is not very important. In Simulation 11 and Simulation 12 as well, electrodes have been set adiabatic. Let us focus on Simulation 11, and compare it with Simulation 8: their setup are very similar (Table 4.3), the main difference is the adiabatic wall in Simulation 11. As already discussed in the previous section, the difference between the two pressure curves is very slight, while the AHR peak of Simulation 11 is 27.88 J/deg higher than in Simulation 8 (258.316 J/deg against 230.441 J/deg). Still, it's not appropriate to consider the electrodes' boundary condition as a very determining parameter for the whole model: peak values for pressure in all the simulations described are in the best case smaller of the 26.69% with respect to the Experimental value (Simulation 11), and very delayed (+8.50 c.a. in the same case). Furthermore, one can see in Table 4.9 how the start of combustion of Simulation 7 is at 735.05 c.a. and of Simulation 11 at 732.01 c.a., against the Experimental start of combustion

722.4 c.a., meaning again that despite the slight improvement, flame is still too late in the early phase to be compared to the experimental one.

In the next section it will be discussed how the most influential parameter is probably laminar flame speed, which governs early flame phase as well. Thus, the heat exchange with the electrodes affects strongly the early phase, but even if this section shows how small its influence is, still the problem may be in the early flame phase.

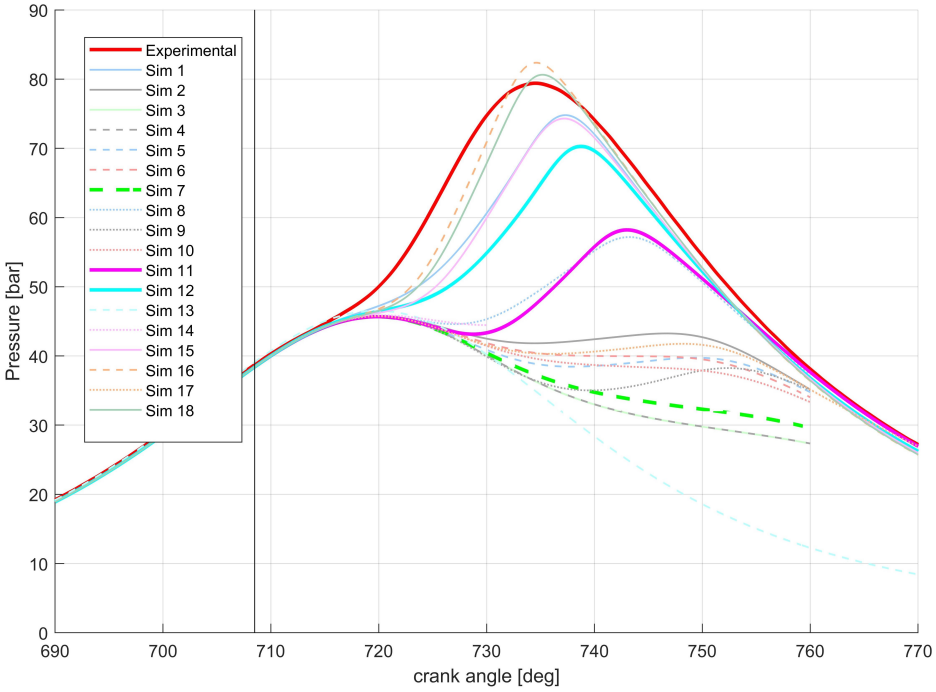

Figure 4.14: Pressure

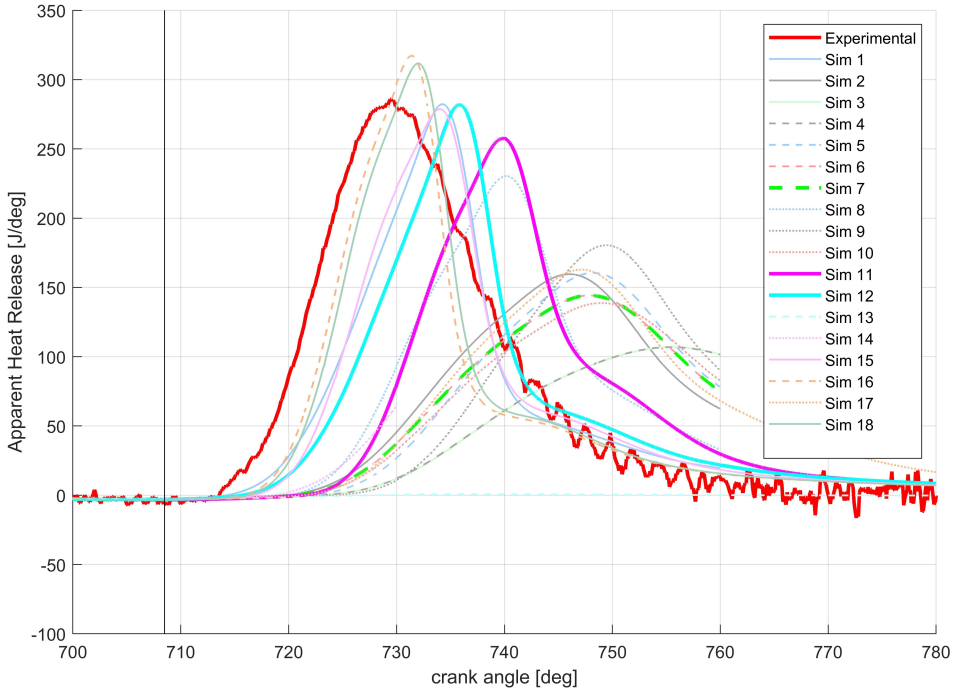

Figure 4.15: Apparent Heat Release

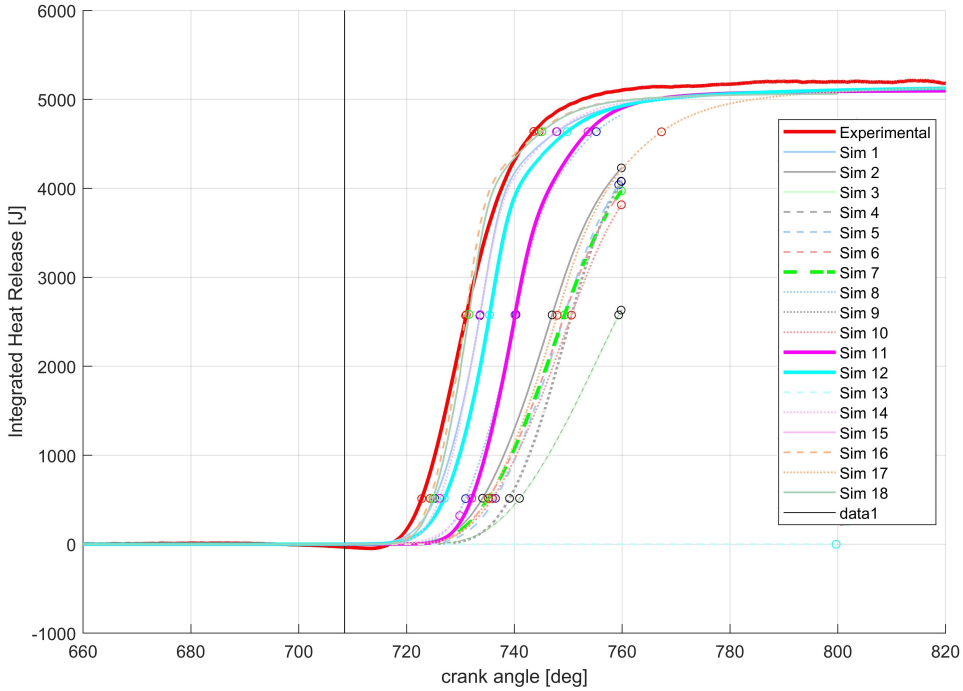

Figure 4.16: Integrated Heat Release

4.2.4 Influence of laminar flame speed

The early phase of combustion in the first simulations is slower than in the experimental one. It can be easily deduced looking to the point at which the pressure curve detaches from the one without combustion, in both the simulation and the experimental curves. Let us consider Simulation 3 and the Experimental data: the delay of the pressure raise in the simulation corresponds to a late start of combustion. This is better noticeable in Figure 5.6, where combustion start is represented by the 10% of mass fraction burnt. The experimental case combustion start corresponds to 722.40 c.a., the Simulation 3 one corresponds to 740.85 c.a., which means a 18.45 c.a. delay. The slope (and the peak value) of Apparent Heat Release curve as well is lower than in the experimental case: this is another macroscopic effect meaning that combustion in simulations is a globally slower process than in experimental case. *proSTAR* post processing snapshots of the flame were useful to understand the cause of this phenomenon, despite the absence of optical access to the real engine i.e. of a direct comparison. As already mentioned in Chapter 3.3.1, the *flame front expansion speed* or real *Observed speed* is the sum of the laminar flame speed S_L and a transport term. Moreover, in the early phase of combustion, the first flame kernel can be said to develop with laminar flame speed S_L. Let us also recall the mechanism governing flame propagation in ECFM-3Z: Flame Surface Density transport equation (Equation 3.21). S_L has a strong effect on FSD, accordingly to the previous physical analysis.

Having established that laminar flame speed was one of the main reasons for the big simulations-experimental discrepancy, the step forward was to find the best method to approximate S_L. The alternatives available in Star-CD using ECFM-3Z are:

- S_L tables
- DARS libraries
- Correlations

S_L tables and DARS libraries are database files listing laminar flame speed values as a function of equivalent ratio, pressure, temperature and EGR percentage for a given fuel composition. DARS libraries can be created by the user with DARS software [18], for each specific case study. Correlations have been illustrated in Chapter

3.3.2. One S_L table for natural gas supplied by the software is the *STAR-CD Open* table. It contains values of laminar flame speed in the points given in Table 4.5.

Variable	Range
temperature points: 10	300.0 - 1200.0 K
pressure points: 9	1 - 200 bar
EGR points: 7	0.0 - 1.0 mol%
ϕ points: 23	0.0 - 5.0
Fuel fracion points: 1	1.0

Table 4.5: *STAR-CD Open* table structure.

In all the intermediate points the laminar flame speed is computed trough interpolation. While using a table means reading the flame speed values from a database file, the use of a correlation demands greater attention. In this work both the methods have been tested.

Let us compare Simulation 3, Simulation 8, and Simulation 9. They represent the three methods for computing the LFS, respectively *STAR-CD Open* table, Gülder correlation and Metghalchi correlation. Despite *STAR-CD Open* table should contain by definition all the LFS values for each situation (Table 4.5), the result of Simulation 3 are not close to the Experimental case. Analyzing this fact, the explanations could be several. The Natural gas library for example could not fit perfectly with the fuel in use, if the components percentage are different from the standard Natural gas to which the table refers. For example, some minor components of Natural gas like propane, ethane etc., are more reactive than methane, generating a globally different combustion phenomenon if they are present in different percentages. Also, to a different mixture corresponds a different specific gas constant $\tilde{R}$ ($\frac{molar\ gas\ constant\ R}{molar\ mass\ of\ the\ gas\ M}$). One other cause could be that the correction for LFS near spark plug is not set properly (see following pharagraphs). Simulation 8 makes use of Gülder correlation for LFS. This case is the one among the one cited in which a single variation influences the combustion process radically. Let us look to the pressure curve: Simulation 8 shows a relevant pressure raise with a peak of 57.1809 bar, which differs from the experimental one from -22.2270 bar (-27.99%). This value is achieved at 743.25 c.a., namely 8.75 c.a. after the Experimental peak. Despite

the apparently far results, looking to the shape of the pressure "bell" one can see how similar it is to the Experimental one, but still with a large delay. The still high discrepancy between the values of the peak and of the whole curve in general, can be explained with the delay, intended as the time interval the flame kernel takes before to start propagating. The more is the ignition delay, the more the piston is close to Top Dead Centre when combustion starts, and in this case even compression stroke is already over. With the piston starting to move downwards, and thus the volume increasing, the ignition timing becomes inappropriate (insufficient) and combustion never becomes very effective as it is supposed to be. Nevertheless, one positive effect of using Gülder correlation can be the pressure raise starting at about 725 c.a., still very late but better than in the other cases described so far. Simulation 9 (in which Metghalchi correlation has been used) as well shows the positive effect of using a correlation for LFS. The overall results of the simulation show a lower combustion intensity with respect to the case with Gülder correlation: pressure peak is 11.5255 bar lower than Experimental, and also AHR peak is 49.888 J/deg lower and delayed. Combustion start for the two Simulations 8 and 9 is respectively at 730.90 c.a. and 739.00 c.a. versus the 722.4 c.a. of the Experimental case.
The model so shaped then, is not yet suitable to represent the Experimental case but, especially comparing the results of Simulations 8 and 9 with the ones of Simulation 3, one can conclude that laminar flame speed is a strongly influential parameter in the combustion modelling of this case study. None of the attempts though showed relevant improvements in the early phase of combustion (close to TDC).

Influence of Extended data (ISSIM)

ISSIM model has many calibrations parameters which need to be set based on the flow field conditions at spark timing. The value of these parameters has to be specified in the section *Extended data* of *star.prob* file. Star-CD support (*The Steve Portal* website [17]) provides some standard setups for specific flow field conditions, depending on the *PINI = Mean Absolute Pressure at Start of Ignition*, *TINI = Mean Temperature at Start of Ignition* and *TKEINI = Mean Kinetic Turbulent Energy at Start of Ignition*. The parameters to adjust have to do with the ignition (ISSIM) and with the laminar flame speed model as well. The following is an overview of all

these parameters one can tune depending on the LFS model chosen.

Laminar flame speed table When using a laminar flame speed table, it's ISSIM to be in charge of the LFS near spark plug modification. The energy released by the spark provokes a raise of the LFS. The correction is the following (see Chapter 3.3.3):

$$S_L^{eff} = S_L^0 \cdot 0.5\left[1 - \frac{4\delta_L^0}{l_{spk}} + \sqrt{\Delta}\right] \tag{4.2}$$

$$\Delta = \left[\frac{4\delta_L^0}{l_{spk}} - 1\right] + 4\left[\frac{4\delta_L^0}{l_{spk}}\right]\left[1 + \frac{E_{ign}}{400 c_p^b m_b}\right] = \left[\frac{4\delta_L^0}{l_{spk}} - 1\right] + 4\left[\frac{4\delta_L^0}{l_{spk}}\right]\left[1 + \frac{\Delta T_b^{ign}}{400}\right] \tag{4.3}$$

$$S_L^{eff} = S_L^0 \cdot \left[1 + (S_L^{corr} - 1) \cdot exp - \left(2\frac{|x - x_{spk}|}{l_{spk} \cdot SPINFEXT2}\right)\right] \tag{4.4}$$

$$\Delta T_b^{ign} = min\left(\frac{E_b}{c_p^b m_b}, TEMPMAXSLCORR\right) \tag{4.5}$$

Where Equations 4.2 and 4.3 represent the correction itself, and Equations 4.4 and 4.5 are the *Extended data* involved. The setup recommended by Star-CD support is $SPINFEXT2 = 8$ and $TEMPMAXSLCORR = 20000$. Two simulations have been run using the standard setup recommended by Star-CD support (Simulations 10 and 12). In the both of them *STAR-CD Open* table (for laminar flame speed) has been used. Simulation 12 differs from 10 for the anticipated ignition point at 700 c.a. (topic discussed in Chapter 4.2.5). Simulation 10's results demonstrate the importance of setting the proper configuration while using a laminar flame speed table. Comparing its pressure curve with Simulation 3's one, one can see how pressure 10 begins to increase more after about 728 c.a.. Despite the improvement is not enough to have a good model to approximate Experimental data, it's possible to state the importance of Extended data, referring to the fact that the same LFS table has been used in the two simulations. The correction of LFS near spark plug is thus very influential in the overall process, considering that in the rest of the domain the flame speed computed comes unchanged from the table. As for the heat exchange through the electrodes, it's clear that this correction alone is not sufficient to obtain a faithful model.

Gülder correlation For general applications such as air-to-fuel equivalence ratio far from 1, this is the recommended correlation. No adjustments are allowed using this correlation.

Metghalchi and Keck correlation When this correlation is used, a correction for the laminar flame speed computation is available in Star-CD:

$$S_L = S_{L0} \cdot \left[\frac{T_{mel}}{300}\right]^{\alpha} \cdot [P_r]^{\beta} \quad with\ P_r = \frac{P_{abs}}{le^5} \tag{4.6}$$

$$\begin{cases} \beta = \beta_0 - 0.08\left[\frac{(P_r - PRTRANSL)}{ULAM3} + \frac{PRTRANSL}{ULAM3BELOW}\right] & if P_r > PRTRANSL \\ \beta = \beta_0 - 0.08\left[\frac{(P_r - PRTRANSL)}{ULAM3BELOW}\right] & if P_r < PRTRANSL \end{cases}$$

The *Extended data* concerning this correlation that one can tune are:

- *ULAM3*: Adjustment of pressure ifluence in laminar flame speed correlation for $P_r > PRTRANSL$ (Default value=40)
- *ULAM3BELOW*: Adjustment of pressure influence in laminar flame speed correlation for $P_r < PRTRANSL$ (Default value=60)
- *PRTRANSL*: Transition pressure for application of ULAM3 or ULAM3BELOW in the laminar flame speed correlation (Default value=0)

PRTRANSL is initially set to 0, which means the correction is not activated. As suggested by Star-CD support [17], it should assume the value of the Mean Cylinder Pressure near spark ignition timing but, for the purpose of tuning the model, different values have been tried. It makes sense as long as it represents the threshold up to which the correction is active. The group of Simulations 15, 16 and 18 represent the sequence of adjusting the LFS correction, in order for the computational results to match as much as possible the experimental ones (a similar pattern has been followed in the work [10], presented in STAR Global Conference 2016). Let us firstly make a comparison between the results of Simulation 15 and Simulation 9: in both Metghalchi correlation is the LFS model. The pressure curves apparently look very different: Simulation 9 reaches a peak value of 45.6554 bar @ 719.82 c.a., versus the Simulation 15 peak of 74.3035 bar @ 737.20 c.a.. Responsible of this

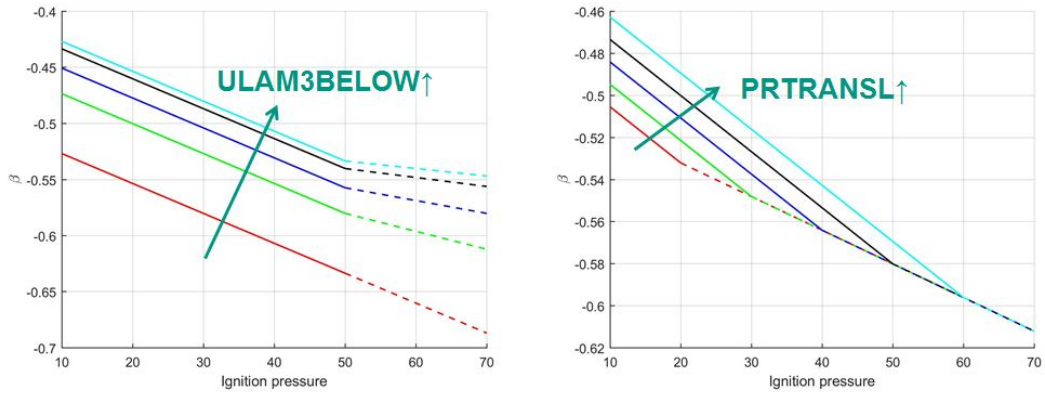

Figure 4.17: Qualitative representation of the influence of *PRTRANSL* and *ULAM3BELOW* on β.

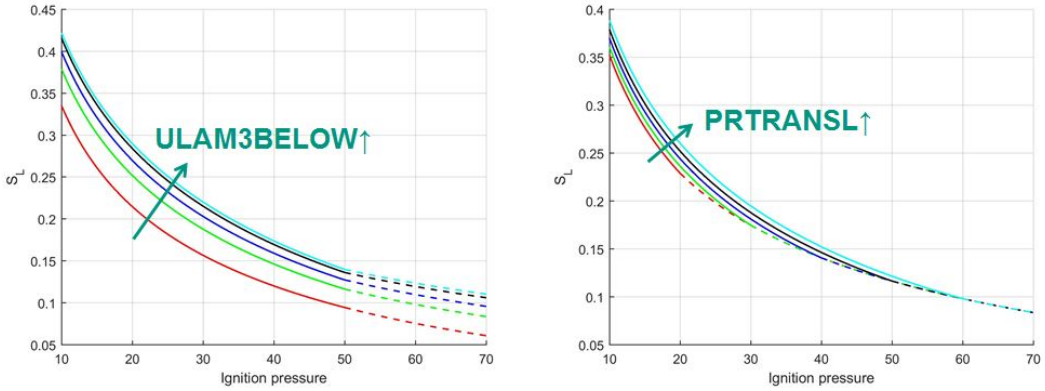

Figure 4.18: Qualitative representation of the influence of *PRTRANSL* and *ULAM3BELOW* on S_l.

drastic difference is the only difference in the two setups i.e. the Extended data, meaning the adjustment of the correction near spark plug parameters in Simulation 15. Namely, $PRTRANSL = 383959$ which is the mean cylinder pressure at spark time (read from previous simulations data, which show nearly the same pressure value before ignition, equal to the Experimental one), $ULAM3BELOW = 50$ and $ULAM3 = 45$ (standard value). The effect of $ULAM3BELOW$ of LFS can be seen in Figures 4.18 and 4.17: by increasing it, LFS curve as a function of pressure becomes steeper and steeper, concluding that generally speaking, higher LFS values correspond to a fixed pressure value. It is possible to see in Figure 4.19 that pressure curve 15 is not close enough to Experimental one to consider this model suitable. Again, in the early phase pressure and consequently AHR and IHR do not detach from the no-combustion curve until about 720 c.a.. In Simulation 16 and

Simulation 18 the tuning of Extended data has been performed to obtain higher LFS values after the correction, with the purpose of checking the importance of LFS over the early phase. For this reason $ULAM3BELOW$ has been raised to 100 while keeping $PRTRANSL$ constant in Simulation 16, and finally they have been set to $ULAM3BELOW = 70$ and $PRTRANSL = 55$ in Simulation 18, while keeping $ULAM3$ constant in both. These values are the consequence of a tuning process aiming to match the pressure's peak value and coordinate. Let us consider Simulation 18 as the final result after tuning: the pressure's peak value is 80.6327 bar @ 735.20 c.a., which is 1.2247 bar higher and 0.70 c.a. late with respect to Experimental case. Pressure detaches from no-combustion curve at about 720 c.a., which is an acceptable result but still delayed with respect to Experimental case. Apparent Heat Release peak is 311.696 J/deg @ 732.00 c.a., which is 25.9269 J/deg higher and 2.50 c.a. late with respect to the Experimental case. This is easily understandable considering the dependence of AHR on pressure (Equation 2.9). Pressure "bell" of Simulation 18 is slightly narrower than the Experimental one. Looking to the fuel burnt curve we have a representation of the combustion speed: it starts at 724.83 c.a. and its duration is of 18.32 c.a., with the half of fuel burnt in correspondence of 731.45 c.a.. Experimental combustion, referring to the fuel burnt as well, has a duration of 19.50 c.a. starting at 722.4 c.a.. This is consistent with the narrower shape of Simulation 8's pressure curve, in which probably the LFS computed is higher than the Experimental one.

Nevertheless, it's not trivial to state the consistency of using Metghalchi correlation in extremely lean conditions (see Chapter 3.3.2), operating a drastic correction. A positive feedback comes from Figure 4.18: by varying the correction threshold $PRTRANSL$, only the laminar flame speed computed below that value is altered, while beyond it LFS is computed through the standard expression 3.22. Having apprehended that the validation of the model problem might be in the early phase of combustion, it makes sense to have a correction for low pressure conditions, corresponding precisely to early phases of the flame. The results show how intense is the effect of an higher laminar flame speed (see post processing images showing the flame front propagation, Figure 4.24) on the pressure evolution, in terms of ignition delay as well as slope and peak value. Moreover, for the purpose of investigating the

flame propagation due to geometric features, the main purpose is to have a suitable model, i.e. to represent the overall combustion phenomenon in a way which is fast enough to reproduce the Experimental behaviour.

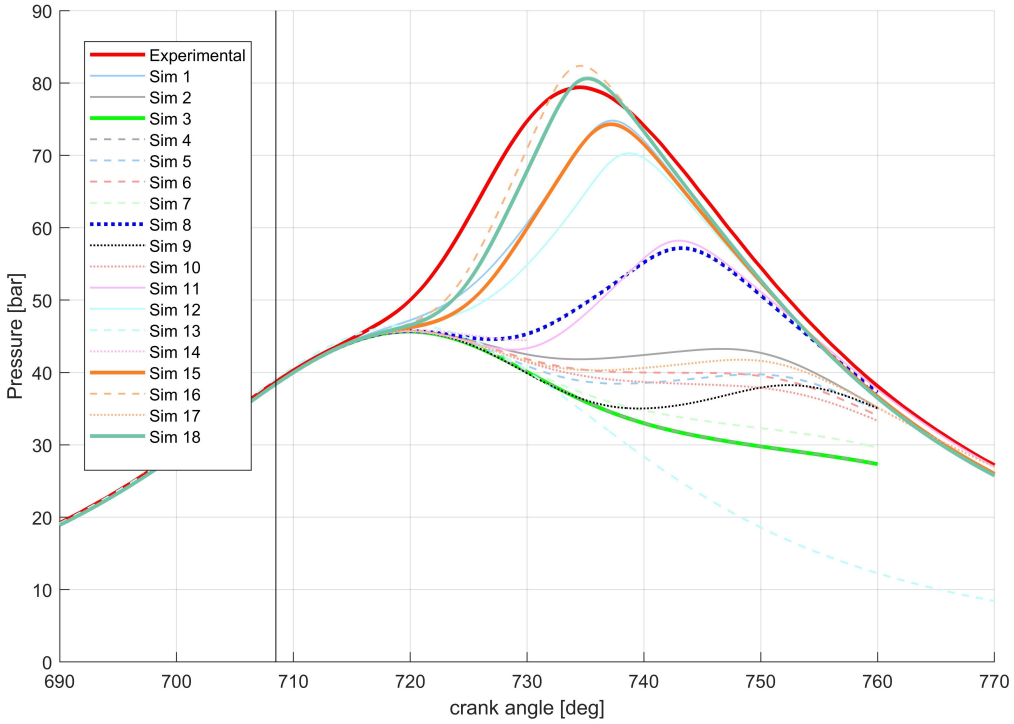

Figure 4.19: Pressure

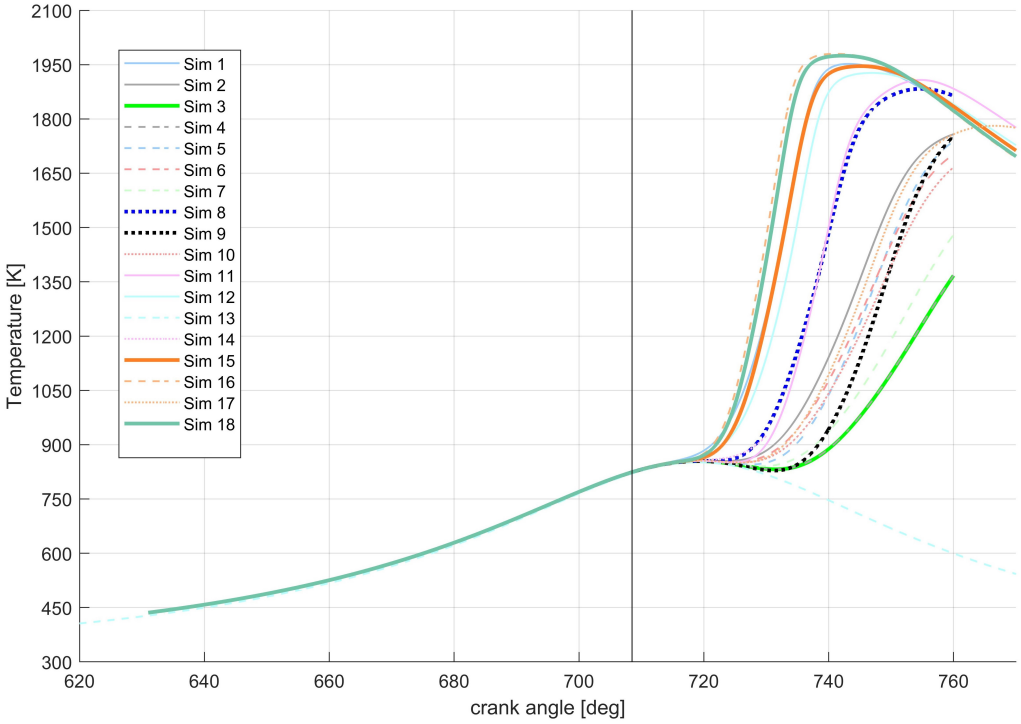

Figure 4.20: Temperature

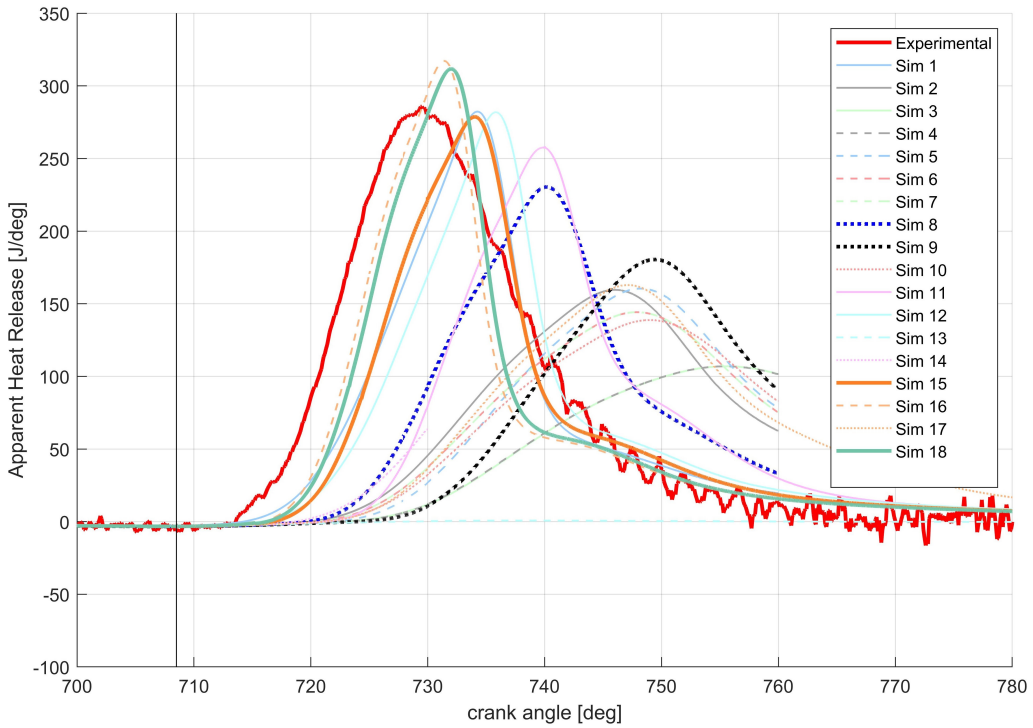

Figure 4.21: Apparent Heat Release

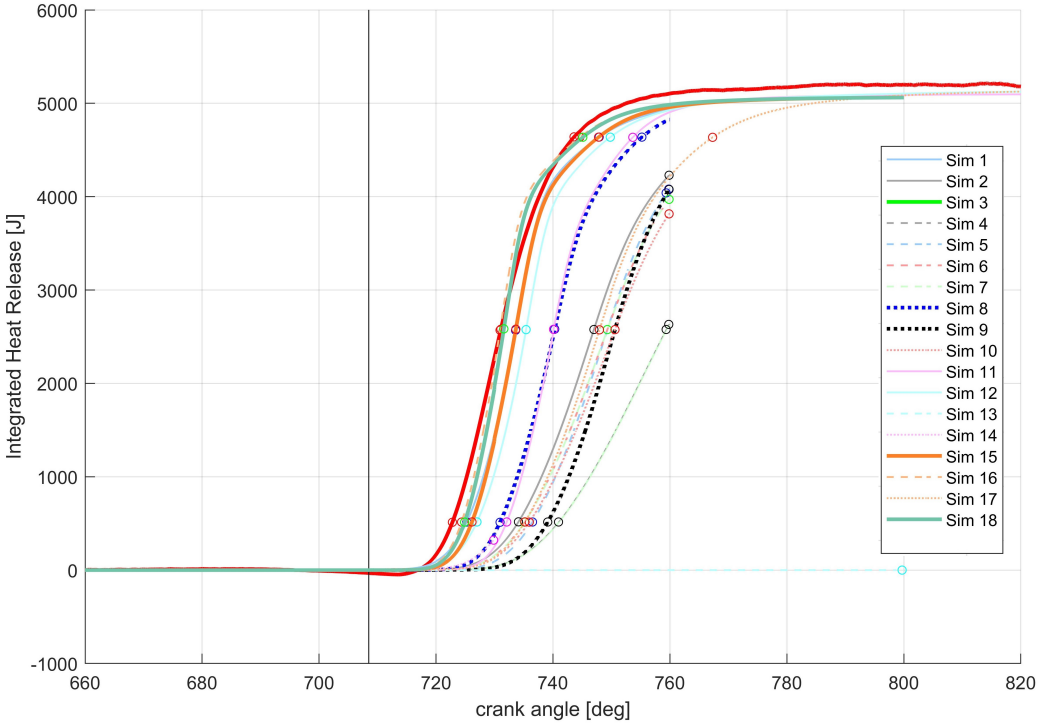

Figure 4.22: Integrated Heat Release

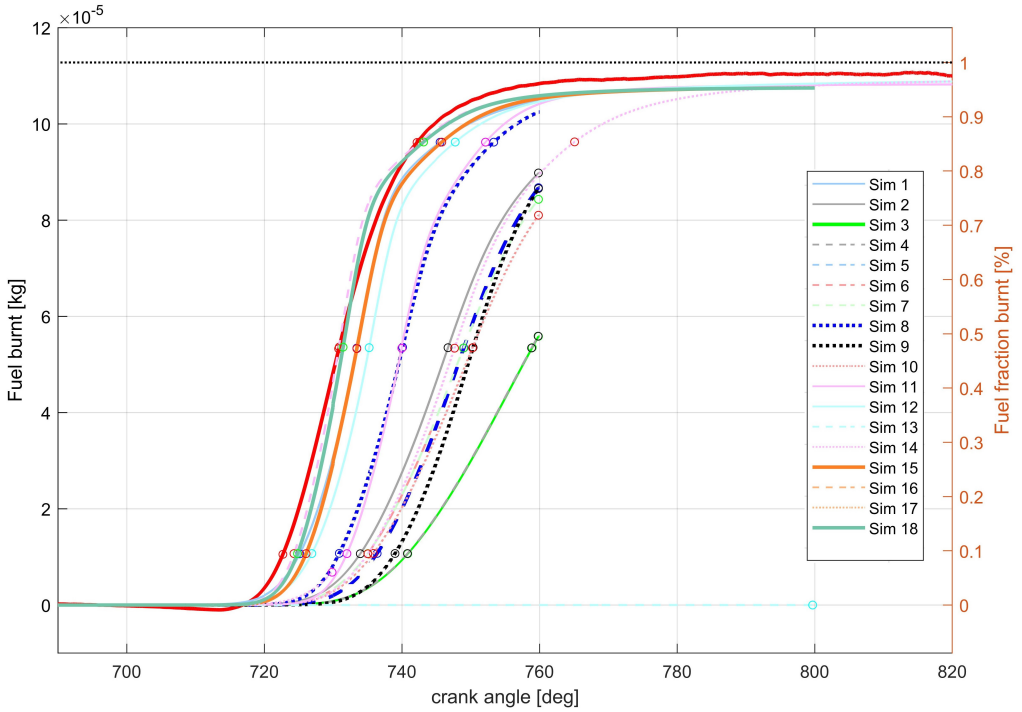

Figure 4.23: Fuel burnt

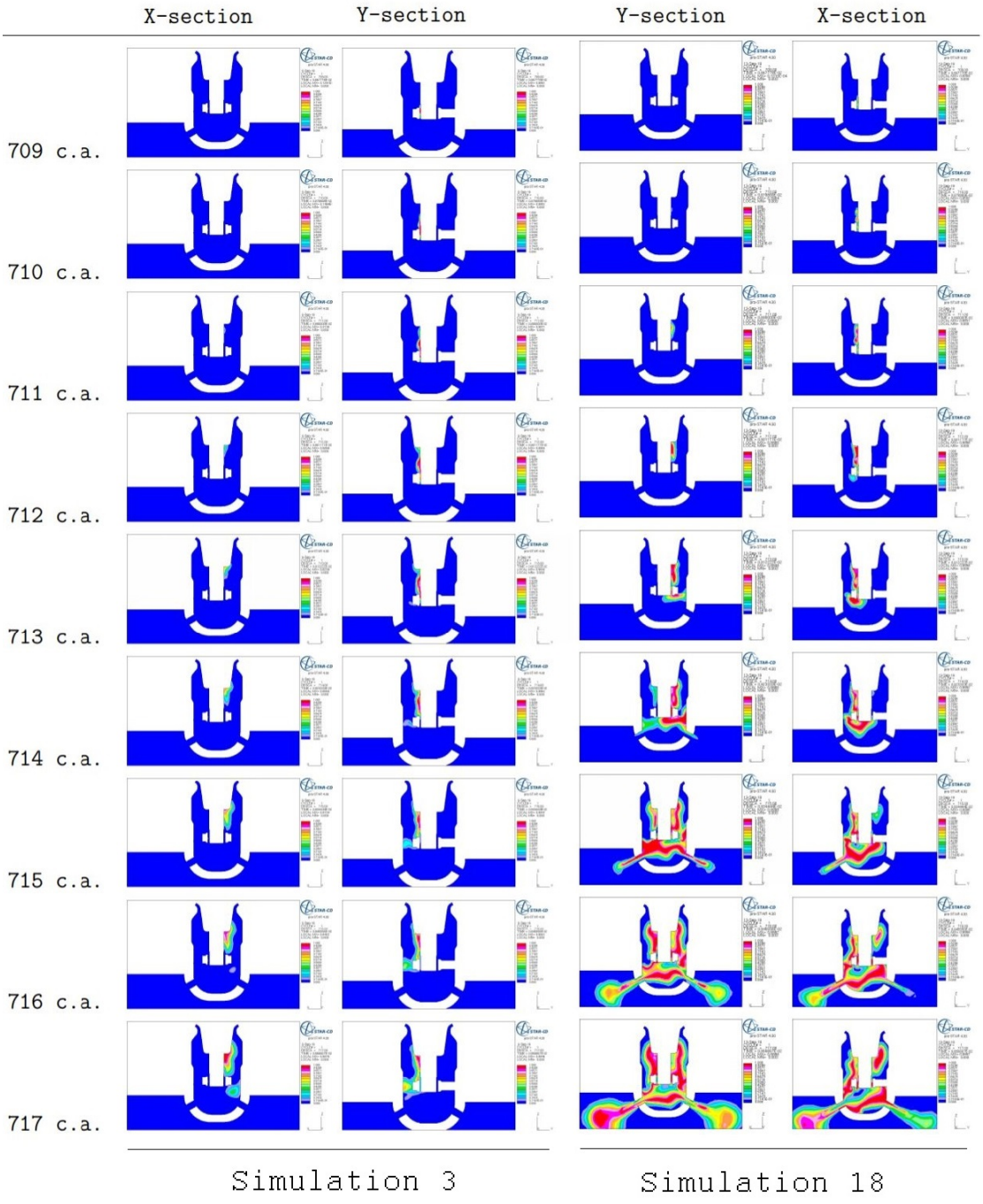

Figure 4.24: Flame front evolution for Simulation 18

4.2.5 Influence of ignition energy

As already mentioned in the methodology section (beginning of Chapter 3.3.3), the software activates ignition only when it recognizes the correct conditions for initiation: $E_{ign}(t) > E_{crit}(t)$. The ignition energy E_{ign} yet is a fraction of the secondary circuit energy E_s. The secondary circuit of a spark plug is an R-L circuit of indunctance L_s in the order of magnitude of 10 mH and most considerable resistance R_s represented by the spark body itself of order of magnitude of 10000 Ω. The time dependent law describing the circuit discharge is:

$$\frac{d}{dt}E_s(t) = -R_s i_s^2(t) - V_{spk} i_s(t) \tag{4.7}$$

Some losses in terms of voltage drop take place in the spark gap: electrodes voltage drop (V_{cf} at cathode and V_{af} at anode), which is maximum in glow phase heats the electrodes' walls, losing a part of E_s, and ionic potential of the cathode voltage drop V_{ion}. The fraction of energy released to the fluid is about $E_{ign} \approx 0.6E_s$.

StarCD user guide [21] recommends to use values for E_s not higher than 0.1 J but ISSIM method allows to set multiple ignition locations at the same crank angle. In Simulations 1 and 2 the attempt of setting multiple ignition points was tried (Figure 4.25). Simulation 1 moreover was run anticipating further the ignition timing to 700 c.a.. The energy value used was 0.1 J to achieve the most intense ignition conditions allowed by the software.

To better and more heterogeneously fill the spark gap with flame sources, the 4 ignition point were set at far apart sites, at different heights within the gap. Coordinates system is placed 1.7 cm below the cathode basis:

Ignition point	x [cm]	y [cm]	z [cm]
Point 1	-1.0554	1.0554	2.9
Point 2	1.0554	1.0554	2.0
Point 3	0	-1.4925	2.4
Point 4	1.0554	-1.0554	2.9

Table 4.6: Multiple ignition point coordinates.

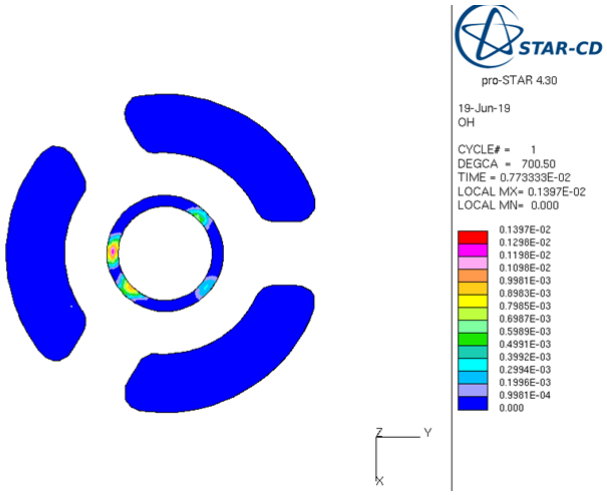

Figure 4.25: Post processing snapshot of Simulation 1 representing the OH radical map at 700.5 c.a., section normal to the z direction displaying the domain of fluid in the spark gap and in the rest of the prechamber (white ring represents the anode). The 4 ignition points are visible.

Let us compare the results of Simulations 1 and 2 to the ones of Simulation 3. Pressure of Simulation 2 reaches much lower values than Simulation 1, and the pressure peak due to combustion is achieved very late with respect to TDC (around 747 c.a.), so it is even lower than the compression stroke peak (720 c.a.). It is immediate to attribute the cause to the different ignition timings set. The ignition timing at 700 c.a. of Simulation 1 allows the flame to develop firstly when the piston is approaching the TDC, while in Simulation 2, due to the slow combustion issue of the model, flame starts to propagate when volume is already increasing. Simulation 1 can be considered as good approximation of the Experimental case: the peak pressure is 74.7970 bar @ 737.30 c.a. versus the 79.4079 bar @ 735 c.a. of the Experimental. The AHR curve as well is consistent, with a peak value of 282.274 J/deg differing by only -1.22% from the Experimental one, but still delayed of 4.75 c.a.. Consequently the IHR and fuel burnt curves show the same slope of the Experimental ones, again being slightly delayed. This is why one can consider Simulation 1's combustion shifted by 4÷5 c.a. with respect to Experimental one, in terms of progress (fuel burnt). Despite the benefit of this approach showed by the analysis of the results, some doubts on the validity of this model raised. Spark is by definition a concentrated discharge of energy which has been routed towards a

point of the spark gap. It is not physically possible that multiple discharges happen at the same time, unless several spark plugs are installed in the engine. Moreover, increasing the number of ignition points means multiplying the amount of energy released, and not splitting it among the ignition points. Considering 0.1 J like a threshold recommended by the manuals, the validity of overcoming it is not verified. Another simulation was run with the same purpose of checking the influence of the ignition energy on the model. To do this, the secondary circuit energy E_s was raised to 1 J (Simulation 17). This much energy is not a realistic amount. The attempt to use a very big amount of energy was done with the aim of checking what variable has the main influence in the early phase of combustion. A positive result (lesser delay in pressure and heat released) would have meant that the model issue is in the kernel development phase, for example the kernel might be too small, or the initial burnt mass m_b^{ign} might be under-extimated in the spark convection phase, affecting the spark source term S_{conv} in FSD equation (see Chapter 3.3.3). The results though, show a very weak improvement, pressure curve is still very close to the original (no combustion) one, as it's possible to see in graph 5.2. It means that, in our model, to an increase of ignition energy, does not correspond necessarily a proportional acceleration of the flame kernel developing phase. What showed to improve strongly the combustion speed was to have a distributed flame source i.e. multiple ignition pints. One can conclude that ignition energy is not one of the most influential parameters in this case study. It has been kept to 0.1 J after learning this fact.

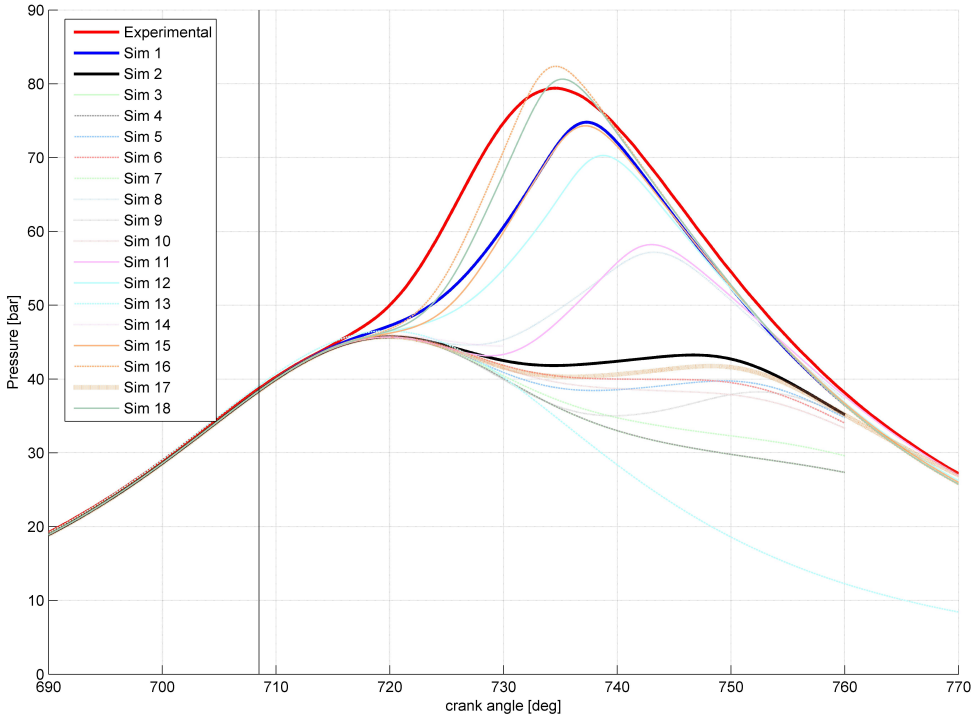

Figure 4.26: Pressure

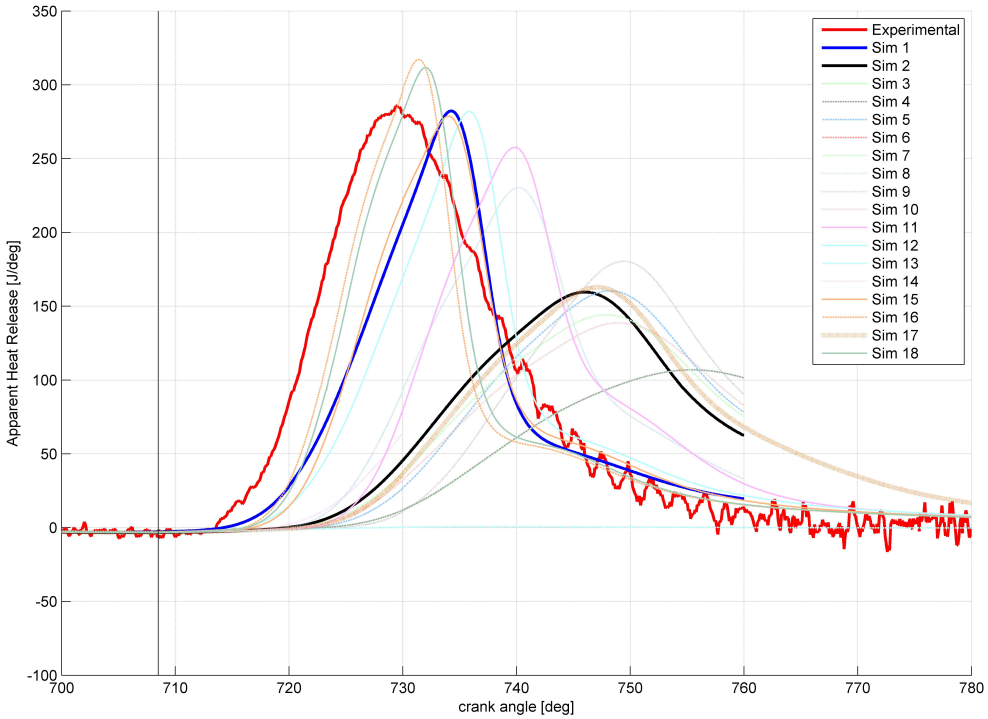

Figure 4.27: Apparent Heat Release

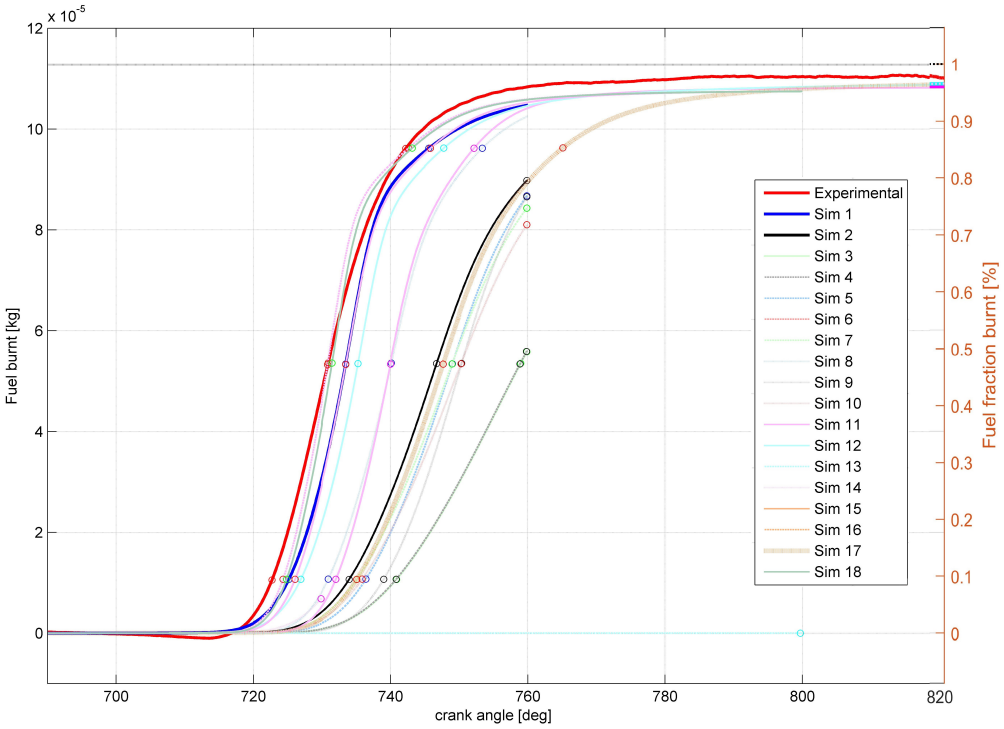

Figure 4.28: Fuel burnt

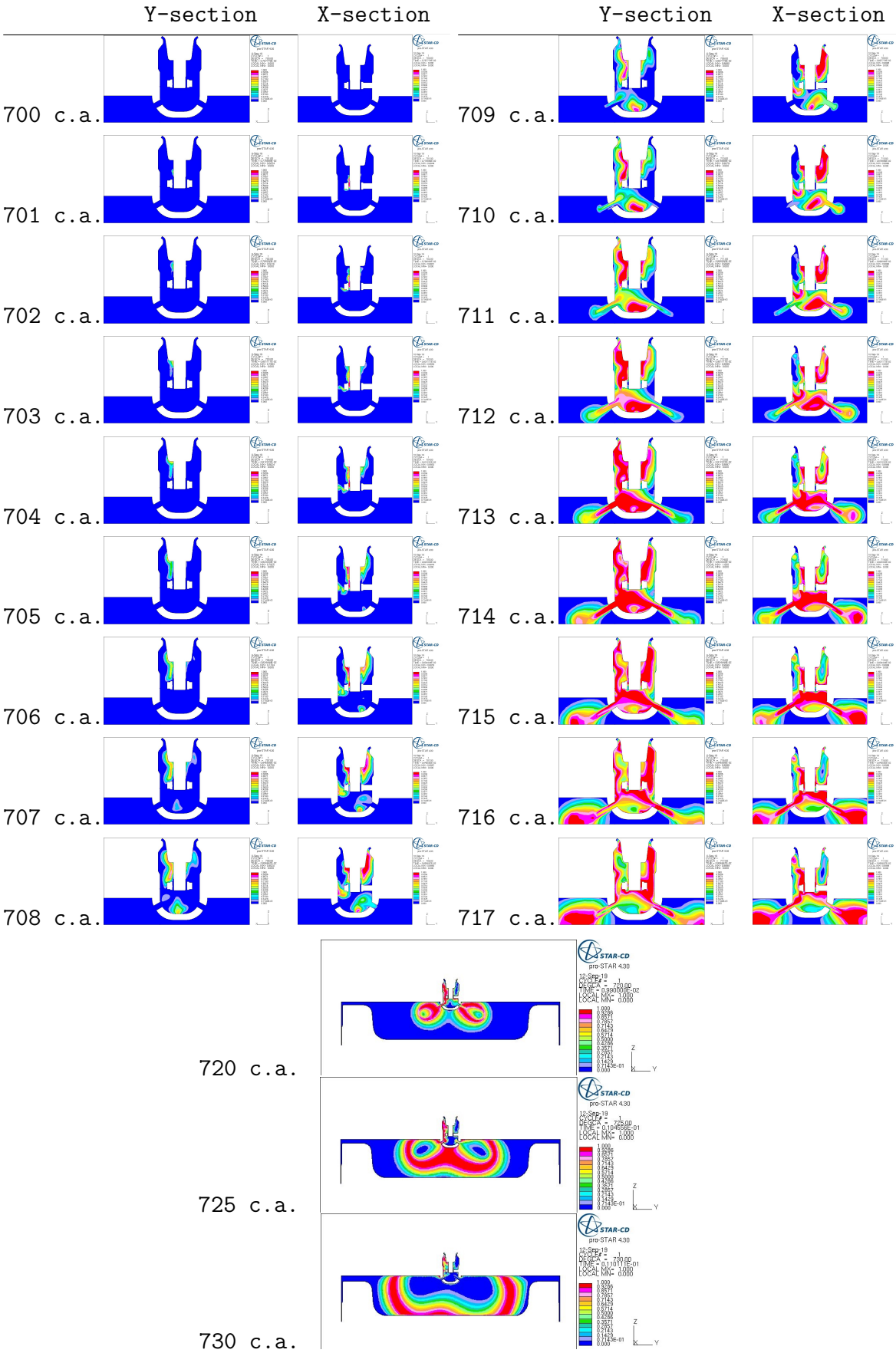

Figure 4.29: Flame front evolution for Simulation 1

4.2.6 Influence of ignition coordinates

As already mentioned, spark breakdown is an energy discharge which, for unpredictable reasons, takes place in a random place within the spark gap. In the 18 simulation performed in the validation process, different spark sites have been used to simulate the unpredictability of the real case. From this very site the flame develops. The results show an important difference in the flame evolution with prechamber, with respect to a standard spark plug. The reasons of the different early flame propagation can be summarized into:

- Flow field inside a prechamber is different with respect to the one available with a standard spark plug
- The spark site is not located on the cylinder axis but slightly away from it (ring-shaped spark gap)
- Flame encounters more physical obstacles i.e. the prechamber walls
- The prechamber is not fully axisymmetric because of the channels situated in discrete locations

However, for the simulation purpose, a part from the multiple ignition points case (Figure 4.25), one ignition point at a time was used, between the ones represented in Figure 4.30.

As mentioned by [11], during the compression stroke (up to TDC) the velocity in the spark gap is pointing upwards. This interval is where the ignition is taking place, so the flow field is driving the flame towards the upper part of the prechamber (Figure 4.29). The position of the spark within the gap height (z coordinate of the ignition point) is not very influential on the flame evolution -as long as it's in a reasonable position, i.e. not too close to the edges-, because the flame is convected upwards quickly. The spark gap height is $1.9cm$, and a z variation of $\pm 0,95cm$ (half of the height) is not sufficient to affect the flame propagation. The influence of this coordinate is negligible. In Figure 4.31 is shown the flame front evolution of Simulations 18 and 3. Both the ignition points are located in the middle width of the spark gap, the Simulation 3 one at $z_3 = 2.4\ cm$ and the Simulation 18 one at $z_{18} = 2.75\ cm$ (middle height of the spark gap). One can see how the flame in its

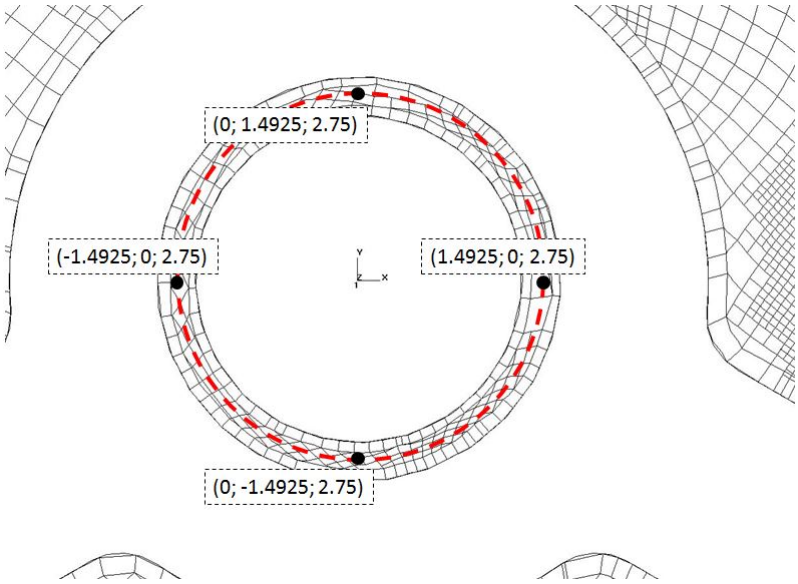

Figure 4.30: Ignition points coordinates.

early phase is convected away from the spark site in a very similar way, regardless of the spark site height.

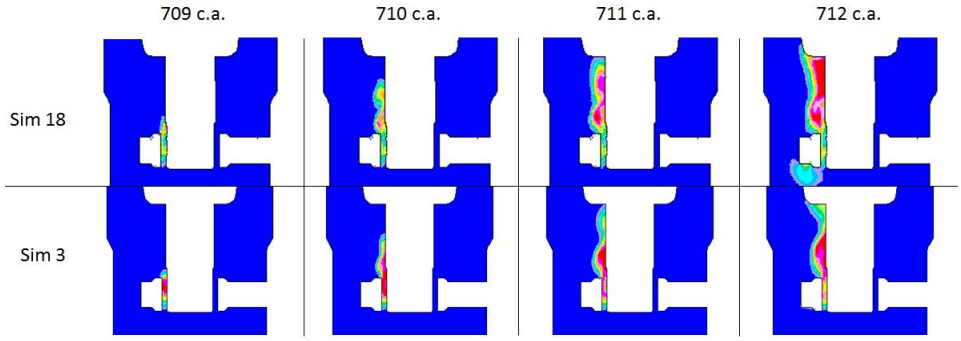

Figure 4.31: Early flame kernel conveted away frome the spark site.

The position of the ignition point within the circumference corresponding to the mean radius of the spark gap is determined by coordinates x and y. The spark site is not by the cylinder axis, meaning that every time one channel is closer to the spark than the other ones. Flame propagates faster in the spark site region: its typical path consists of being driven upwards, then bending around the anode (external ring) to go downwards towards the prechamber channels, and finally diffusing into the main chamber (Figures 4.29 and 4.24). The flame jet coming out from the closest hole is the biggest one, and the one with greater penetration length at each time instant. Even though the effect of this anisotropy has not been fully analyzed in

this work, it's worth to mention that the jets touching the piston have already had the time to re-joint together to a single flame, and that this mechanism is driven by the random spark placement.

4.2.7 Influence of ignition timing

The ignition timing of the real engine is 11.5°, meaning the spark breakdown is realized at 708.5 crank angle. For the sake of understanding the cause for the simulations-experimental data mismatch, four attempts anticipating the ignition timing have been performed. Simulations 1, 12 and 17 have been run anticipating the ignition point to 700 c.a., while in Simulation 14 the ignition happens at 690 c.a.. For all of them, generally speaking, the effect of anticipating the ignition is an easier pressure raise due to the small cylinder volume close to Top Dead Center. Besides, this is the same principle behind the anticipation of ignition timing before TDC in the engine design, as a function of the crank speed and the combustion duration. Let us consider Simulation 14: the main features are the use of *STAR-CD Open* table for laminar flame speed, and the ignition timing anticipated to 690 c.a.. This simulation was run only up to 730 c.a. to verify the effective behaviour in the very early phase of combustion. The results represent a proof for the hypothesis that LFS is one of the main issues of the model. If one compares the results with the ones of Simulation 3, it is possible to see how even anticipating the ignition timing of 18.5 c.a., pressure is not raising much until about 722 c.a., i.e. 32 c.a. after the spark. Coming back to the comparison, the reasons for the very late combustion of Simulation 14 may be several. The laminar flame speed read in the *STAR-CD Open* should be higher at 690 c.a. due to the pressure not raised yet (about 19.5 bar), which is different from the one at 708.5 c.a. (about 38.8 bar). Also the flow field is different. One of the more likely scenarios is that despite of the higher LFS, fluid flow is not powerful enough to transport the flame away from the spark in a short period.

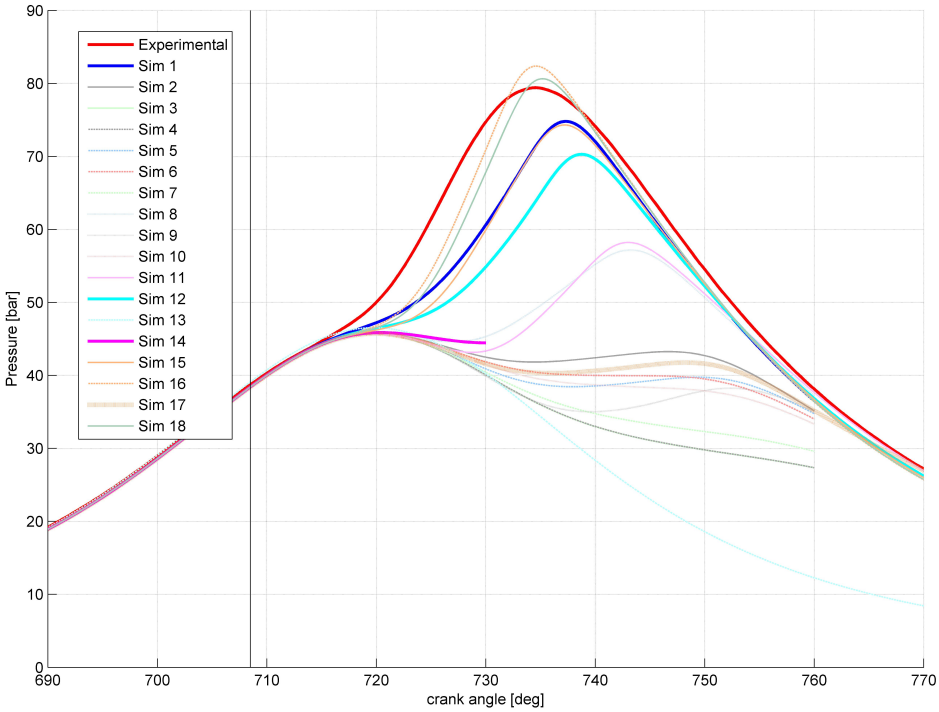

Figure 4.32: Pressure

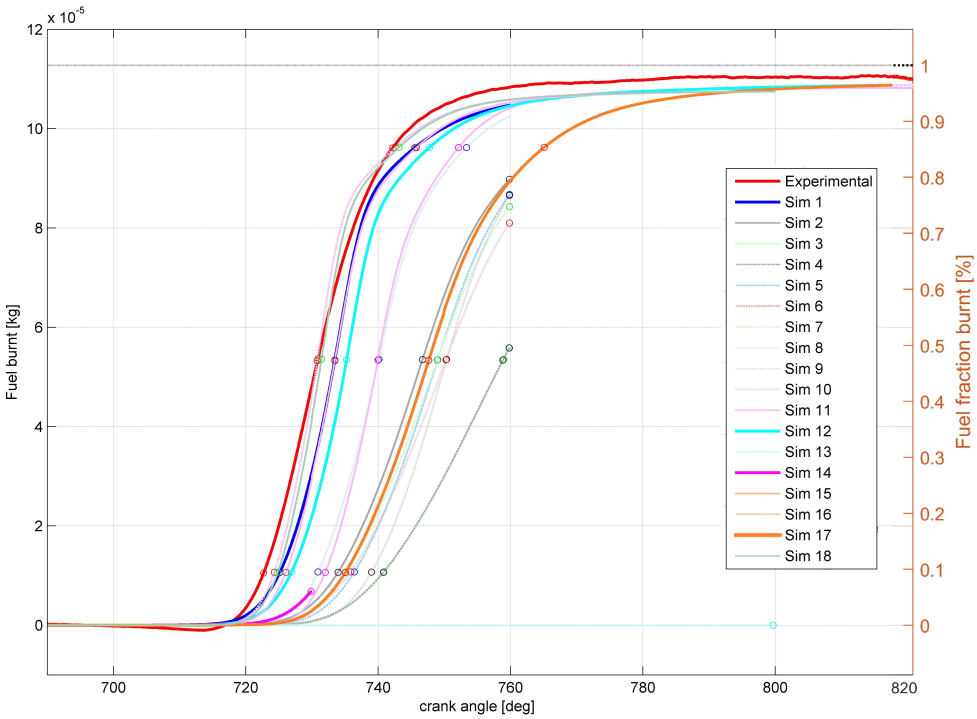

Figure 4.33: Fuel burnt

Chapter 5

Geometry optimization

5.1 New prechamber geometries

To check the influence of the prechamber geometry on combustion, three new prechamber configurations have been tested. As already mentioned in Chapter 4.1.2, the optimization simulations have been run using a fine mesh for the cylinder domain, jointed to each prechamber mesh. All the three new geometries have been investigated by MSc. Yijun Li in his work [11]. In the latter, grid independence study has been performed, as well as an investigation on turbulent kinetic energy, flow field (velocity) and species concentration in the spark gap and in the whole prechamber. In prechamber K2 (*Klein*), the channels are narrower than in the standard configuration, and one more vertical channel has been added at the bottom of the prechamber. K3 configuration (*Rund*) differs from the standard one for the filleted

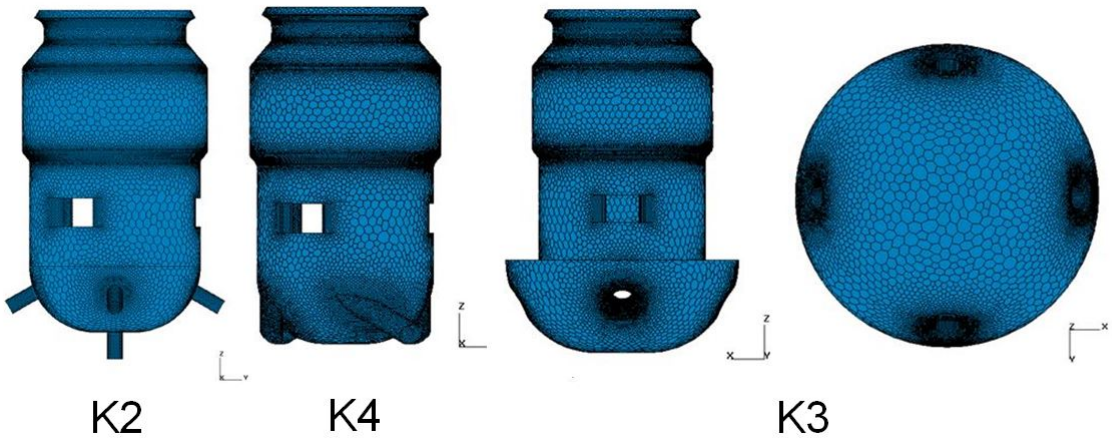

Figure 5.1: New prechamber geometries

channels, which has been done to eliminate all the sharp edges between the channel and the two environments. In K4 prechamber (*Tangent*), the channels are tangential with respect to the cylindrical prechamber wall, and still inclined downwards to better spread the flame over the piston head.

5.2 Choice of the model

The previous chapter lists the all possibilities to adjust a model in Star-CD for the very study case. As some problems in the validation phase occurred, the decision to proceed with the next step of the work required to choose the best model among the ones already described, such as the one which best approximates experimental data, and represents most faithfully possible the real case's course of events. The chose fell on the model of Simulation 18. Provided that laminar flame speed is one of the main issues of the models analyzed, the motivation of the model 18 choice was the need to compute LFS in the best possible way. If the hypothesis that LFS is the main issue is true, then to get consistent values is the final purpose to achieve a good approximation of Experimental case, because it depends mostly on this variable. This is why, even if Metghalchi correlation (Sim 18) is not reccommended for very lean mixtures, it was considered the best choice for this work. The priority here is assigned to match Experimental curves, thus to compute appropriate LFS. Furthermore, the possibility to adjust the LFS in the vicinity of spark plug is a good justification. As already mentioned in Chapter 4.2.4, the correction is activated only up to 55 bar, which has been set consistently with the previous simulations' pressure curve, and it is also the result of a model tuning process. Looking to the pressure curve of Simulation 3 for instance, there is no raise in the early phase. On the other hand, when the slope of the Metghalchi function (Figure 4.18) is altered too drastically like in Simulation 16 ($ULAM3BELOW = 100$), the pressure peak achieved is too high. The correct trade-off seemed to be to lift the correction threshold up to an higher pressure, so to have a consistent behaviour once this early phase is over.

5.3 Results

The standard channels' configuration shows the fastest combustion with respect to the new geometries. Let us consider the pressure curve of K4 (*Tangent*) and K2 (*Klein*). The curves are comparable each other. The pressure peak of K4 is 71.9557 bar @ 737.44 c.a., and the one of K2 is 69.8753 bar @ 738.00 c.a., both delayed of about 3 crank angles from the Experimental one and nearly the same amount from the Standard geometry. In this analysis, it is important to compare the optimization results with the Standard geometry ones as well as to the Experimental ones. Both represent the same case, but in terms of qualitative improvements, i.e. in terms of the effect of the geometry on combustion events, it's appropriate to check the differences with respect to the Standard geometry simulation. In both the new geometries and the Standard one in fact, the same setup has been used, so even if not completely faithful to the reality (Experimental), we can look to the differences as if they are "scaled" in the limit of the simulation's yield. As concerns the results, in both K2 and K4 the pressure curve does not detach from the compression stoke before Top Dead Center i.e. 720 c.a., which is not too far from the correspondent point of the Standard geometry simulation. The pressure slope in the combustion phase is not enough to give the pressure an high peak and, above all, it is not enough to achieve an early peak. As long as the Heat Release strongly depends on pressure and the two curves for K2 and K4 are very similar, the overall AHR curve and the final total energy released expressed as Integrated Heat Release are very similar each other. As a matter of fact, combustion progress (fuel burnt) curves are almost the same, and one can see how they are delayed from Standard simulation of 2.58 c.a. (K2) and of 1.68 c.a. (K4). Despite the similar macroscopic behaviour, local phenomena inside the prechamber are different.

As one can see in the picture Figure 5.7, in K2 prechamber the first channel through which the flame is propagating in the cylinder is the one close to the ignition point (on the negative side of Y axis). The first turbulent jet comes out the prechamber between 715 c.a. and 717 c.a., when the early phase is already over. One possible reason for the slow combustion with respect to the standard geometry here, could be that the bottom channel is not yet used, thus for the flame propagation purpose

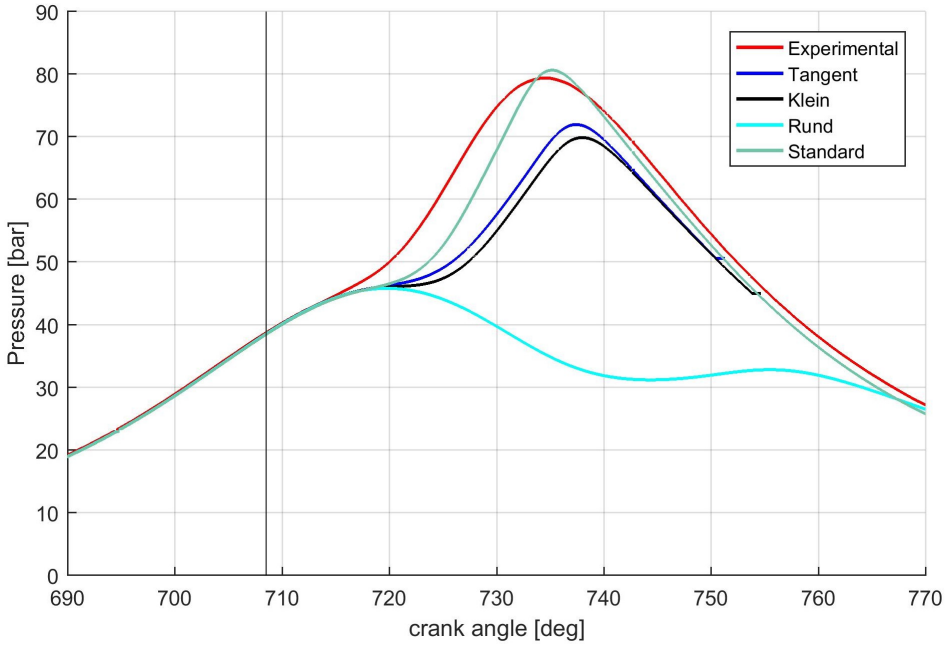

Figure 5.2: Pressure

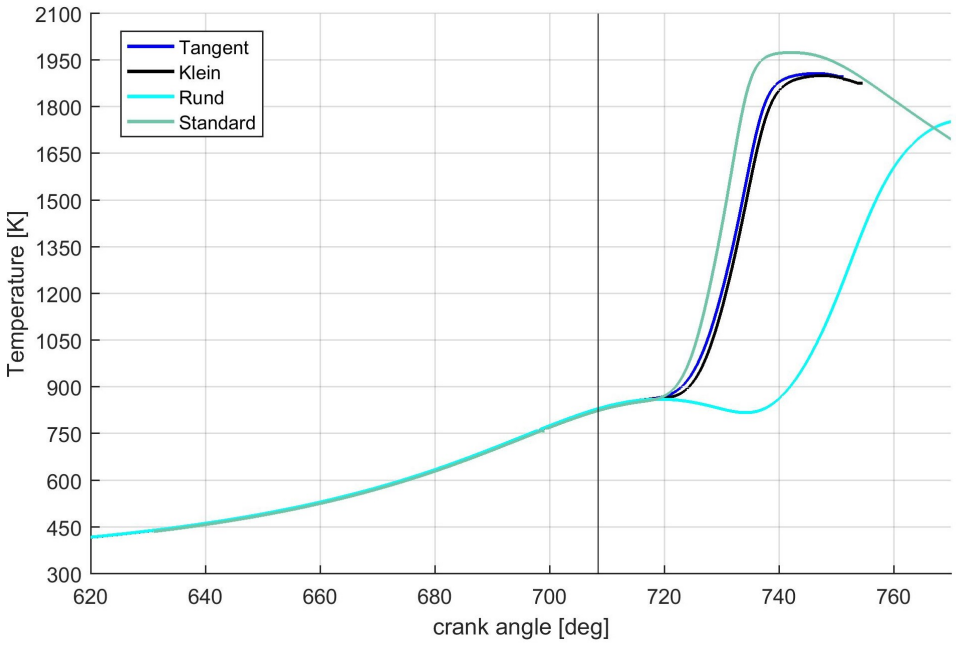

Figure 5.3: Temperature

it's like not having it until it is reached by the flame. Up to that instant, for flame propagation, the geometry is equivalent to one which features 4 small channels. To summarize, the influence of the fifth channel at the bottom of the prechamber shows up after the flame has already reached the main chamber through another channel and, as long as the reason for the combustion delay is in the early phase

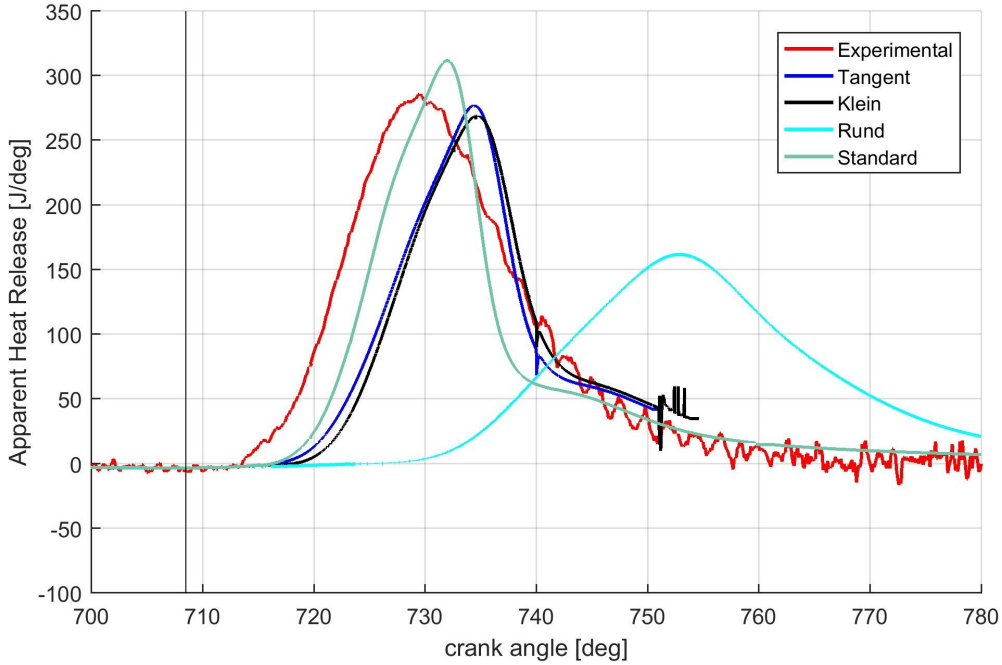

Figure 5.4: Apparent Heat Release

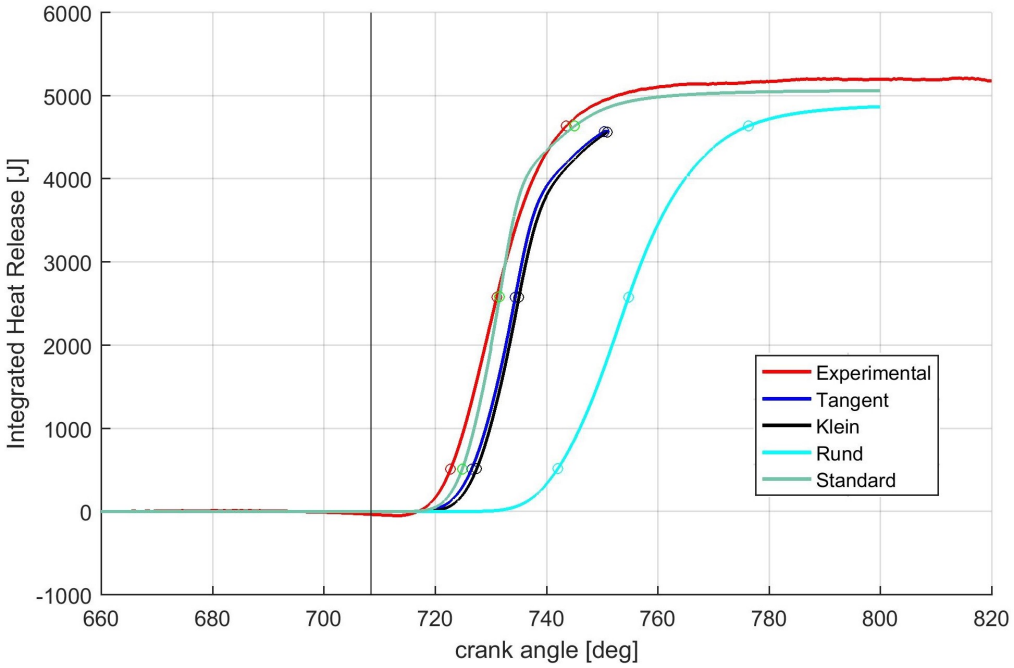

Figure 5.5: Integrated Heat Release

(already completed when the channel is used), the bottom channel is not useful for the purpose of optimizing this prechamber geometry. One can see in Figure 5.10 how the Turbulent Kinetic Energy in the spark gap and at the bottom of the prechamber is very high with respect to the other geometries due to the additional channel. TKE in this case could turn the flame to turbulent very early. If this is true, the effort to

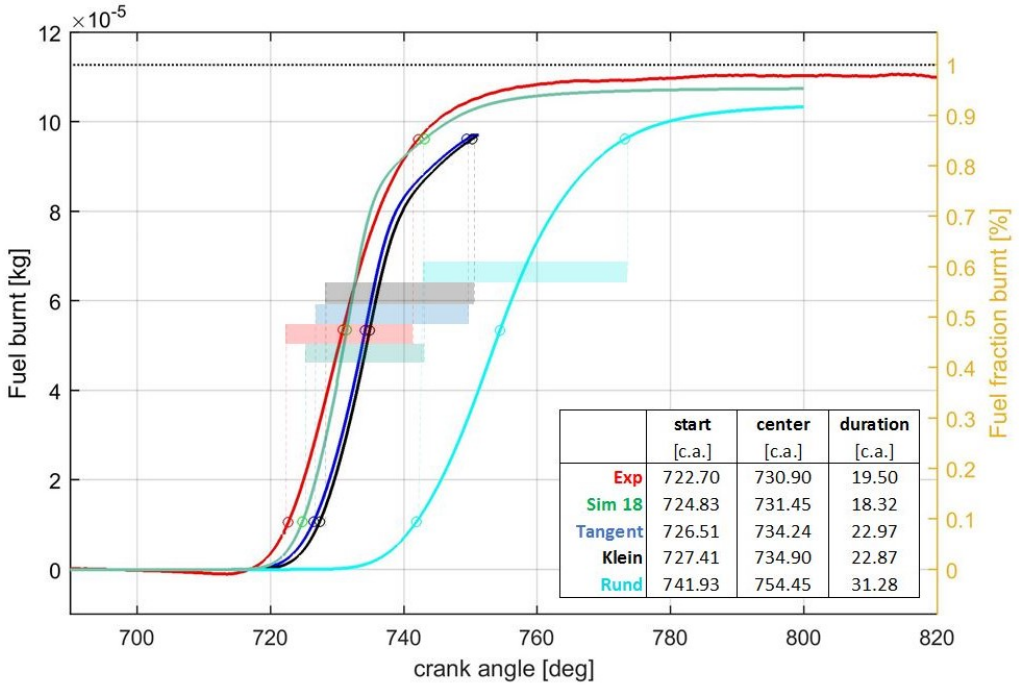

Figure 5.6: Fuel burnt

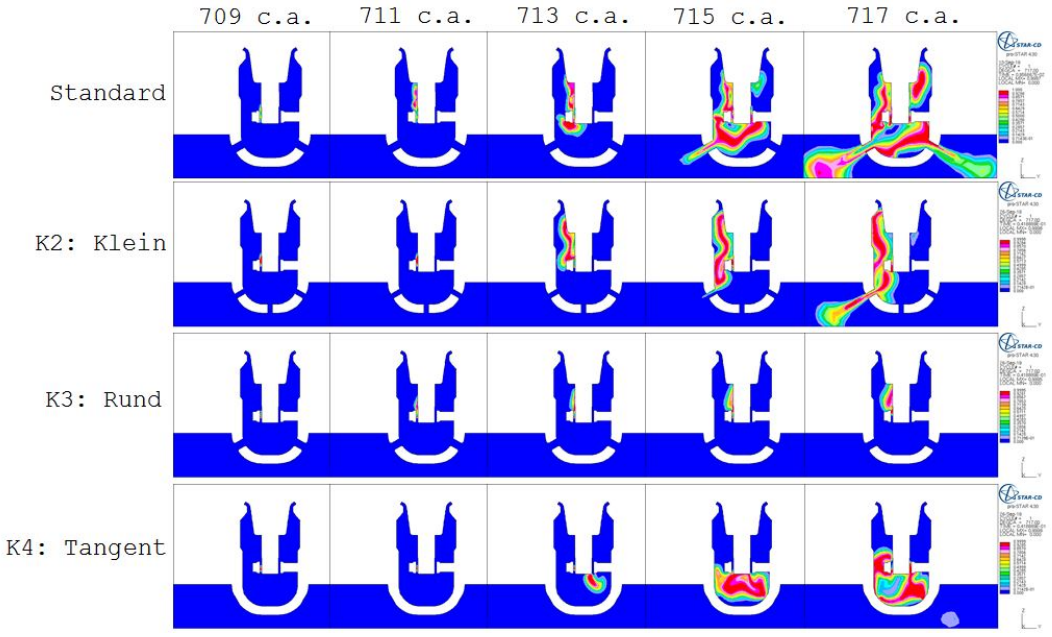

Figure 5.7: Flame front evolution in the new prechamber geometries

use Metghalchi correlation with the low pressure correction could not be consistent, or else the flame speed could be too small. As concerns K4 geometry, the reason for a late pressure raise ($\approx$ 722 c.a.) could be the flame quenching. The turbulent jets which spread in the main chamber through the holes remain very close to the prechamber wall initially due to the tangential orientation of the channels, as one

can see in Figure 5.8.

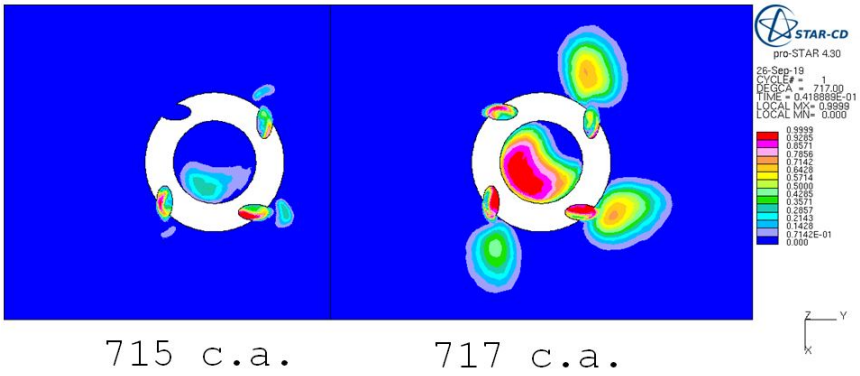

Figure 5.8: Turbulent jets in K4 geometry, z-axis section

Let us analyze the results of the K3 prechamber's simulation. In this case the pressure is not undergoing a strong raise, despite the post processing snapshots show that combustion is actually taking place. Thus, the reason for the slow combustion should be researched in the geometric features of the prechamber. To have filleted holes and not sharp edges should allow the mixture to flow smoothly through the channels, but Figure 5.10 shows how velocity in the channels is lower with respect to the other prechamber geometries. An investigation on this behaviour has been made in [11], and the reason is the low pressure gradient between the two environments (pre- and main chamber). Combustion here is very delayed with respect to the Standard prechamber: the start (10% of fuel burnt) corresponds to 741.93 c.a. versus the 724.83 c.a. of the Standard, and as a matter of fact the overall process is much slower (31.28 c.a. of duration versus 19.50 c.a.). As before, one possible reason for the slow combuston could be that Metghalchi correlation cannot be extended to each single case. One very likely reason furthermore, could be that the flow field is not fast and powerful enough to convect the flame away from the spark site. In this case the flame propagation is not enhanced, thus turbulent jets spread over the piston in a late phase. This hypothesis is supported by the snapshots representing the flame front: it is mostly static until 715 c.a., instant at which in the other geometries, flame is already approaching the channels.

	Pressure peak				
	peak [bar]	peak diff. [bar]	diff. % [%]	position [c.a.]	pos. diff. [c.a.]
Exp	79.4079	-	-	734.50°	-
Standard	80.6327	-1.2247	+1.54%	735.20°	+0.70°
K2 (Klein)	69.8753	+9.5326	-12.00%	738.00°	+3.50°
K3 (Rund)	45.8185	+33.5894	-42.30%	719.80°	-14.70°
K4 (Tangent)	71.9557	+7.4523	-9.38%	737.44°	+2.94°

	AHR peak				
	peak [J/deg]	peak diff. [J/deg]	diff. % [%]	position [c.a.]	pos. diff. [c.a.]
Exp	285.7690	-	-	729.50°	-
Standard	311.6959	+25.9269	+9.07%	732.00°	+2.50°
K2 (Klein)	269.1032	-16.6658	-5.83%	734.58°	+5.08°
K3 (Rund)	161.7179	-124.0511	-43.41%	753.15°	+23.65°
K4 (Tangent)	277.2570	-8.5119	-2.98%	734.43°	+4.93°

Figure 5.9: Peak values for pressure and AHR for optimization geometries

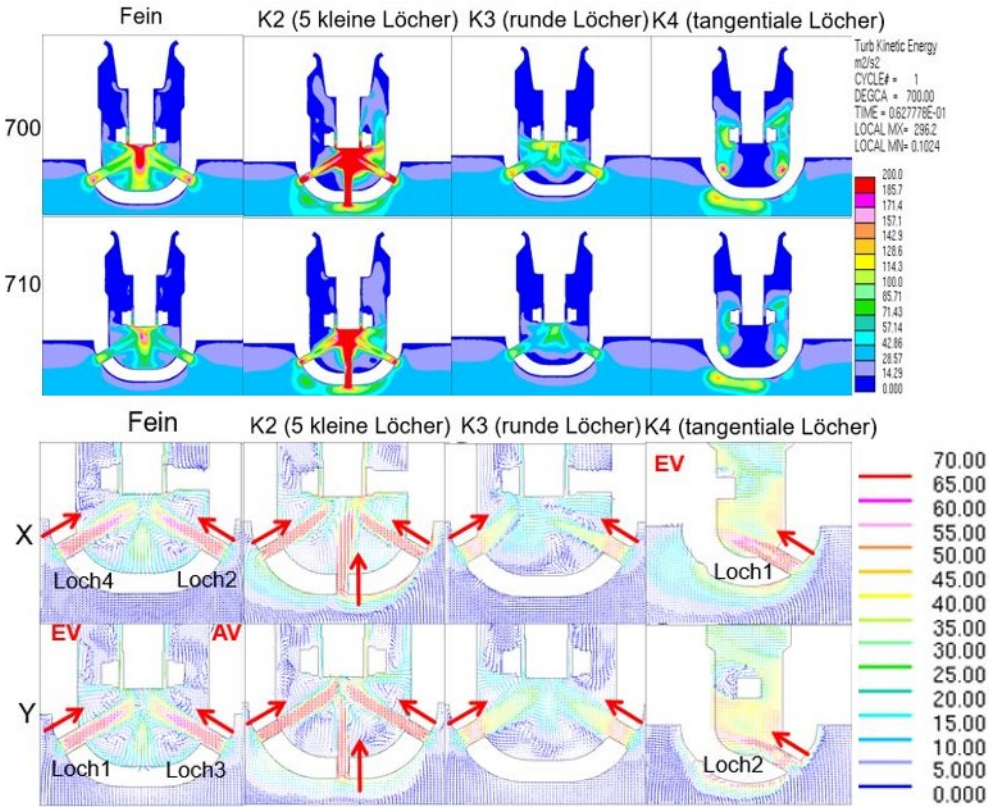

Figure 5.10: Turbulent kinetic energy and velocity field in the new prechambers. The arrows highlight the direction towards the field is pointing to. Picture taken from [11]

Chapter 6

Conclusions

Both the validation phase and the optimization showed that many variables play a role to speed up combustion. As it is possible to see in every post processing flame front snapshot, the flame kernel is always born in correspondence of the ignition timing, meaning that the mixture is immediately ignited. The delay of combustion development thus, is due to geometric features of the engine (prechamber, piston etc..), physical variables influencing the reaction and the flow field. One most influential variable is the Laminar Flame Speed, which governs the early flame kernel development right after ignition, and also the flame propagation. The model used to compute laminar flame speed is a starting point to define a suitable setup for running simulations to test the influence of the geometry. Thus, once a suitable model has been validated, one can consider the changes between the results referred to different geometries. Even though the model is not representing reality in a perfect way, it is possible to analyze the changes due to the different geometries as "scaled" with respect to the Standard one. This approach has validity in the limit of a consistent yield of the model (validity discussed in Chapter 4.2.7).
Optimization showed that the fastest combustion process overall is achieved with the Standard geometry. Pressure is raising faster here and up to an higher peak with respect to te other prechambers. Flame front is also propagating in a more homogeneous way inside the prechamber, influencing the behaviour of the turbulent jets. One important result of this work is the influence of the spark site on the flame front propagation. In every simulation's post processing snapshot is possible to see how the first turbulent jet to diffuse in the main chamber is the one closest to

the ignition point. One possible scenario is that this inequality in the development timing of the jets is annulled as soon as they joint together to a single flame inside the cylinder. Despite this aspect has not fully analyzed in this work, the turbulent jets evolution shows how the ignition point influences the flame propagation, and probably the overall performances, as long as it is not in the center of the dome, thus necessarily close to one of the channels. To control the exact position of the first spark could be a good way to govern the flame propagation through the channels, for instance using multiple spark plugs. A similar scenario is the one reproduced in Simulation 1 (Chapter 4.2.7).
Finally, the work has outlined an optimal configuration for the prechamber: it would include sharp edges combined with tangential or straight channels, and the possibility to control the position of the first spark for instance by means of a smaller and non-annular spark plug.

6.1 Future work

The model of Simulation 18 can be improved to better represent the experimental data. One radical approach could be to use a different combustion model, for example PMV model. One attempt to use a specific laminar flame speed library, made ad hoc for the very case, has been performed, but no positive results have been achieved. To dedicate attention in this way could bring good results, as long as the laminar flame speed is one of the issues of the model. As concerns the optimization, one case which hasn't been tested is to have the spark initiation at an intermediate point between two channels. To check how does the flame split between the channels could give some insights about what is the main factor to drive the flame propagation through the holes process.

Chapter 7

Appendix

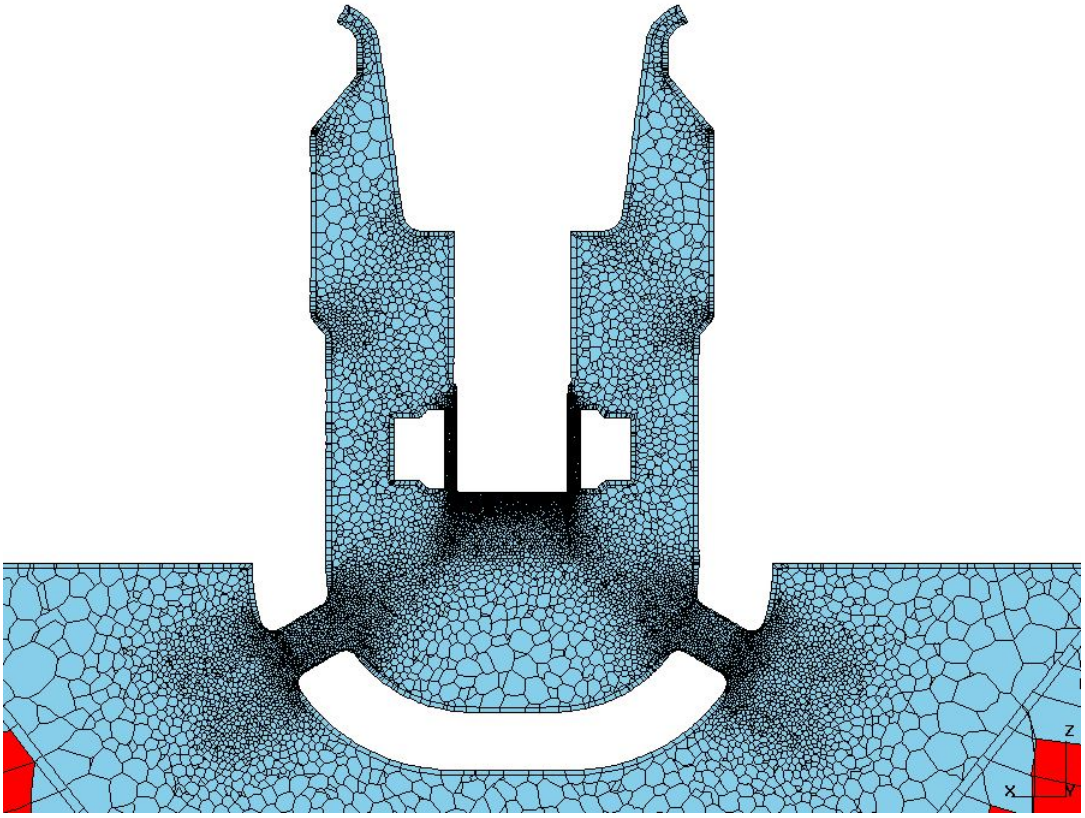

Figure 7.1: Fine mesh: highlight of the prechamber geometry K3. It is possible to see the fillet radius at the channel edge. (y axis section)

	Pressure peak				
	peak [bar]	peak diff. [bar]	diff. % [%]	position [c.a.]	pos. diff. [c.a.]
Exp	79.4079	-	-	735°	-
Sim 1	74.797	-4.6109	-5.81%	737.30°	+2.80°
Sim 2	45.7203	-33.6877	-42.42%	720.00°	-14.50°
Sim 3	45.6539	-33.7540	-42.51%	719.83°	-14.67°
Sim 4	45.6533	-33.7546	-42.51%	719.83°	-14.67°
Sim 5	45.6614	-33.7465	-42.50%	719.85°	-14.65°
Sim 6	45.6937	-33.7142	-42.46%	719.94°	-14.56°
Sim 7	45.6571	-33.7508	-42.50%	719.84°	-14.66°
Sim 8	57.1809	-22.2270	-27.99%	743.25°	+8.75°
Sim 9	45.6554	-33.7525	-42.51%	719.82°	-14.68°
Sim 10	45.7	-33.7080	-42.45%	719.91°	-14.59°
Sim 11	58.2128	-21.1951	-26.69%	743.00°	+8.50°
Sim 12	70.284	-9.1239	-11.49%	738.75°	+4.25°
Sim 13	46.5346	-32.8733	-41.40%	719.78°	-14.72°
Sim 14	45.8643	-33.5436	-42.24%	720.45°	-14.05°
Sim 15	74.3035	-5.1045	-6.43%	737.20°	+2.70°
Sim 16	82.3705	+2.9626	+3.73%	734.60°	+0.10°
Sim 17	45.7199	-33.6880	-42.42%	719.89°	-14.61°
Sim 18	80.6327	+1.2247	+1.54%	735.20°	+0.70°

	AHR peak				
	peak [J/deg]	peak diff. [J/deg]	diff. % [%]	position [c.a.]	pos. diff. [c.a.]
Exp	285.769	-	-	729.50°	-
Sim 1	282.274	-3.4945	-1.22%	734.25°	+4.75°
Sim 2	159.575	-126.1938	-44.16%	746.00°	+16.50°
Sim 3	107.011	-178.7582	-62.55%	755.70°	+26.20°
Sim 4	106.973	-178.7960	-62.57%	755.65°	+26.15°
Sim 5	160.506	-125.2625	-43.83%	748.55°	+19.05°
Sim 6	144.279	-141.4902	-49.51%	747.55°	+18.05°
Sim 7	144.279	-141.4902	-49.51%	747.55°	+18.05°
Sim 8	230.441	-55.3276	-19.36%	740.15°	+10.65°
Sim 9	180.533	-105.2361	-36.83%	749.55°	+20.05°
Sim 10	138.781	-146.9875	-51.44%	748.55°	+19.05°
Sim 11	258.316	-27.4527	-9.61%	740.00°	+10.50°
Sim 12	281.884	-3.8848	-1.36%	735.82°	+6.32°
Sim 13	9.24349	-276.5255	-96.77%	478.00°	-251.50°
Sim 14	63.4228	-222.3462	-77.81%	729.90°	+0.40°
Sim 15	278.724	-7.0448	-2.47%	734.00°	+4.50°
Sim 16	317.21	+31.4406	+11.00%	731.40°	+1.90°
Sim 17	162.868	-122.9014	-43.01%	747.15°	+17.65°
Sim 18	311.696	+25.9269	+9.07%	732.00°	+2.50°

Figure 7.2: Peak values for pressure and AHR. Please note that the negative values in the coloumn "pressure - position difference" are due to the weak combustion, which generates a very slight pressure raise compared to the first peak generated by the compression stroke (except for Simulation 17).

	Domain	Ignition			Ignition (ISSIM)	Spark circuit		ECFM-3Z FSD equation				Boundary conditions Walls	Extended data		
	[deg]	Ignition angle [deg]	Ignition point [cm]		Energy [J]	Resistance [Ω]	Inductance [H]	λ [-]	Laminar flame speed	Auto ignition model	α [-]	β [-]	Electrodes temperature [K]	ULAM3	ULAM3BELOW	PRTRANSL
1	630.9° - 760°	708.5°	(-1.4925; 0; 2.4)		0.1	8000	20	1,5529	STAR-CD open	no	1.6	1	950			
2	630.9° - 760°	**700°**	**4 ignition points**		0.1	8000	20	1,5529	STAR-CD open	no	1.6	1	950			
3	630.9° - 760°	708.5°	**4 ignition points**		0.1	8000	20	1,5529	STAR-CD open	no	1.6	1	950			
4	630.9° - 760°	708.5°	(-1.4925; 0; 2.4)		0.1	8000	**40**	1,5529	STAR-CD open	no	1.6	1	950			
5	630.9° - 760°	708.5°	(-1.4925; 0; 2.4)		0.1	8000	**10**	1,5529	STAR-CD open	no	1.6	1	950			
6	630.9° - 760°	708.5°	(-1.4925; 0; 2.4)		0.1	8000	20	1,5529	STAR-CD open	no	2	1	950			
7	630.9° - 760°	708.5°	(-1.4925; 0; 2.4)		0.1	8000	20	1,5529	STAR-CD open	**TKI EDF**	1.6	1	950			
8	630.9° - 760°	708.5°	(-1.4925; 0; 2.75)		0.1	8000	20	1,5529	STAR-CD open	no	1.6	1	**Adiabatic**			
9	630.9° - 760°	708.5°	(-1.4925; 0; 2.75)		0.1	8000	20	1,5529	**Gülder**	no	1.6	1	950			
10	630.9° - 760°	708.5°	(-1.4925; 0; 2.75)		0.1	8000	20	1,5529	**Metghalchi**	no	1.6	1	950			
11	630.9° - 760°	708.5°	(-1.4925; 0; 2.75)		0.1	8000	20	1,5529	**STAR-CD open**	no	1.6	1	950	standard setup		
12	630.9° - 760°	**700°**	(-1.4925; 0; 2.75)		0.1	8000	20	1,5529	**Gülder**	no	**2**	1	**Adiabatic**			
13	340° - 800°	708.5°	(-1.4925; 0; 2.75)		0.1	8000	20	1,5529	**STAR-CD open**	no	**1.8**	1	**Adiabatic**			
14	630.9° - 730°	**690°**	(-1.4925; 0; 2.75)		0.1	8000	20	1,5529	**library**	**library**	1.6	1	950			
15	630.9° - 730°	708.5°	(-1.4925; 0; 2.75)		0.1	8000	20	1,5529	**STAR-CD open**	no	1.6	1	950			
16	630.9° - 730°	708.5°	(-1.4925; 0; 2.75)		0.1	8000	20	1,5529	**Metghalchi**	no	1.6	1	950	45	50	383959
17	630.9° - 730°	**700°**	(-1.4925; 0; 2.75)		**1**	8000	20	1,5529	**Metghalchi**	no	1.6	1	950	45	100	383959
18	630.9° - 730°	708.5°	(-1.4925; 0; 2.75)		0.1	8000	20	1,5529	**Metghalchi**	no	1.6	1	950	45	standard setup 70	55000

Figure 7.3: Extended version of the simulations' setups

Bibliography

[1] United States Environmental Protection Agency. *Greenhouse Gas Emissions - "Understanding Global Warming Potentials"*. Feb 2017. URL: https://www.epa.gov/ghgemissions/understanding-global-warming-potentials#Learn%5C%20why.

[2] Riccardo Amirante et al. "Laminar flame speed correlations for methane, ethane, propane and their mixtures, and natural gas and gasoline for spark-ignition engine simulations". In: *International Journal of Engine Research* 18.9 (2017), pp. 951–970.

[3] GP Beretta, M Rashidi, and JC Keck. "Turbulent flame propagation and combustion in spark ignition engines". In: *Combustion and flame* 52 (1983), pp. 217–245.

[4] Giancarlo Ferrari. *Motori a combustione interna*. Società Editrice Esculapio, 2019.

[5] Leonardo Fonseca et al. *Tuning the Parameters of ECFM-3Z Combustion Model for CFD 3D Simulation of a Two Valve Engine fueled with Ethanol*. Tech. rep. SAE Technical Paper, 2016.

[6] Ömer L Gülder. "Turbulent premixed flame propagation models for different combustion regimes". In: *Symposium (International) on Combustion*. Vol. 23. 1. Elsevier. 1991, pp. 743–750.

[7] IAV. *"Intelligent Powertrain – Concepts and Technologies for Minimum Emissions and Maximum Efficiency" (On the Way to 45 Percent Efficiency)*. 2018. URL: https://www.iav.com/en/news/way-45-percent-efficiency/.

[8] Hannu Jääskeläinen. "In-Cylinder Processes of Natural Gas Combustion Modes." In: *DieselNet.com. Copyright* © (Aug. 2019).

[9] Peter Janas and Werner Niessner. “3.2 Towards a Thermally Robust Automotive Pre-Chamber Spark Plug for Turbocharged Direct Injection Gasoline Engines”. In: *Ignition Systems for Gasoline Engines: Internationale Tagung Zündsysteme für Ottomotoren* (2018), p. 122.

[10] Sergio Tosi Juan San Primitivo. *Combustion calibration in a Methane port fuel injection engine with the STAR-CD ISSIM embedding the ECFM-3Z model*. Tech. rep. 2016.

[11] Yijun Li. “Numerische Untersuchung (CFD) der Opti-mierung des Ladungswechsels mit Vorkam-merzündkerze”. M.Sc Thesis. Karlsruher Institut für Technologie, 2019.

[12] Saarang Sharma Marcis Jansons. *Boundary Conditions for Predictive Combustion Simulation*. Tech. rep. Bruce Geist, Fiat Chrysler Automobiles, 2016.

[13] Mohamad Metghalchi and James C Keck. “Burning velocities of mixtures of air with methanol, isooctane, and indolene at high pressure and temperature”. In: *Combustion and flame* 48 (1982), pp. 191–210.

[14] Federico Millo. *Combustione nei motori alternativi: motori ad accensione comandata, slides of the course*. 2018-2019.

[15] Daniela Anna Misul. *Notes from the course "Thermal and Hydraulic Machines"*. 2017.

[16] Mark P. Musculus. “In-Cylinder Processes of Natural Gas Combustion Modes.” In: (Aug. 2015).

[17] Antonella Perrone. “ISSIM spark ignition model extended data set up for different operating conditions”. In: *The Steve Portal* (2018), pp. 1–1.

[18] Siemens. *DARS User's Manual Version 3.02*. 2018.

[19] Siemens. *STAR METHODOLOGY For Internal Combustion Engine Applications Version 4.30*. 2018.

[20] Siemens. *Tutorials es-ice Version 4.30*. 2018.

[21] Siemens. *User Guide es-ice Version 4.30*. 2018.

[22] SoCalGas. *"Benefits of Natural Gas Vehicles" - Learn about the environmental and economic benefits of natural gas vehicles.* Sep 2019. URL: https://www.iav.com/en/news/way-45-percent-efficiency/.

[23] M Zellat et al. "A new spark model for SI engine in STAR-CD: The Imposed Stretch Spark Ignition Model-Concept and preliminary validations to SI-GDI combustion". In: *International Multidimensional Engine Modeling User's Group Meeting*. 2013.

List of Figures

1.1 Fluid domain 7

2.1 Pressure evolution (*indicated cycle*) 10
2.2 Piston and valves position during each stroke 11
2.3 Ideal cycle and thermal efficiency 12
2.4 Turbulent Jet Ignition 14
2.5 Natural gas price 15
2.6 Combustion chamber 16

3.1 Turbulent flame front 25
3.2 Laminar flame speed components 26
3.3 ECFM-3Z model schematic 27

4.1 Prechamber coarse mesh 35
4.2 Flow chart 37
4.3 Simulations' list 38
4.4 Pressure 38
4.5 Temperature 39
4.6 Apparent Heat Release 39
4.7 Integrated Heat Release 40
4.8 Fuel burnt 40
4.9 Combustion duration 41
4.10 Flame front evolution (Sim 3) 43
4.11 α pressure curve 46
4.12 α AHR curve 46
4.13 Early flame temperature 48

4.14 Pressure 50
4.15 Apparent Heat Release 51
4.16 Integrated Heat Release 51
4.17 β exponent 57
4.18 S_l correction 57
4.19 Pressure 59
4.20 Temperature 60
4.21 Apparent Heat Release 60
4.22 Integrated Heat Release 61
4.23 Fuel burnt 61
4.24 Flame front evolution (Sim 18) 62
4.25 Multiple ignition points 64
4.26 Pressure 66
4.27 Apparent Heat Release 66
4.28 Fuel burnt 67
4.29 Flame front evolution (Sim 1) 68
4.30 Ignition points 70
4.31 Early flame 70
4.32 Pressure 72
4.33 Fuel burnt 72

5.1 New prechamber geometries 73
5.2 Pressure 76
5.3 Temperature 76
5.4 Apparent Heat Release 77
5.5 Integrated Heat Release 77
5.6 Fuel burnt 78
5.7 Flame front in new prechambers 78
5.8 Turbulent jets in K4 geometry, z-axis section 79
5.9 Pressure and AHR peaks (new prechambers) 80
5.10 TKE and velocity field (new prechambers) 80

7.1 Fine mesh (K3) 83

7.2 Pressure and AHR peaks (validation) 84
7.3 List of the simulations 85

List of Tables

1.1 Engine specifications 8

3.1 Gülder coefficients 30

4.1 Fine mesh cells 36
4.2 Time step 36
4.3 Boundary conditions 47
4.4 B.C. electrodes setup 48
4.5 star-cdopen 53
4.6 Multiple ignition point coordinates 63